

Spring 1-1-2013

Characterization of Nano-scale Aluminum Oxide Transport Through Porous Media

Sasha Norien Norwood
Portland State University

Follow this and additional works at: https://pdxscholar.library.pdx.edu/open_access_etds



Part of the [Environmental Engineering Commons](#), and the [Other Environmental Sciences Commons](#)

Let us know how access to this document benefits you.

Recommended Citation

Norwood, Sasha Norien, "Characterization of Nano-scale Aluminum Oxide Transport Through Porous Media" (2013). *Dissertations and Theses*. Paper 981.

<https://doi.org/10.15760/etd.981>

This Thesis is brought to you for free and open access. It has been accepted for inclusion in Dissertations and Theses by an authorized administrator of PDXScholar. Please contact us if we can make this document more accessible: pdxscholar@pdx.edu.

Characterization of Nano-scale Aluminum Oxide Transport Through Porous Media

by

Sasha Norien Norwood

A thesis submitted in partial fulfillment of the
requirements for the degree of

Master of Science
in
Civil and Environmental Engineering

Thesis Committee:
Gwynn R. Johnson, Chair
Dean B. Atkinson
William Fish

Portland State University
2013

ABSTRACT

Land application of biosolids has become common practice in the United States as an alternative to industrial fertilizers. Although nutrient rich, biosolids have been found to contain high concentrations of unregulated and/or unrecognized emerging contaminants (e.g., pharmaceuticals, personal care products) while containing a significant fraction of inorganic nano-scale colloidal materials such as oxides of iron, titanium, and aluminum. Given their reactivity and small size, there are many questions concerning the potential migration of these nano-sized colloidal materials through the soil column and into our surface and groundwater bodies. Transport of emerging pollutants of concern through the soil column, at minimum, is impacted by colloidal properties (e.g., chemical composition, shape, aggregation kinetics), solution chemistry (e.g., pH, ionic strength, natural organic matter), and water flow velocity. The purpose of this current research was to characterize the long-term transport behavior of aluminum oxide nanoparticles (Al_2O_3) through a natural porous media with changes in pH, aqueous-phase concentration, pore-water velocity and electrolyte valence. Additionally, deposition rates during the initial stages of deposition were compared to several models developed based on colloid filtration theory and DLVO stability theory. Benchtop column laboratory experiments showed that, under environmentally relevant groundwater conditions, Al_2O_3 nanoparticles are mobile through saturated porous media. Mobility increased under conditions in which the nanoparticles and porous media were of like charge (pH 9). Changes in linear pore water velocity, under these same high pH conditions, showed similar transport behavior with little mass retained in the system. Deposition is believed to be kinetically controlled at

pH 9, as evidenced by the slightly earlier breakthrough as flow rate increased and was further supported by observed concentration effects on the arrival wave following several stop flows. While lower aqueous-phase concentrations resulted in significantly longer breakthrough times, the total mass retained in the system was found to be independent of concentration. Additionally, experimental deposition rate coefficients (k_d), used to describe deposition kinetics under “clean bed” conditions, were similar across the aqueous-phase concentrations studied. The use of calcium chloride electrolyte solution in transport studies resulted in enhanced mobility relative to potassium chloride suggesting that changes in groundwater solution chemistry could impact mobility of contaminants associated with biosolids. Predicted deposition rate coefficients, using three different models, were found to under- or over-predict values relative to those experimentally determined values depending on the model. This current research has shown that nanocolloids associated with biosolids, specifically Al_2O_3 , are mobile through saturated porous media. Given the ubiquity of nanocolloidal materials, particularly engineered nanomaterials, coupled with the expected increase in land-application of biosolids, a clear understanding of their transport and fate is prudent to understanding the potential impact these emerging pollutants may have on our surface and groundwater bodies.

TABLE OF CONTENTS

ABSTRACT	i
LIST OF TABLES	v
LIST OF FIGURES	vi
LIST OF SYMBOLS	viii
INTRODUCTION	1
LITERATURE REVIEW	6
Colloid Attachment Theory	8
Colloid Deposition Kinetics	10
Modeling Colloid Deposition	12
Colloid Deposition Research	23
Favorable Attachment	23
Unfavorable Attachment: Ionic Strength	24
Unfavorable Attachment: Colloid Size	27
Unfavorable Attachment: Discrepancies between α and α_{exp}	28
Nano-scale Colloid Transport	31
Nano-scale Metal Oxide Transport	35
Al ₂ O ₃ Nanoparticle Transport	39
MATERIALS AND METHODS	43
Apparatus	43
Porous Media	43
Aluminum Oxide Nanoparticles	45
Column Experiments	45
Collector Efficiency and Deposition Rate Coefficients	48
RESULTS AND DISCUSSION	50

Physical Heterogeneity – Non-reactive Tracer.....	50
Physical and Chemical Heterogeneity.....	51
Favorable and Unfavorable Attachment Conditions (pH 6 and pH 9).....	53
Linear Pore Water Velocity	58
Aqueous-Phase Concentration	62
Electrolyte – Monovalent Versus Divalent Cation.....	65
Collector Efficiency/First-order Reaction Rate Coefficient.....	68
CONCLUDING REMARKS.....	73
REFERENCES	75
APPENDIX – EXPERIMENTAL DATA	84

LIST OF TABLES

Table 1: Tufenkji and Elimelech (2004) dimensionless parameters	17
Table 2: Nelson and Ginn (2011) dimensionless parameters	19
Table 3: Experimental Parameters	44
Table 4: Theoretical single-collector efficiencies (η) compared to experimental single-collector efficiencies (η_{exp}) from Al ₂ O ₃ pH 6 nanoparticle transport experiments	70
Table 5: Theoretical collector efficiencies (η) compared to experimental collector efficiencies (η_{exp}) from Al ₂ O ₃ pH 6 nanoparticle transport experiments	71
Table 6: Experimental and Theoretical Reaction Rate Coefficients – Favorable Attachment Condition Experiments (pH 6)	72

LIST OF FIGURES

Figure 1: Particle transport mechanisms to the collector surface	6
Figure 2: Relative contribution of diffusion, sedimentation, and interception to overall transport as a function of particle size	7
Figure 3: DLVO theory of colloid stability.....	8
Figure 4: Breakthrough Curve of Silica Coated Zirconia – Favorable Attachment	11
Figure 5: Breakthrough curves of 489 nm latex colloids as a function of aqueous-phase concentration and time– Favorable Attachment	12
Figure 6: Single-collector efficiency model compared to experimental values.....	15
Figure 7: Tufenkji and Elimelech and Yao collector efficiency model performance	18
Figure 8: Nelson and Ginn and Tufenkji and Elimelech collector efficiency model performance	22
Figure 9: Latex colloid breakthrough curves with approach velocity of 8.2 cm/min ($v = 1224$ cm/hr) – Favorable Attachment	24
Figure 10: Colloid-collector interaction energy profiles for a representative negatively charged colloid-collector system	25
Figure 11: Particle breakthrough curves of 753 nm negatively charged latex colloids illustrating an increase in deposition with increasing ionic strength	26
Figure 12: Interaction energy profiles for 50, 110, and 1500 nm negatively charged latex colloids in 0.001 – 0.1 M electrolyte solutions	27
Figure 13: Discrepancies between theoretical and experimental attachment efficiencies with changes in ionic strength.....	28
Figure 14: Increasing deposition of silica colloids due to collector patchwise charge heterogeneity and roughness.....	30
Figure 15: Nanoparticle classification: Size and representative natural colloids	31
Figure 16: Engineered Nanoparticle Breakthrough Curves – Unfavorable Attachment ..	33
Figure 17: Impact of solution pH on hematite (α - Fe_2O_3) nanoparticle aggregation rate and hydrodynamic diameter.....	37
Figure 18: Breakthrough Curves of 100 nm Fe_2O_3 Particles – Unfavorable Attachment	38

Figure 19: Alumina (Al_2O_3) breakthrough curves with approach velocity Transport Experiments – Favorable Attachment	41
Figure 20: Representative Non-reactive Tracer Studies Illustrating Physical Heterogeneity	50
Figure 21: Al_2O_3 Arrival Waves Illustrating Physical and Chemical Heterogeneity Relative to NRT Physical Heterogeneity	52
Figure 22: Al_2O_3 Arrival Waves- Favorable (pH 6) and Unfavorable Attachment (pH 9)	54
Figure 23: High velocity Al_2O_3 Nanoparticle Breakthrough Curve ($v = 217 \text{ cm/h}$) – Favorable Attachment	57
Figure 24: Characterization of Velocity Effects on Transport Behavior of Al_2O_3 – Unfavorable Conditions (pH 9)	59
Figure 25: Concentration effects upon stop flow events – Unfavorable Attachment	61
Figure 26: Stop Flow, Favorable Attachment Conditions (pH 6)	62
Figure 27: Al_2O_3 aqueous-phase concentration transport studies	63
Figure 28: Total mass Al_2O_3 nanoparticles retained relative to the total mass injected at three different aqueous phase concentrations	65
Figure 29: Comparison of Al_2O_3 transport using a monovalent (KCl) and divalent (CaCl_2) electrolyte solution.....	66
Figure 30: Comparison of Al_2O_3 Transport Study in KCl to a Higher Ionic Strength Study using CaCl_2	68
Figure 31: Al_2O_3 Early Transport Behavior – Favorable Attachment Conditions	69

LIST OF SYMBOLS

A	Hamaker constant
a_p	radius of a particle
C	particle concentration
C_o	fluid-phase particle concentration
D	hydrodynamic dispersion coefficient
D_∞, D_{BM}	diffusion coefficient in an infinite medium, $D_\infty = D_{BM} = kT/6\pi\mu a_p$
d_c	diameter of spherical collector
d_p	diameter of particle
f	porosity of porous medium
g	gravitational constant
k_d	particle deposition (filtration) rate coefficient
k	Boltzmann constant, 1.3805×10^{-23} J/K
L	filter bed packed length or column length
S	retained particle concentration
T	absolute temperature
t	time
U	approach (superficial) velocity of fluid; darcy velocity
x	distance along column length

Greek Letters

α	single-collector attachment efficiency
η	single-collector removal (collection) efficiency or collection efficiency
η_o	single-collector contact efficiency
η_D	single-collector contact efficiency for deposition by diffusion
η_G	single-collector contact efficiency for deposition by gravity
η_I	single-collector contact efficiency for deposition by interception

μ	absolute viscosity of fluid
v	linear pore-water velocity, $v = U/f$ for saturated porous media
ρ_b	porous medium bulk density
ρ_p	density of particle
ρ_f	density of fluid
γ	$\gamma = (1 - f)^{1/3}$

INTRODUCTION

The production, use, and disposal of anthropogenic compounds has resulted in the detection of compounds in the environment whose distribution and input sources may be largely unknown. These compounds, many with unknown human and environmental health risks, are increasingly being recognized as emerging pollutants of concern. Pharmaceuticals and personal care products (PPCPs) and other anthropogenic waste indicators (e.g., nanomaterials, halogenated compounds, pesticides, flame retardants, plasticizers) have been found in wastewater effluent and surface runoff that feed into our nation's surface waters: waters that provide fish and wildlife habitat, drinking water supplies and recreational resources (1 – 7).

Modern nanotechnology, with a projected market value of \$1.5 trillion by 2015, seeks to fabricate nano-scale materials for a variety of applications including medical devices, consumer products, electronic devices, and wastewater treatment (8, 9). Although nanotechnology serves to improve our quality of life, there is concern that the ubiquity of nano-scale materials, in particular nano-particles, have the potential to negatively impact human health and natural ecosystems via uptake through groundwater, surface water, plants and animals. More specifically, given their reactivity and small size, there are many questions concerning the potential migration of these nano-sized particulates through the soil column and their potential participation in the facilitated transport of contaminants, such as heavy metals and other pollutants of concern.

While research points to wastewater effluent and stormwater runoff as input sources of emerging pollutants of concern, the land-application of biosolids is an exposure pathway of considerable interest among many researchers. Treated sewage sludge, termed biosolids, is increasingly being land applied and marketed as a sustainable solution to incineration or disposal in a land-fill. Of the 7.1 million dry tons generated in the United States in 2004, it is estimated that 55% were land applied where they were spread on the land surface, mechanically incorporated or injected (10, 11). While providing nutrients and improving soil properties of agricultural and reclaimed lands, forests, and parks, biosolids also contain high concentrations of unregulated and/or unrecognized emerging contaminants; including pharmaceuticals, personal care products, and other anthropogenic waste indicators (12 – 15). Additionally biosolids contain a significant amount of inorganic material including heavy metals and metal oxides (12, 14, 16, 17). For example, Jaynes and Zartman (2005) found oxides of iron, aluminum, silicon, and magnesium in their analysis of New York City municipal biosolids (16). Additionally, anthropogenic nano-scale titanium dioxide, commonly used as a whitener and strong UV absorber in consumer products, is believed to have contributed to the titanium found in these same biosolids (16).

Land-application of biosolids presents a possible exposure pathway for these nano-scale emerging pollutants resulting from consumer product usage and disposal of nanoparticle-incorporated products. For example, several studies have shown the migration of pollutants of concern from land-applied biosolids into tile drains used in

agricultural fields (18 – 20). Gottschall et al. (2012) showed that several of the compounds (e.g., bacteriocides and fluoroquinolones) were detected up to a year post-application with four compounds (ibuprofen, triclosan, triclocarbon, and o-desmethylvenlafaxine) also detected in shallow groundwater after the first rain event two days post-application (20). Furthermore in-situ colloid generation and transport through biosolid-amended soils has been shown to occur and has the potential to facilitate transport of heavy metals and those emerging pollutants of concern found in biosolids (17, 21 – 24).

As generation of biosolids from wastewater treatment plants has increased, so have costs of disposal. Disposal via landfill and incineration has become less cost effective such that biosolids slated for beneficial use (e.g., land-application) is expected to continuously grow. Given the ubiquitous nature of many emerging pollutants of concern in the environment coupled with the expected increases in biosolid generation and land-application, a clear understanding of their transport and fate is necessary. Furthermore, a characterization of mechanisms and/or processes potentially facilitating the transport and affecting the fate of these toxins is necessary.

Transport of emerging pollutants of concern through the soil column, at minimum, is impacted by colloidal properties (e.g., chemical composition, shape, aggregation kinetics), solution chemistry (e.g., pH, ionic strength, natural organic matter), and water flow velocity. Colloidal transport and deposition, commonly described using colloid filtration theory in conjunction with Derjaguin - Landau - Verwey - Overbeek

(DLVO) colloid stability theory, typically considers mono-disperse model colloid solutions (e.g., spherical latex particles in mono-valent electrolytes) in model porous media (e.g., glass beads or silica sand). In contrast, variations in surface reactivity and the propensity to form poly-disperse aggregates may result in nanoparticle transport behavior much different than that measured in these model systems. A laboratory assessment of nanoparticle mobility, conducted by Lecoanet et al. (2004) used glass beads to simulate a sandy groundwater aquifer and found markedly different transport behavior among the eight engineered nanoparticles examined, indicating mobility of nanoparticles through soils may be highly variable (25).

Questions concerning the transport and fate of nano-colloidal emerging pollutants through the soil column, particularly those associated with land-applied biosolids, is an important area of concern within our research group. This current research attempts to characterize transport of metal oxide nanoparticles, specifically aluminum oxide nanoparticles, under variable and environmentally relevant groundwater conditions. While ecotoxicity of aluminum oxide nanoparticles, manufactured for use as an abrasive, insulator, and in personal care products, has not been well established, some research indicates a higher conferred toxicity to some plants and animals (26, 27). Benchtop column transport studies were conducted to characterize aluminum oxide nanoparticle transport through a natural porous media using large input pulses and pore-water velocities typical of groundwater flow. While research typically focuses on the initial stages of deposition using short input pulses and significantly higher flow velocities

paramount to colloid filtration theory, this research aims to characterize long-term transport behavior with changes in pH, ionic strength, aqueous-phase concentration, and pore-water velocity. Deposition rates during the initial stages of deposition were examined and compared to models developed utilizing colloid filtration and DLVO colloid stability theory. Given the ubiquitous nature of these emerging pollutants of concern in the environment, a clear understanding of their transport and fate is necessary to assess the potential for contaminant transport and the facilitated transport of toxins through the subsurface and into our surface and groundwater bodies.

LITERATURE REVIEW

Colloidal particles, with at least one linear dimension between 1nm and 1 μ m, are ubiquitous in the natural environment (28, 29). Transport and fate of these particles through saturated porous media is described as a two step process consisting of particle transport to the collector surface followed by attachment (29). While advective flow transports particles through porous media, contact or collision with the media or collector surface occurs via three mechanisms: interception, sedimentation, and/or diffusion, also termed Brownian diffusion (30, 31, Figure 1). Interception is the result of direct contact with the collector as colloids are transported along a streamline of flow. Sedimentation occurs through gravitational settling of colloids flowing along a different trajectory than the aqueous solution. Diffusion is transport through the random motion of particles quantified as a thermal kinetic energy. The extent that diffusion, interception, and

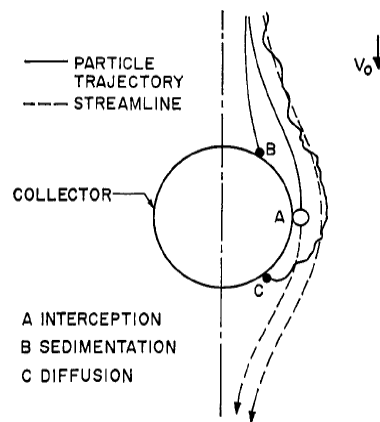


Figure 1: Particle transport mechanisms to the collector surface

(Source: Yao et al. (30))

sedimentation operate in overall colloid transport to the collector surface is dependent, in part, on particle diameter. For particles smaller than $1\mu\text{m}$, diffusion is the dominant filtration mechanism with its contribution increasing as particle size decreases as illustrated in Figure 2 (30 – 33). This behavior is in contrast to particles greater than $1\mu\text{m}$ in diameter whose transport to collector surfaces is increasingly controlled by interception and sedimentation.

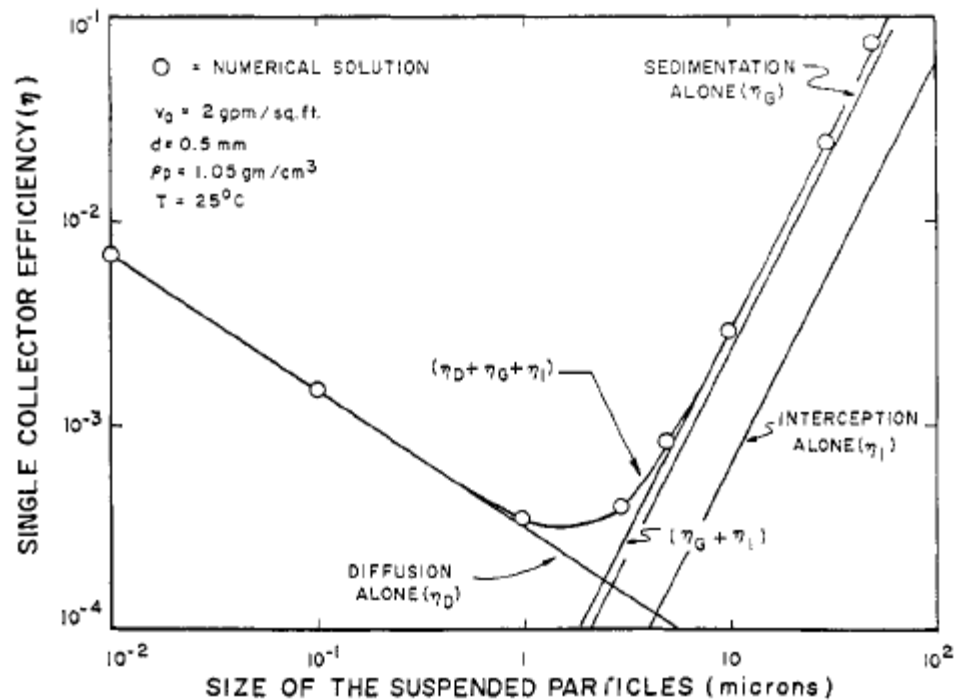


Figure 2: Relative contribution of diffusion, sedimentation, and interception to overall transport as a function of particle size

(Source: Yao et al. (30))

Colloid Attachment Theory

Attachment occurs as the result of interaction forces between charged colloidal particles and collectors. The net force, or net interaction energy, is described by the classic DLVO colloid stability theory, historically used to describe colloid-colloid interactions in aqueous solutions. The net force is the sum of the van der Waals attractive force and electric double layer force (attractive or repulsive) between charged particles (28, 34). The result is a net interaction energy profile that is a function of separation distance between colloid and collector. Figure 3a illustrates the net interaction energy profile of 1- μm diameter spheres in a monovalent electrolyte as a function of separation distance.

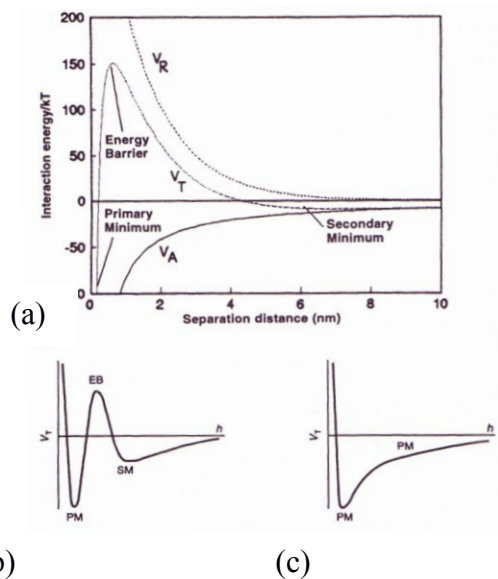


Figure 3: DLVO theory of colloid stability

Interaction energy profile. (a) Total interaction energy (V_T) as the sum of electric double layer repulsion energy (V_R) and van der Waals attraction energy (V_A). (b) Energy profile of like-charged colloids. (c) Energy profile of oppositely charged particles.

(Source: Elimelech et al. (29))

Under natural environmental conditions in the subsurface, colloids and porous media typically carry an overall negative surface charge. As such, these negatively charged colloids will exhibit greater mobility than their positively charged counterparts due to electrostatic repulsion between these colloids and collectors (35, 36). When colloids are of like charge there is a large energy barrier (EB) to deposition in the primary minimum and a shallow secondary minimum (SM) energy well. Under these conditions electrostatic repulsion is the dominant force between colloids and porous media surfaces and attachment to those surfaces is deemed unfavorable. A typical interaction energy profile of colloids under these like-charged conditions is illustrated in Figure 3b. Attachment under these “unfavorable” conditions may occur in the deep primary energy well (PM) and/or in the shallow attractive secondary energy minimum (SM) where attachment is weaker than in the primary energy well and may be reversible. This shallow attractive energy well exists at an optimal separation distance where the net interaction energy is small and attractive; a direct result of the slower rate at which van der Waals attractive energy decreases with increasing separation distance relative to electrostatic repulsion (37, 38).

In contrast, when colloid and collector carry an opposite sign of surface charge the electrostatic interaction force is attractive and shows a net interaction energy profile as illustrated in Figure 3c. Coupled with attractive van der Waals forces there is no energy barrier to attachment. Under these favorable conditions attachment is described as irreversible and transport limited (29).

Colloid Deposition Kinetics

Fundamental theories of deposition kinetics for colloidal particles are based on classic filtration theory. Originally developed to describe particle retention in packed bed filters employed in engineered water treatment systems, the theory describes particle removal at the initial stages of filtration under “clean bed conditions” when the filter bed is devoid of deposited particles (30). A one-dimensional advection dispersion equation with first-order kinetic deposition is typically used to describe colloid transport and fate through saturated porous media under these initial deposition conditions.

$$\frac{\partial C}{\partial t} + \frac{\rho_b}{\theta} \frac{\partial S}{\partial t} = D \frac{\partial^2 C}{\partial x^2} - v \frac{\partial C}{\partial x} \quad (1)$$

$$\frac{\rho_b}{\theta} \frac{\partial S}{\partial t} = k_d C \quad (2)$$

Here C is aqueous concentration, S is the deposited particle concentration, θ is volumetric water content, ρ_b is bulk density, D is the hydrodynamic dispersion coefficient, v is pore-water velocity, x is column or bed length, t is time, and k_d is the particle deposition rate coefficient (39). Under steady state conditions of continuous particle injection and negligible hydrodynamic dispersion (typically assumed for laboratory column experiments) equations (1) and (2) can be simplified to a first-order deposition equation where L is the bed or column length in equation (5).

$$k_d C = -v \frac{\partial C}{\partial x} \quad (3)$$

$$C(x) = C_o e^{-\frac{k_d x}{v}} \quad (4)$$

$$k_d = -\frac{v}{L} \ln \left(\frac{C}{C_o} \right) \quad (5)$$

Colloid filtration theory assumes that during this initial deposition behavior, under “clean bed” conditions, the rate of deposition (k_d) is constant. Results of aquifer tank experiments conducted by Loveland et al. (2003) illustrate the impact of “constant deposition rates” on colloidal transport behavior (see Figure 4). Specifically, an early low-concentration steady-state breakthrough is measured resulting from deposition under clean bed conditions followed by dynamic transport behavior wherein “blocking” occurs impacting subsequent particle deposition (e.g., 40). Additionally, colloid filtration

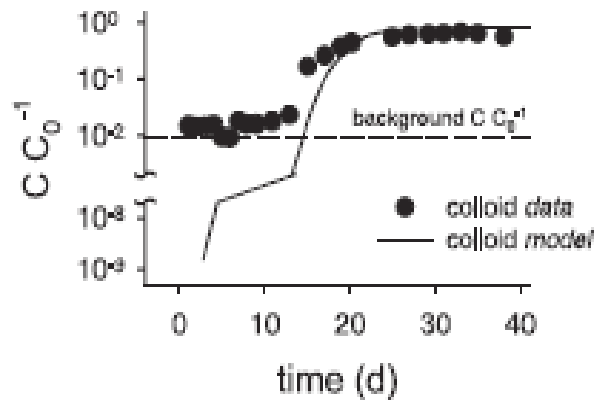


Figure 4: Breakthrough Curve of Silica Coated Zirconia – Favorable Attachment

A low velocity ($v = 2.2$ cm/h) aquifer tank experiment conducted using negatively-charged 150 nm silica-coated zirconia colloids and positively-charged ferric oxyhydroxide coated sand.

(Source: Loveland et al. (41))

theory assumes that the rate of particle attachment to the collector surface is independent of particle concentration. For example, Liu et al. (1995) found that while the effluent concentration at any time-point was dependent on the influent concentration (as

illustrated in Figure 5), the initial breakthrough relative concentration under clean bed conditions ($C/C_0 = 0.2$) was independent of influent latex colloid aqueous-phase concentration (42).

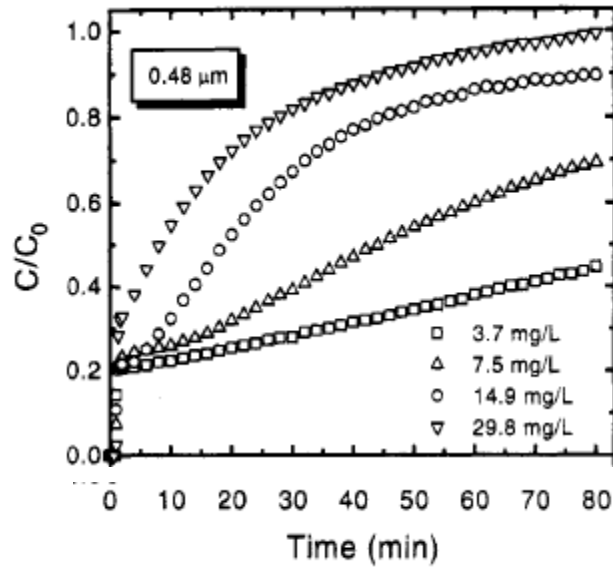


Figure 5: Breakthrough curves of 489 nm latex colloids as a function of aqueous-phase concentration and time – Favorable Attachment

(Source: Liu et al. (42))

Modeling Colloid Deposition

Several filtration models have been developed in an effort to predict colloid deposition rates in saturated porous media under “clean bed” conditions. These models are based on formulations of physical and chemical mechanisms that control colloid transport and attachment where the particle deposition rate coefficient (k_d) is a function of the collector efficiency (η) as illustrated in equation (6) wherein d_c is the collector diameter and f is porosity (32). Equation (6) describes the particle deposition rate onto a

single-collector and as such η is termed the single-collector efficiency by Yao et al. (1971) and Tufenkji and Elimelech (2004) (30, 32). The single-collector efficiency (η) attempts to capture the rate of attachment of those colloids that have made contact

$$k_d = \frac{3(1-f)v}{2d_c} \eta \quad (6)$$

with the collector surface via diffusion, interception, and/or gravitational sedimentation. Specifically, the single-collector efficiency (η) is the ratio of particle attachment rate to rate of advective flow.

$$\eta = \alpha \eta_o \quad (7)$$

Equation (7) illustrates the proportional relationship between the single-collector efficiency (η) and the single-collector contact efficiency (η_o) where that contact efficiency is defined as the ratio of colloid-to-collector rate of contact to the rate of advective flow. The collision (or sticking) efficiency factor (α) describes the fraction of collisions resulting in attachment and is defined as the ratio of the colloid attachment rate to the colloid-to-collector rate of contact (32). When α is unity, all contacts with the collector result in attachment ($\eta = \eta_o$), indicating there is no energy barrier to attachment; this is typically termed as favorable attachment conditions. When α is less than unity (i.e., unfavorable attachment conditions), not all contacts result in attachment such that an energy barrier exists wherein only a certain fraction of collisions will have enough energy to overcome the energy barrier. The extent of attachment is impacted by

particle and collector surface chemistry (e.g., mineralogy and organic matter coatings and content) and solution chemistry (e.g., pH and ionic strength).

Yao et al. (1971) developed a theoretical expression for the single-collector contact efficiency (η_o) wherein the contribution from diffusion, interception, and sedimentation on deposition (η_D, η_I, η_G respectively) are assumed additive as shown in equation (8) (30). While Yao et al. (1971) denotes the single-collector contact efficiency with η (30), it is changed here in equation (8) for consistency with later research nomenclature using η_o . The contribution of particle diffusion, incorporated into Yao's

$$\eta_o = \eta_D + \eta_I + \eta_G \quad (8)$$

$$\eta_D = 4.04Pe^{-2/3} = 0.9 \left(\frac{kT}{\mu d_p d_c U} \right)^{2/3} \quad (9)$$

$$\eta_I = \frac{3}{2} \left(\frac{d_p}{d_c} \right)^2 \quad (10)$$

$$\eta_G = \frac{(\rho_p - \rho_f)gd_p^2}{18\mu U} \quad (11)$$

model with equation (9), to the single-collector contact efficiency is a function of the Peclet number (Pe), a ratio of transport by advective fluid flow to transport by diffusion. Colloid contact via interception, incorporated into the model with equation (10), is a function of the aspect ratio (relative fraction of particle diameter to collector diameter), such that as particle size increases so does the probability that contact with the collector will occur. Gravitational sedimentation (equation 11) is the ratio of Stokes settling velocity to the fluid approach (darcy) velocity (U). This parameter becomes important as

particle diameter and/or particle density (ρ_p) increases. All other parameters are as defined in the List of Symbols section of this thesis.

It is recognized that Yao's filtration model tends to underestimate experimental single-collector efficiencies in packed bed systems (Figure 6). For colloids in the 10 nm to 100 μm size range, the theoretical model tends to under-predict the percent removal of colloids by the filter bed. It is presumed that this underestimation occurs as the model does not capture the impact van der Waals attraction forces and hydrodynamic interactions have on diffusion, interception, and sedimentation (30, 32). Accordingly, the single-collector contact efficiency (η_o) equation has evolved over the years in an attempt

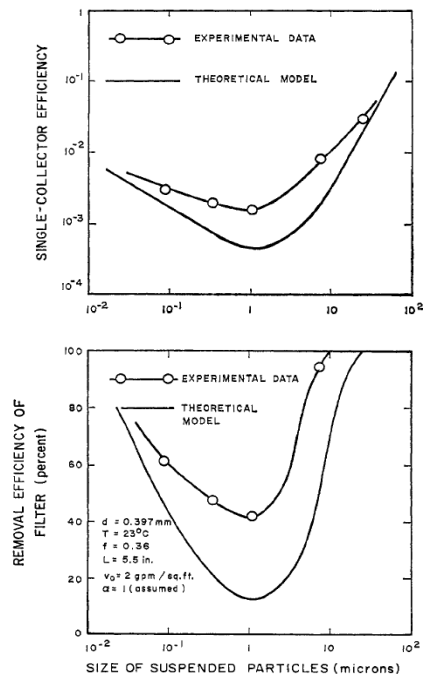


Figure 6: Single-collector efficiency model compared to experimental values

(Source: Yao et al. (30))

to capture these processes. Tufenkji and Elimelech (2004) developed a correlation equation that accounts for the impact of van der Waals forces and hydrodynamic retardation (drag force and torque on particles), processes believed to be important in sub-micron particle transport (32). Specifically, those terms accounting for diffusion, interception, and sedimentation as they impact deposition are described as in equations (12), (13), and (14), respectively. As in the Yao et al. (1971) model, all three transport

$$\eta_D = 2.4A_s^{1/3}N_R^{-0.081}N_{Pe}^{-0.715}N_{vdW}^{0.052} \quad (12)$$

$$\eta_I = 0.55A_sN_R^{1.675}N_A^{0.125} \quad (13)$$

$$\eta_G = 0.22N_R^{-0.24}N_G^{1.11}N_{vdW}^{0.053} \quad (14)$$

mechanisms (diffusion, interception, and gravitational sedimentation) are considered additive with dimensionless parameters defined as in Table 1 (parameters therein are as defined in the List of Symbols section of this thesis). The Tufenkji and Elimelech (2004) model incorporates a porosity dependent parameter (A_s) that is meant to capture the impact of neighboring collectors on the velocity flow field where $\gamma = (1 - f)^{1/3}$. The van der Waals number (N_{vdW}), a ratio of van der Waals interaction energy to the colloid thermal energy (kT), accounts for those van der Waals attraction forces between colloid and collector. Similarly, the attraction number (N_A), is the combined influence of van der Waals attraction forces and fluid velocity on colloid attachment via interception.

Table 1: Tufenkji and Elimelech (2004) dimensionless parameters

$A_s = \frac{2(1 - \gamma^5)}{2 - 3\gamma + 3\gamma^6 + 2\gamma^6}$	Porosity dependent parameter
$N_R = \frac{d_p}{d_c}$	Aspect ratio
$N_{Pe} = \frac{U d_c}{D_\infty}$	Peclet number
$N_{vdw} = \frac{A}{kT}$	van der Waals number
$N_A = \frac{A}{12\pi\mu a_p^2 U}$	Attraction number
$N_G = \frac{2 a_p^2 (\rho_p - \rho_f) g}{9 \mu U}$	Gravity number

The Tufenkji and Elimelech single-collector efficiency model shows better agreement between predicted single-collector efficiencies (η) and experimental single-collector efficiencies (η_{exp}) than the Yao model (equation 15). A side-by-side comparison is illustrated in Figure 7 where the dashed lines represent perfect agreement between the respective models and the experimental collector efficiency calculated from column experiments and the resulting breakthrough curves (equation 15).

$$\eta_{exp} = -\frac{2}{3} \frac{d_c}{(1-f)L} \ln(C/C_o) \quad (15)$$

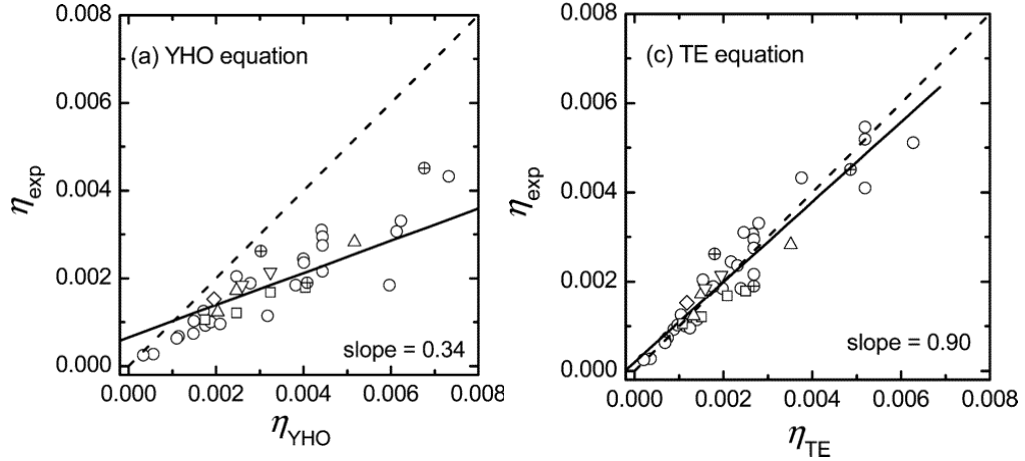


Figure 7: Tufenkji and Elimelech and Yao collector efficiency model performance
 The dashed line represents perfect agreement between the single-collector efficiency model and the experimental single-collector efficiency (η_{exp}). The Yao model is designated as YHO while the Tufenkji and Elimelech model is designated as TE.
 (Source: Tufenkji and Elimelech (32))

The Yao model was again shown to under-predict single-collector efficiencies while the Tufenkji and Elimelech model appears to show near perfect agreement between theoretical and experimental values. The conditions under which this analysis was performed employed oppositely charged colloids and collectors such that no energy barrier exists to colloid attachment (favorable conditions) and all contacts are assumed to result in attachment ($\alpha \approx 1$ and $\eta \approx \eta_o$).

While the Tufenkji and Elimelech model for predicting removal (collector) efficiency is based on the Eulerian approach that looks at the distribution of particle concentration over space and time around a single collector, a more recent model from Nelson and Ginn (2011) attempts to track a single particle's position over time (43). This Lagrangian approach considers the size of the filter bed whereas the Tufenkji and

Elimelech model uses a single collector. As such, the Nelson and Ginn model (equation 16) calculates a collector efficiency using γ^2 to upscale their model from a single collector to a bed of collector surfaces where $\gamma = (1 - f)^{1/3}$.

$$\eta \approx \gamma^2 \left[2.4A_s^{1/3} \left(\frac{N_{PE}}{N_{PE} + 16} \right)^{0.75} N_{PE}^{-0.68} N_{LO}^{0.015} N_{Gi}^{0.8} + A_s N_{LO}^{1/8} N_R^{15/8} + 0.7 \left(\frac{N_{Gi}}{N_{Gi} + 0.9} \right) N_G N_R^{-0.05} \right] \quad (16)$$

Table 2: Nelson and Ginn (2011) dimensionless parameters

$N_R = \frac{d_p}{d_c}$	Aspect ratio
$N_{PE} = \frac{U d_c}{D_{BM}}$	Peclet number
$N_{LO} = \frac{A}{9\pi\mu a_p^2 U}$	van der Waals number
$N_G = \frac{2 a_p^2 (\rho_p - \rho_f) g}{9 \mu U}$	Gravity Number
$N_{Gi} = \frac{1}{N_G + 1}$	

The first term of equation (16) accounts for transport via diffusion, the second term via interception and the last term via sedimentation with dimensionless parameters defined as in Table 2 (parameters therein are as defined in the List of Symbols section of this thesis). Furthermore, in developing their model, Nelson and Ginn (2011) have attempted to more fully capture the impacts of hydrodynamic retardation by considering drag forces and torques on translating and rotating colloids and is in contrast to the

Tufenkji and Elimelech model that only considers hydrodynamic retardation on translating colloids. Finally, while the Yao and the Tufenkji and Elimelech models were developed using flow velocities typical of engineered water treatment systems, the Nelson and Ginn collector efficiency model was developed using groundwater velocities typical in the natural environment.

It should be noted that Nelson and Ginn (2011) have assumed all contacts result in attachment ($\alpha = 1$). They have denoted their equation just as a collector efficiency (η), as their research focus was on conditions in which there is no energy barrier to particle attachment onto a bed of collectors ($\eta = \eta_o$), those conditions where attachment is expected to be favorable. As in Yao et al. (1971) and Tufenkji and Elimelech (2004), the Nelson and Ginn (2011) particle deposition rate coefficient (k_d) is a function of the collector efficiency (η) (equation 17). It should be noted that Nelson and Ginn (2011) have designated their particle deposition rate coefficient as k_f instead of k_d in their research. To maintain a consistent nomenclature throughout this thesis the symbol k_d is used here in equation (17).

$$k_d = \frac{3(1-f)^{1/3}v}{2d_c}\eta \quad (17)$$

Similar to Tufenkji and Elimelech (2004), Nelson and Ginn (2011) compare their model in conjunction with several other models (including the Tufenkji and Elimelech model previously presented) to experimental results using breakthrough data from 112 transport experiments performed under favorable attachment conditions ($\alpha = 1$) (Figure

8). The extent that the Tufenkji and Elimelech model (TE) and Nelson and Ginn model (NG) agree with experimental values is shown in Figure 8 as semi-log plot of the ratio of a theoretical deposition rate coefficient (equation 17) to the experimental deposition rate coefficient (equation 5) on the y-axis with increasing colloid diameter on the x-axis. For this analysis the Tufenkji and Elimelech model (equations 12 – 14) was upscaled by a factor of γ^2 in order to make valid comparisons between models. Additionally, the experimental deposition rate coefficient (k_d) for each experiment (equation 17) was calculated using an experimental collector efficiency values (η_{exp}) from equation (18) below.

$$\eta_{exp} = -\frac{2}{3} \frac{d_c}{(1-f)^{1/3} L} \ln(C/C_o) \quad (18)$$

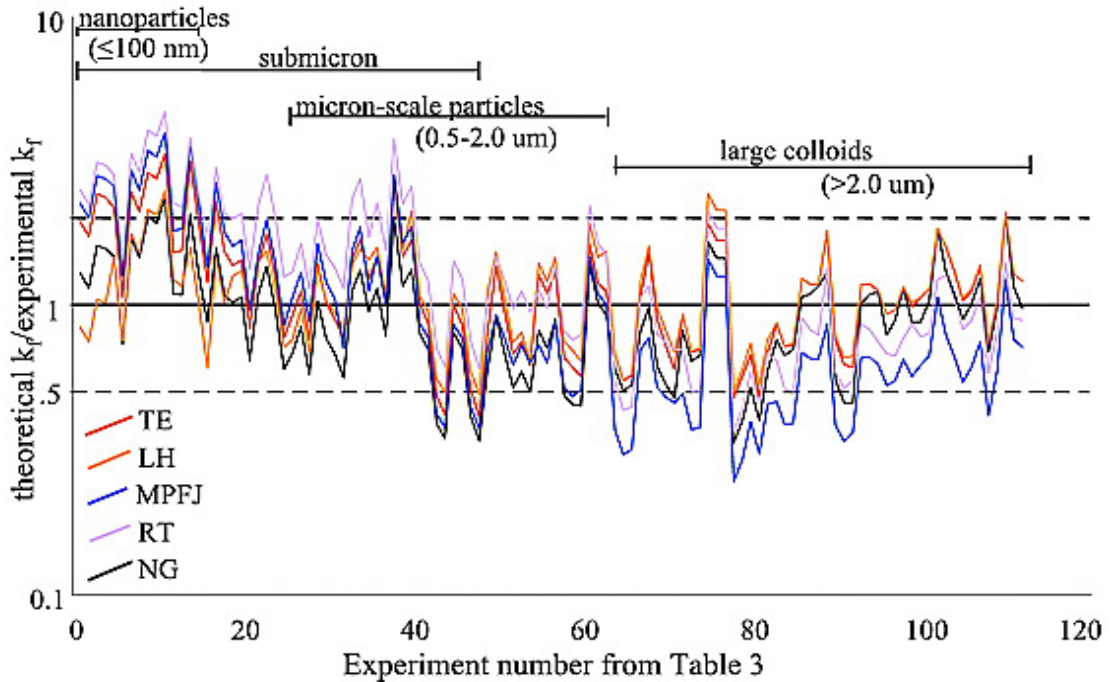


Figure 8: Nelson and Ginn and Tufenkji and Elimelech collector efficiency model performance

The Nelson and Ginn model (NG) results are represented by the solid black curve while the Tufenkji and Elimelech model (TE) is represented by the red curve. The solid horizontal line designates perfect agreement between the model and experimental values while the dashed lines indicate a 2-fold under or over prediction of the deposition rate coefficient.

(Source: Nelson and Ginn (43))

For submicron colloids, both the Nelson and Ginn (NG) and the Tufenkji and Elimelech model (TE) generally over-predict the deposition rate coefficient with the NG model performing slightly better than the TE model in the nano-scale range (defined here as $d_p \leq 100\text{ nm}$) with the two models showing better agreement with each other and with experimental values in the $0.5\ \mu\text{m}$ size range (Figure 8). The TE model performs better than the NG model in the $1 - 2\ \mu\text{m}$ size range showing better agreement with

experimental values. Both models showed better performance for large colloids with diameters greater than 2 μm .

Colloid Deposition Research

Favorable Attachment

As discussed previously, when colloids and collectors carry opposite charges, there is no energy barrier to colloid attachment to the collector, as described in DLVO theory. All contacts with the collector via diffusion, interception, and/or gravitational sedimentation are assumed to result in attachment ($\alpha = 1$). Research has shown that particle size and ionic strength strongly control colloid deposition rates under initial "clean bed conditions" when attachment is believed to be favorable (30 – 33, 42, 44). For example, Elimelech (1994) showed that under low ionic strength conditions (less than 10^{-3} M) the experimental single-collector efficiency (η_{exp}) increased as the diameter of positively-charged latex particles decreased below 1 μm and increased above 1 μm (44). This trend is believed to be the result of diffusion dominated transport to the collector surface for submicron colloids while for colloids greater than 1 μm interception and gravitational sedimentation become increasingly dominant as illustrated previously in Figure 2. Additionally, as ionic strength decreased the experimental single-collector efficiency increased. As ionic strength decreases the electric diffuse double layer thickness around colloids and collectors increases (becomes less compressed) and is believed to result in an increasing magnitude and range of particle-collector attractive

forces that results in increasing attachment (42, 44, 45). Transport experiments conducted by Elimelech (1991) showed increased deposition of positively-charged latex colloids as ionic strength decreased (45). This deposition trend is illustrated in Figure 9 where the breakthrough relative concentration (C/C_0) decreased from ~ 0.6 to 0.4 (i.e., deposition increased) with a decreasing ionic strength from 10^{-1} to 10^{-5} M KCl.

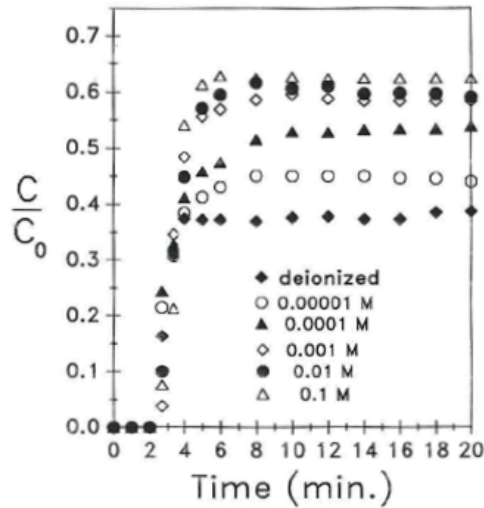


Figure 9: Latex colloid breakthrough curves with approach velocity of 8.2 cm/min ($v = 1224$ cm/hr) – Favorable Attachment

Transport experiments used 477 nm positively latex colloids in deionized water and potassium chloride electrolyte solutions (ionic strength 10^{-5} to 10^{-1} M).

(Source: Elimelech (45))

Unfavorable Attachment: Ionic Strength

As discussed previously, there exists an energy barrier to attachment when colloids and collectors are of like charge and as such the attachment efficiency (α) is expected to be less than unity. DLVO theory predicts as ionic strength increases the energy barrier height to attachment in the primary energy minimum decreases, i.e.,

becomes less positive (46-48, Figure 10). Additionally, the depth of the secondary energy well, representing an attractive energy, increases (becomes more negative).

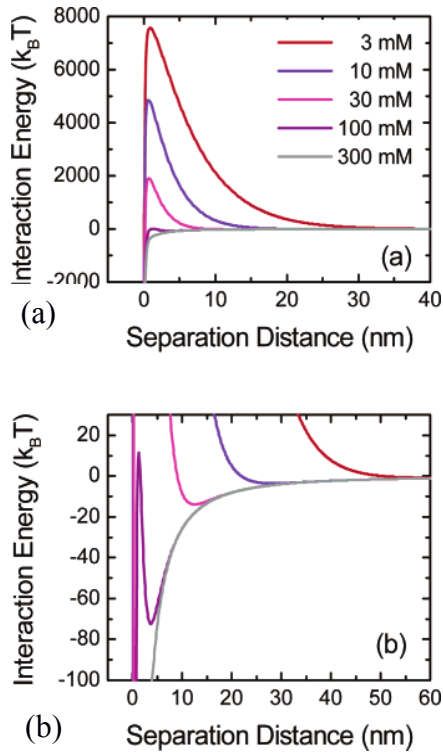


Figure 10: Colloid-collector interaction energy profiles for a representative negatively charged colloid-collector system

(a) Energy barrier to colloid deposition into primary energy minimum. (b) Energy well of the secondary energy minimum.

(Source: Tufenkji and Elimelech (47))

The increase in ion concentration results in compression of the diffuse double layer that translates into reduced electrostatic repulsion between colloids and collectors. As electrostatic repulsion decreases, the van der Waals attractive force, while independent of solution chemistry, becomes increasingly dominant.

Column transport experiments, using negatively charged latex colloids, have shown increased deposition with increasing ionic strength as predicted from DLVO theory (47 – 49). This deposition trend is illustrated in Figure 11 using 753 nm diameter latex colloids and shows that the breakthrough relative concentration

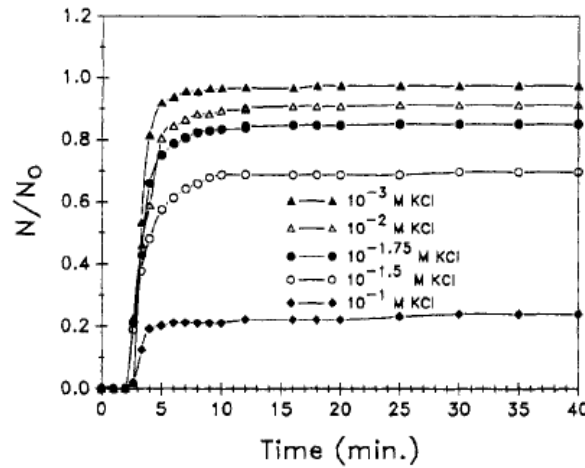


Figure 11: Particle breakthrough curves of 753 nm negatively charged latex colloids illustrating an increase in deposition with increasing ionic strength

(Source: Elimelech (49))

(N/N_0) significantly decreases from ~ 0.9 to 0.2 when ionic strength increases from 10^{-3} to 10^{-1} M KCl, showing an increased retention of colloids onto collectors in the column.

This research is further supported by Pelley and Tufenkji (2008) who showed increasing experimental attachment efficiencies (α_{exp}) with ionic strength, indicating a higher fraction of collisions are resulting in attachment to the collector surface (48).

Unfavorable Attachment: Colloid Size

Interaction energy profiles show an increasing energy barrier height to colloid deposition as diameter increases but concurrently show an increasing depth of the secondary energy well (46, 48, 50). For example, Pelley and Tufenkji (2008) have reported a large increase in the height of the energy barrier as latex colloid diameter increased (see Figure 9) and suggested that the 1500 nm colloids would not attach in the primary energy minimum. Transport experiments showed increased attachment efficiency (α_{exp}) with increasing colloid diameter despite the presence of large primary energy barriers. These results suggest that attachment in the secondary energy well becomes increasingly dominant as colloid diameter increases.

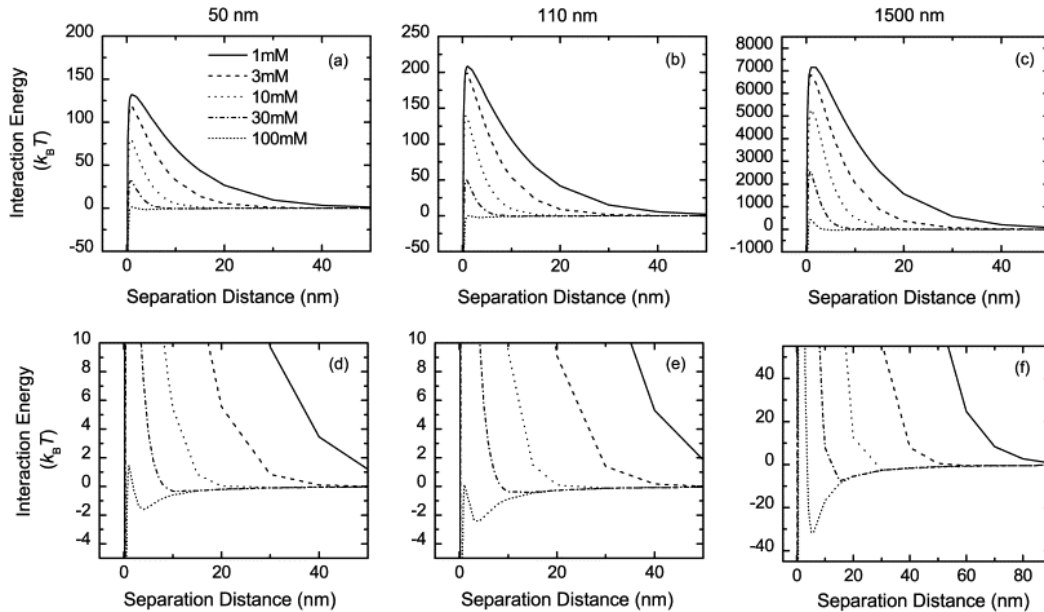


Figure 12: Interaction energy profiles for 50, 110, and 1500 nm negatively charged latex colloids in 0.001 – 0.1 M electrolyte solutions

(Source: Pelley and Tufenkji (48))

Unfavorable Attachment: Discrepancies between α and α_{exp}

Colloid filtration models incorporating colloid attachment theory have increasingly been developed to better predict colloid deposition under unfavorable attachment conditions, when $\alpha < 1$. These models have been shown to significantly under-predict attachment efficiencies relative to experimentally determined values from column transport experiment breakthrough curves (48 – 52). The discrepancies observed have been linked to deposition in the secondary minimum, particle straining, surface charge heterogeneity, and collector surface roughness (49, 50, 52, 53). For example, Elimelech and O'Melia (1990) showed (Figure 13) that experimental attachment efficiencies gradually decrease as ionic strength decreased and is in contrast to theoretical attachment efficiencies that exhibited a very sharp decrease as ionic strength decreased. This discrepancy between model predictions and experimental results

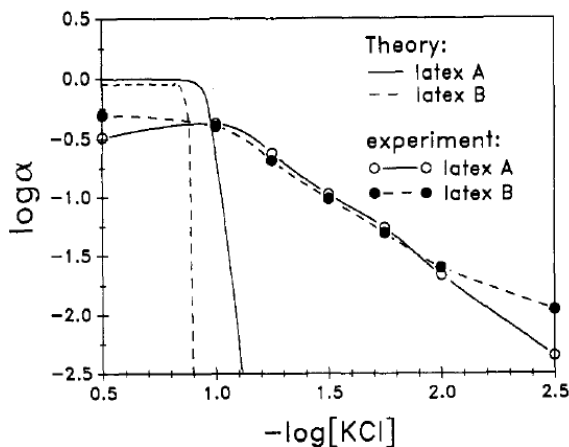


Figure 13: Discrepancies between theoretical and experimental attachment efficiencies with changes in ionic strength

(Source: Elimelech and O'Melia (49))

has been attributed by several researchers to the failure of the model in considering only attachment into the primary energy minimum without considering the contribution of the secondary energy minimum to deposition as was illustrated in Figure 10 and Figure 12 (48 – 50, 53). Litton and Olson (1996) showed that in the presence of large primary energy barriers, latex colloids exhibited an increasing experimental attachment efficiency that was strongly correlated with an increasing secondary energy well as diameter increased and ionic strength increased (50). When deposition in the secondary minimum is incorporated into these deposition models there is improved agreement between theoretical attachment efficiencies and experimental values (50, 53, 54).

Straining, wherein particles become trapped in smaller pore throats, has been suggested as a filtration mechanism that may account for discrepancies observed between predicted and experimental attachment efficiency values. Evidence of straining was shown by Bradford et al. (2002) when $d_p/d_c > 0.0017$ using negatively charged latex colloids (51). Likewise Tufenkji et al. (2004) found straining to be important when $d_p/d_{50} > 0.05$ (55). As DLVO theory does not account for the occurrence of straining experimental attachment efficiencies may be larger than those theoretical values from colloid filtration models employing colloid attachment theory.

Classical DLVO theory assumes a uniform charge distribution on the collector surface while, in reality, imperfections in the crystal lattice structure either through ion arrangement or chemical impurities, such as iron and aluminum oxide substitutions, can

result in a heterogeneously charged surface (37, 42, 56). Additionally, while DLVO theory assumes colloids and collector surfaces are smooth and spherical, scanning electron microscopy has shown individual quartz grain surfaces with a substantial amount of surface roughness, with the surfaces appearing highly irregular, having sharp, angular terminations, jagged protrusions, and deep crevices (55, 57, 58). Johnson et al. (1996) found that as charge heterogeneity decreased with the addition of minor fractions of iron oxyhydroxide coating quartz grain surfaces, deposition of silica colloids increased (Figure 14), and is believed due to the decrease in patchwise charge heterogeneity as the fraction of collector surface increased (59). As illustrated in Figure 14, the particle's breakthrough relative concentration (n/n_0) decreases (deposition increases) as charge heterogeneity increases (specifically, as the fraction of quartz sand coated with iron oxyhydroxide increases from 0% to 16%).

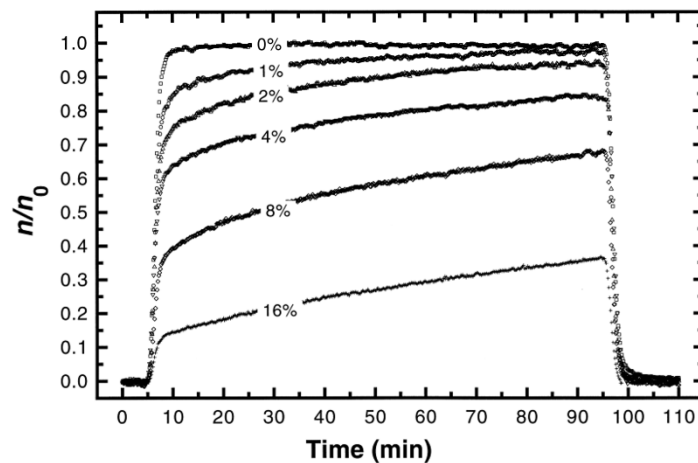


Figure 14: Increasing deposition of silica colloids due to collector patchwise charge heterogeneity and roughness

(Source: Johnson et al. (59))

Nano-scale Colloid Transport

Nano-scale colloids, or nanoparticles, are typically defined as particles with at least one dimension less than 100 nm and include organic and inorganic molecules (e.g., fulvic/humic acids, oxides, clays) and biocolloids (e.g., bacteria, viruses, algae) (60, Figure 15). Organic and inorganic nanoparticles can be naturally produced in the environment with biogenic, geogenic, pyrogenic, and atmospheric origins. These particles are also anthroprogenically produced as combustion by-products and as manufactured/engineered particles. (61).

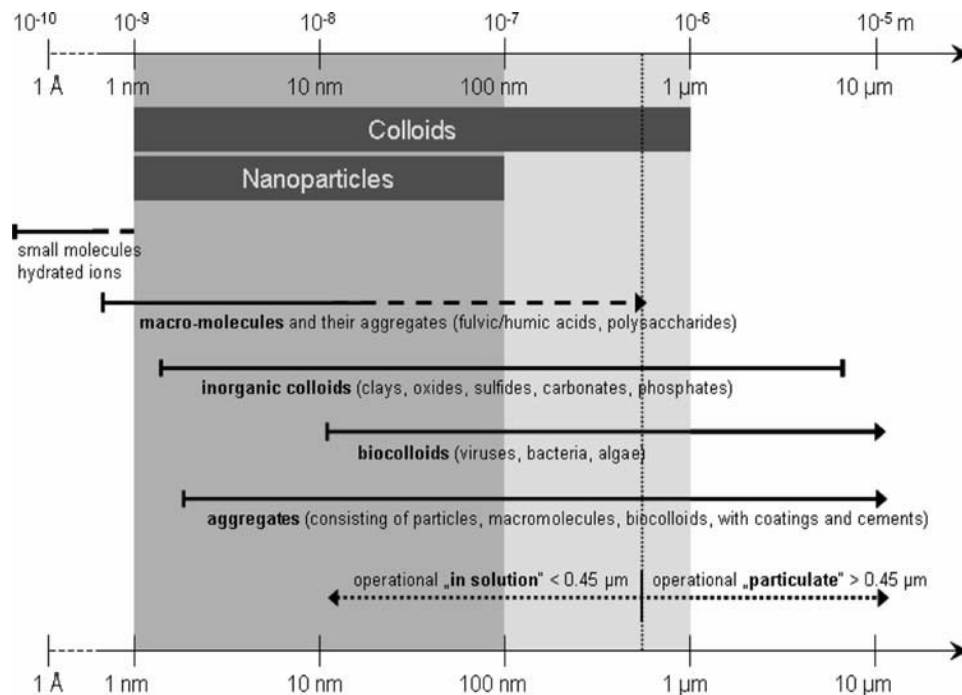


Figure 15: Nanoparticle classification: Size and representative natural colloids

(Source: Christian et al. (62))

Engineered nanoparticles, sometimes designed to amplify surface reactivity, vary in shape and chemical composition including carbon nanotubes of varying complexity, metal oxides and light-emitting crystals called quantum dots. Release into the environment includes direct release from manufacturing processes and remediation efforts and indirect release as a result of consumer product usage and disposal of nanoparticle incorporated products. As particle size decreases the surface area to volume ratio increases, with the percentage of atoms at the particle surface increasing concurrently, resulting in a higher reactivity; a unique feature of nanoparticles (62, 63). For example, 5 nm gold particles have 31% of their atoms at the surface while 50 nm gold particles have only 3.4% at the surface, resulting in nano-scale gold of higher reactivity than its larger counterpart (62).

Transport behavior (mobility) of nano-scale colloids has been shown to be variable with that variability largely due to physicochemical interactions between colloids and collector surfaces. For example, Lecoanet et al. (2004) demonstrated (Figure 16) that mobility of negatively-charged engineered nanoparticles was highly variable in porous media (25). Monodisperse suspensions of spherical nanoparticles (1.2-nm fullerol and 57-nm silica) showed similar transport behavior to the 21-nm single-wall nanotubes with an approach to complete breakthrough occurring in less than 3 pore volumes. In contrast, monodisperse suspensions (135-nm silica and 168-nm n-C₆₀) and polydisperse solutions (198-nm anatase titanium dioxide and 30- nm ferroxane) required more than 6 pore volumes of injection to reach complete breakthrough. These results suggest the import of nanoparticle characteristics (e.g., size, shape, composition, and aggregation kinetics)

significantly impact mobility in porous media.

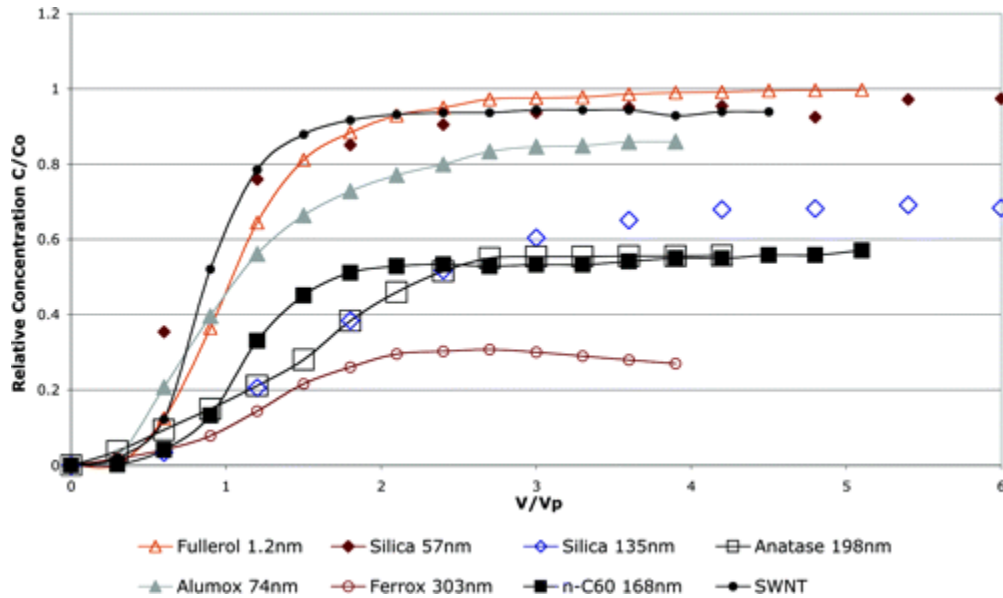


Figure 16: Engineered Nanoparticle Breakthrough Curves – Unfavorable Attachment
 Mondisperse and polydisperse (aggregated) nanoparticle suspensions injected through spherical glass beads at darcy velocity of 0.04 cm/s ($v = 335$ cm/h).

(Source: Lecoanet et al. (25))

Nanoparticles show a greater propensity to form aggregates as the energy barrier to attachment decreases with particle size, as has previously shown in Figure 12. The rate of aggregate formation (aggregation kinetics) and effective particle size are dependent on particle concentration and solution chemistry; namely ionic strength, pH, and counterion valence (64 – 66). Environmental systems may be able to remove larger aggregates to prevent long range transport through water bodies and as such, interception and sedimentation may become important transport mechanisms with aggregate sizes larger than 1 μm (62). Straining has been suggested as an additional colloid filtration mechanism for nano-scale particles and may occur with very small collector diameters,

micron-sized nanoparticle aggregates, and those nanomaterials of irregular shapes such as ellipsoids and helices (33, 51, 55, 63, 67). Subsequent disaggregation and transport of nanoparticles trapped in pore throats may occur with changes in solution chemistry (pH, ionic strength, counterion valence) and flow rate (hydrodynamic shear) (35). Furthermore, changes in solution chemistry, flow rate, or the presence of natural organic matter may result in increased surface charge and stability in aqueous solution subsequently resulting in increased mobility into surface and subsurface drinking water supplies (33, 48, 63, 64, 68 – 70). Additionally, humic acid has been shown to induce disaggregation of iron oxide nanoparticles, resulting in decreasing hydrodynamic diameter and an increase in electrophoretic mobility over a 28 day period (69). A reduction in groundwater ionic strength and shifts in counterion valence, for example from Ca^{2+} to Na^+ , could also increase mobility through disaggregation and/or release of colloidal material (35).

While research has focused on potential organism uptake or adsorption, transport and fate of manufactured nanoparticles is in its infancy (61, 71, 72). Colloid filtration theory and DLVO theory are typically applied to the transport and attachment of nanoparticles to a collector surface. Diffusion is the dominant transport mechanism to the collector while the total particle-particle and particle-collector interaction energies are used as a predictor of nanoparticle stability, aggregation, and deposition onto a collector surface (30, 31, 44, 49, 63). Additionally, non-DLVO or extended DLVO interactions, while not unique to nanoparticles, are amplified and believed to influence nanoparticle

stability and potential transport. These non-DLVO (or extended) interactions include steric repulsive forces due to adsorbed layers of particles such as surfactants or natural organic matter, magnetic forces due to dipole moment(s), and hydration forces resulting from hydrophilic surface functional groups (33, 63).

Under favorable deposition conditions, the deposition rate approaches rate-limited mass transfer and the attachment efficiency approaches unity. When an energy barrier exists, typically under unfavorable attachment conditions, nanoparticles exhibit a lower energy barrier to deposition and aggregation in the primary energy minimum than micro-scale colloids (29, 48 – 50). Furthermore, secondary minimum energies at typical environmental ionic strengths are small so that deposition in the secondary energy well is expected to be minimal. Geochemical heterogeneities and surface roughness are expected to play a larger role in nanoparticle deposition when an energy barrier exists. This is due to the smaller particle size relative to patch-wise charge heterogeneities and areas of surface roughness (33).

Nano-scale Metal Oxide Transport

Metal oxides, while naturally occurring, are increasingly being engineered or manufactured at the nano-scale for a variety of functions. From use as whitening agents and ultraviolet light absorbers to application in environmental remediation and wastewater treatment, there is a concern regarding the potential toxicity of these metal oxide nanoparticles in the environment (73 – 76).

While nano-colloid metal oxide transport is expected to be dominated by Brownian diffusion, gravitational sedimentation may become important in transport to collector surface given their relatively large particle densities (33, 52). Metal oxides are, for the most part, amphoteric; their surface charge is strongly pH dependent (77). As such, solution pH, in addition to ionic strength and counterion valence, heavily impacts particle stability in an aqueous solution and, subsequently, transport and deposition in saturated porous media.

Isoelectric points vary among metal oxide nanoparticles and are typically lower than their bulk counterpart. Consequently, these particles may have a positive or negative surface charge under environmentally relevant conditions (33, 50, 66, 78 – 82). For example, silicon dioxide (SiO_2), an electrical insulator, has an isoelectric point around pH 2.0 while cerium dioxide's (CeO_2) isoelectric point is between pH 7 and 8 while zinc oxide (ZnO), an effective UV absorber, has a high isoelectric point at around pH 9 (81). As “most groundwater matrices carry a net negative charge”, at environmentally relevant pH conditions, negatively charged SiO_2 would be more mobile than the positively charged ZnO (31).

As solution pH moves toward the isoelectric point, particle stability decreases (aggregation rate increases) and the hydrodynamic diameter increases (80, 83). For example, He et al. (2008) showed (Figure 17) as the solution pH of 32 nm hematite ($\alpha\text{-Fe}_2\text{O}_3$) nanoparticles decreases from the point of zero charge (pH 8.2), the

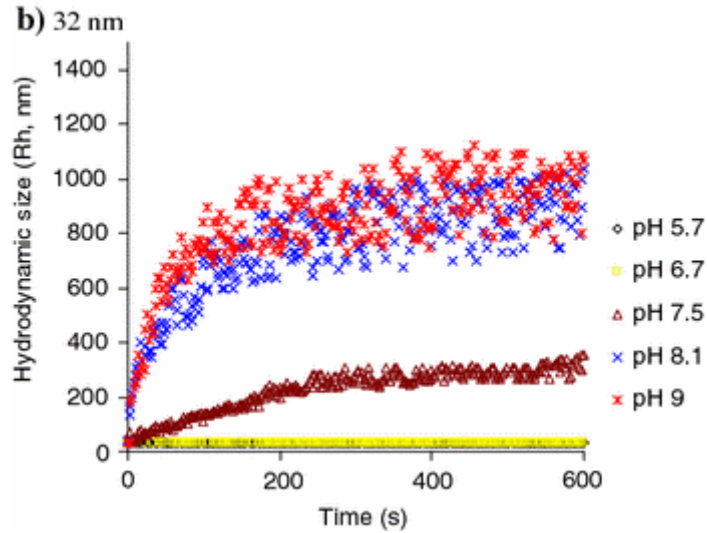


Figure 17: Impact of solution pH on hematite (α -Fe₂O₃) nanoparticle aggregation rate and hydrodynamic diameter

(Source: He et al. (83))

aggregation rate increases and the hydrodynamic diameter increases (83). Additionally, despite the propensity for aggregation, polydisperse solutions of nanoparticles have been shown to be mobile. For example, as shown in Figure 18, despite the measured tendency for fast aggregation behavior (78), nanoparticles of Fe₂O₃ are mobile in aquifer material with complete breakthrough within ~ 2 pore volumes. Furthermore, Guzman et al. (2006) showed that while only 3% of TiO₂ nanoparticles were mobile through a micromodel at the point of zero charge (pH 7), over 80% were mobile at all other solution pHs.

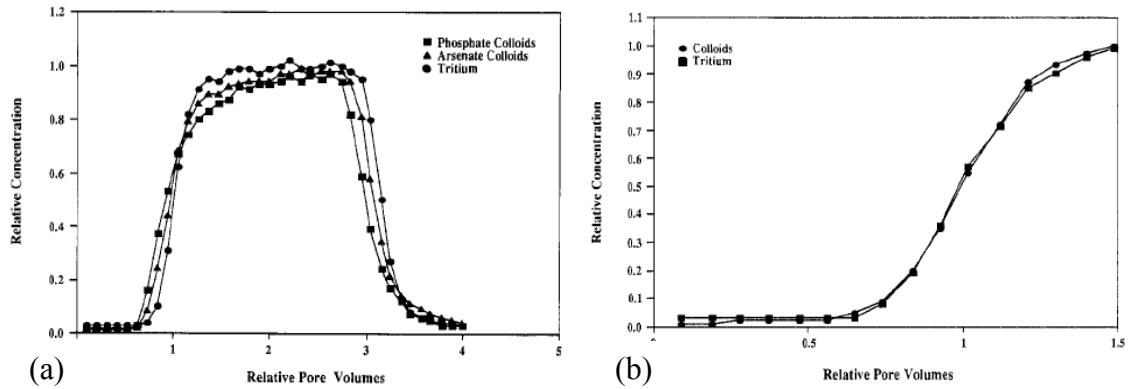


Figure 18: Breakthrough Curves of 100 nm Fe₂O₃ Particles – Unfavorable Attachment

Transport experiments using natural aquifer material and approach (darcy) velocity 0.236 cm/min. (a) Full breakthrough curves of 100-nm Fe₂O₃ nanoparticles in 0.01 M NaH₂PO₄ (phosphate colloids) and 0.01 M Na₂HAsO₄ (arsenate colloids) electrolyte solutions. (b) Arrival wave of the 100-nm Fe₂O₃ nanoparticles in 0.005 M NaCl.

(Source: Puls and Powell (78))

As with other nanoparticles, metal oxide nanoparticles show increased aggregation and deposition with increases in ionic strength (70, 83). Domingos et al. (2009) demonstrated the average hydrodynamic diameter of anatase TiO₂ increased with increases in electrolyte ionic strength (70). Ben-Moshe et al. (2010) showed increased retention in glass bead column transport experiments of rutile TiO₂, ZnO, and CuO with a 10-fold increase in ionic strength from 0.01 to 0.1 M NaCl (81).

The presence of natural organic matter would likely confer an enhanced stability through steric stabilization and negative surface charge (31). For example, addition of fulvic acid to a titanium dioxide nanoparticle (isoelectric point at pH 6) solution resulted in a stable nanoparticle dispersion at environmentally relevant conditions of fulvic acid, pH, and ionic strength (70). Furthermore, disaggregation has been shown to occur in the presence of humic and fulvic acid with iron oxide and titanium dioxide nanoparticles,

respectively (69, 70). Fulvic acid addition to solutions of negatively charged magnetite (Fe_3O_4) and rutile titanium dioxide (TiO_2), and positively charged zinc oxide (ZnO) and copper oxide (CuO) resulted in increased elution (or decreased retention) through a packed bed of negatively charged glass beads (81). These results suggest that long-range transport of metal oxide nanoparticles may be possible and that, while some metal oxides may be unstable in aqueous solution at environmentally relevant ionic strength and pH, stabilizing agents like natural organic matter may enhance mobility through porous media.

Al_2O_3 Nanoparticle Transport

Aluminum oxide, also referred to as alumina, can be found naturally in mineral form and is increasingly manufactured for use as an abrasive and an insulator (27, 84). Activated alumina, a highly porous material with a surface area $> 200 \text{ m}^2/\text{g}$, is used in wastewater treatment as an absorbent for contaminant filtration (9). Nanoparticles of aluminum oxide exhibit amphoteric behavior with an isoelectric point that varies from 8.2 to 10.4 depending upon mineral type (crystalline structure) and method of measurement (85). Ghosh et al. (2008) found the point of zero charge for Al_2O_3 nanoparticles in a KNO_3 solution to be 7.9, lower than the 8.7 found by Tombácz et al. (2008) for bulk Al_2O_3 using the same electrolyte, suggesting that, in general, isoelectric point decreases as size decreases (86, 87).

Ghosh et al. (2008) has shown that while Al_2O_3 nanoparticle suspensions were stable at pH values far from the ZPC, the largest enhancement in particle stability was observed at pH values at or above the ZPC where the zeta potential of the HA- Al_2O_3 particles is increasing (86). Additionally, enhanced aggregation has been shown to occur with the humic acid fraction comprised of small polar fractions and hydrophobic long chains (88). These long chains may act as bridging ligands in the formation of large aggregates. This behavior suggests that natural organic matter may either enhance or reduce Al_2O_3 nanoparticle stability in aqueous solution and therefore their potential for transport through saturated porous media.

Little research has been performed regarding the transport and fate of these nanoparticles in the environment. Zeta potential (a surface potential proxy) of γ - Al_2O_3 was shown to decrease with increasing ionic strength and as solution pH moved toward the point of zero charge (86, 89). These results indicate, similar to other metal oxide nanoparticle research, a decrease in energy of repulsion between particles and hence a reduction of particle stability in solution and increased aggregation (80). Transport experiments using 0.123 nm positively-charged Al_2O_3 in KCl under high velocity conditions show increased mobility as ionic strength decreased (Figure 19).

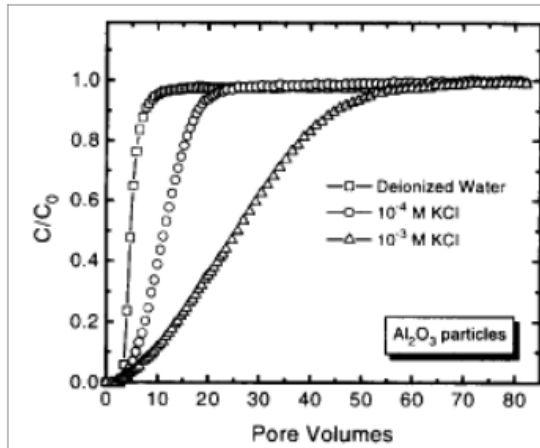


Figure 19: Alumina (Al_2O_3) breakthrough curves with approach velocity Transport Experiments - Favorable Attachment

Breakthrough curves using 123 nm Al_2O_3 in pH 5.6 KCl electrolyte solutions and silica sand as porous media.

(Source: Liu (90); Graphic taken from Ryan and Elimelech (37))

These transport studies, while indicating Al_2O_3 is mobile under flow conditions typical of engineered systems (for example, darcy velocity of 6.0 cm/min), may not represent flow conditions expected under natural subsurface conditions. Similar to TiO_2 , these polydisperse solutions of Al_2O_3 would likely be mobile in saturated porous media when experimental parameters are more representative of the natural subsurface environment. Transport under favorable and unfavorable conditions is likely to be similar to results obtained in other metal oxide nanoparticle studies with transport influenced by solution pH, ionic strength, counterion valence, and presence of natural organic matter (64, 80).

The purpose of this current thesis research is to investigate the transport behavior of aluminum oxide nanoparticles through saturated porous media under environmentally relevant conditions. Research performed at the benchtop scale employed miscible

displacement experiments to delineate the impact of pH, aqueous-phase concentration, linear pore-water velocity, and electrolyte cation valence on the transport of aluminum oxide nanoparticles. Additionally, experimental particle deposition rates under clean bed conditions were determined and compared to models developed by Yao et al (1971), Tufenkji and Elimelech (2004) and Nelson and Ginn (2011).

MATERIALS AND METHODS

Apparatus

Miscible displacement experiments were conducted using acrylic flow cells 5 cm in length with 2.54 cm diameter (Soil Measurement Systems, Tucson, AZ). Column end-plates were fitted with porous polyethylene frits with a 15 to 45- μm pore size from Interstate Specialty Products. Washers were added to the influent and effluent stainless steel compression tube fittings to produce a more uniform wetting front through the column. Flow cell saturation and non-reactive tracer injections were performed using a Hitachi L-6000 HPLC pump, a FMI Q pump or a Sage Instruments 341 Syringe pump. Aluminum oxide injection experiments were performed using a Sage Instruments 341 syringe pump for high and low velocity injections while a FMI Q pump was used for all 0.5 ml/min injections. Parker Paraflex $\frac{1}{8}$ -inch polyethylene tubing was used as influent and effluent tubing on the Hitachi L-6000 HPLC pump and the FMI Q pump while Tygon $\frac{1}{8}$ -inch soft tubing was used for the Sage Instruments syringe pump in conjunction with a 50-ml polyethylene syringe.

Porous Media

Flow cells were packed with 20/30 Accusand ($d_{50} = 0.713$ mm) from Unimin Corporation, a highly uniform, low organic matter content sand containing trace levels of metals and a small cation exchange capacity (58). Prior to packing, the porous media was cleaned using sonication and nanopure water from a Barnstead Nanopure System.

The sand was sonicated for sixty minutes with stirring every five minutes and then rinsed with approximately 10 L of nanopure water and air-dried for 48 hours.

Columns were saturated with electrolyte solution at 0.25 ml/min for 24 hours, followed by 0.35 ml/min for an additional 24 hours. Finally, saturation at 0.5 ml/min was performed for 48 – 72 hours or until no mass change occurred day to day. Saturated pore volume was determined using column volume and porosity. Column porosity was determined using a calculated bulk density and a uniform sand particle density of 2.65 g/cm³. Experimental parameters are included in Table 3.

Table 3: Experimental Parameters

Study Number	Bulk Density (g/cm ³)	Porosity	Pore Volume (mL)
Study #1_pH6	1.87	0.296	7.62
Study #2_pH6	1.83	0.308	7.92
Study #3_pH6	1.78	0.329	8.48
Study #4_pH9	1.80	0.320	8.13
Study #5_pH9	1.73	0.348	8.85
Study #6_pH9	1.79	0.324	8.23
Study #7_pH9	1.79	0.324	8.24
Study #8_pH9	1.80	0.320	8.14
Study #9_pH9	1.75	0.338	8.61

Aluminum Oxide Nanoparticles

Aluminum oxide nanopowder ($\gamma\text{-Al}_2\text{O}_3$), particle diameter < 50 nm (Sigma-Aldrich), was suspended in electrolyte solutions with an ionic strength of 0.015 M or 0.030 M. All aluminum oxide handling was performed in polypropylene containers to prevent particle adhesion to container walls. Particle suspensions, 25 and 200 mg/L in calcium chloride dehydrate ($\text{CaCl}_2 \cdot 2\text{H}_2\text{O}$) solutions and 100 mg/L in a potassium chloride (KCl) solution were pH adjusted to 6.0 ± 0.1 using a sodium hydroxide solution. Additionally, $\gamma\text{-Al}_2\text{O}_3$ nanoparticles (100 mg/L) were suspended in a potassium phosphate buffer solution ($\text{K}_2\text{HPO}_4/\text{K}_3\text{PO}_4$, Fisher Scientific and J.T. Baker) to achieve a stable solution pH between 9 and 10. All electrolyte solutions were made using nanopure water.

Aluminum oxide hydrodynamic diameter in calcium chloride electrolyte solution (pH 6) was obtained from research performed in conjunction with the University of Arizona using a Malvern Zetasizer Nano ZS. Aluminum oxide nanoparticle absorbance values were measured at an optimum wavelength of 204 nm with a UV-Visible Spectrophotometer (Hitachi U-1800) standardized to a ten point calibration curve with a lower detection limit of ~ 1 mg/L.

Column Experiments

Conservative tracer experiments were performed to delineate hydrodynamic characteristics of each packed column using pentafluorobenzoic acid (PFBA) from Acros

Organics and Alfa Aesar in either a pH 6 CaCl₂, a pH 6 KCl, or a pH 9.2 K₂HPO₄/K₃PO₄ electrolyte solution. PFBA effluent samples were collected in glass scintillation vials and absorbance values measured using the UV-Visible spectrophotometer (Hitachi U-1800) at an optimum absorbance wavelength of 226 nm. PFBA concentration was determined using a ten-point standard calibration curve with a lower detection limit of ~1 mg/L. Each calibration curve was performed through serial dilution of a 525 mg/L PFBA stock standard solution prepared on the day of the tracer experiment. Samples whose absorbance was expected to exceed the upper limit of detection were diluted before absorbance measurement.

As part of the analysis to ensure reproducibility between column packings and between the column apparatus a standard moment analysis was performed for all PFBA breakthrough curves. The zeroth moment was calculated, representing the total PFBA mass recovered in the column effluent, and compared to the total mass injected. The percent mass recovery was used as part of the reproducibility analysis. Additionally, the non-reactive tracer breakthrough curves were analyzed using the nonlinear least-squared optimization program CFITIM3 (91) to determine the extent of physical heterogeneity in each packed core.

Large injection pulses of γ -Al₂O₃ nanoparticle suspensions were performed for all experiments to fully capture the impact of long-term retention and the multiple ongoing transport processes that may be occurring. The absorbance value of each effluent sample was immediately measured upon collection using the UV- Vis spectrophotometer at 204

nm and quantified using the calibration curve made using an Al_2O_3 stock solution prepared on the day of the experiment.

Experiments under favorable attachment conditions, $\text{pH} < \text{ZPC}$, were performed using 25 and 200 mg/L of $\gamma\text{-Al}_2\text{O}_3$ in a CaCl_2 electrolyte solution ($\text{IS} = 0.015 \text{ M}$) adjusted to pH 6 with a sodium hydroxide solution. Additionally, a pH 6 experiment was conducted using a KCl electrolyte solution ($\text{IS} = 0.015 \text{ M}$) to ascertain the potential impact a monovalent cation has on Al_2O_3 nanoparticle transport relative to the divalent calcium cation of the CaCl_2 electrolyte. At a $\text{pH} < \text{ZPC}$ the Al_2O_3 nanoparticles are expected to carry a net positive surface charge while the porous media (i.e. collectors) carries an overall net negative surface charge.

Experiments under unfavorable attachment conditions, $\text{pH} > \text{ZPC}$, were performed using 100 mg/L Al_2O_3 in a potassium phosphate buffer ($\text{K}_2\text{HPO}_4/\text{K}_3\text{PO}_4$) at an average pH of 9.2 and ionic strength of 0.015 M. At a $\text{pH} > \text{ZPC}$ the Al_2O_3 nanoparticles are expected to carry an overall negative charge with the porous media maintaining a net negative surface charge. Under these experimental conditions attachment is deemed unfavorable.

Elution of Al_2O_3 from flow cells was performed using a nanoparticle-free electrolyte solution once a gently sloping high concentration, nearly linear, pseudo-steady state condition was measured in the flowcell effluent. The three experiments conducted at pH 6 under favorable attachment conditions were performed using a darcy

velocity (q) of 0.10 cm/min or average pore-water velocity (v) of 18.7 cm /h.

Experiments conducted at pH 9 – 10 under unfavorable attachment conditions were performed at three darcy velocities; 0.03, 0.10, 1.8 cm/min ($v = 4.5, 17.5, 338$ cm/h, respectively).

Collector Efficiency and Deposition Rate Coefficients

Predicted collector efficiencies (η) and predicted deposition rate coefficients (k_d) were calculated for all favorable attachment transport studies conducted in our research group at pH 6; conditions under which no energy barrier is assumed to exist for particle attachment to the porous media.

A theoretical *single-collector* efficiency (η_o) was calculated using both the Yao et al. (1971) and Tufenkji and Elimelech (2004) model for all pH 6 transport experiments (equations 7-14). A theoretical collector efficiency (η) was also calculated using the Nelson and Ginn (2011) model, an upscaled model with the potential for large-scale field applications (equation 16). Each theoretical value was compared to an experimentally derived collector efficiency (η_{exp}) calculated using equations (15) and (18). A Hamaker constant (A) for alumina and silica in water (1.83×10^{-20} J) was used in calculating the van der Waals number and the attraction number (N_{vdW} and N_A , respectively) in the Tufenkji and Elimelech model and the van der Waals number (N_{LO}) in the Nelson and Ginn model (92). Additionally, the theoretical and experimental collector efficiencies

were used to calculate deposition rate coefficients (k_d) (equations 6 and 17) using the theoretical and experimental collector efficiencies from each respective model.

RESULTS AND DISCUSSION

Physical Heterogeneity – Non-reactive Tracer

Non-reactive tracer (NRT) experimental results (Figure 20) show reproducible and nearly ideal transport behavior for all experimental conditions (e.g., pH, electrolyte, and pore water velocity). Additionally, a comparison of measured NRT breakthrough curves to a simulated, ideal NRT breakthrough curve shows a small degree of non-ideal transport behavior. That nonideality is evidenced by the slightly earlier measured

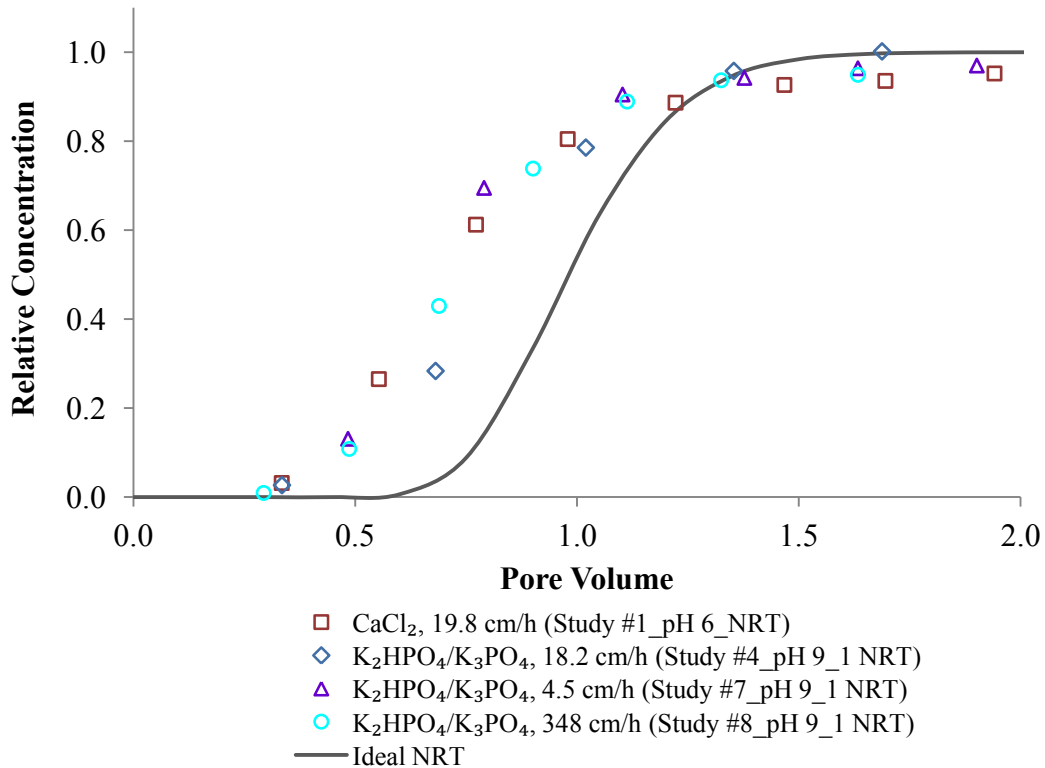


Figure 20: Representative Non-reactive Tracer Studies Illustrating Physical Heterogeneity
Representative non-reactive tracer arrival waves for experiments conducted at pH 6 and pH 9, pore water velocity (4.5, ~ 19, 348 cm/h), and electrolyte type (CaCl₂, K₂HPO₄/K₃PO₄). All experiments conducted at 0.015 M ionic strength. The ideal NRT assumes dispersive fluxes are negligible ($Pe = 50$, $\beta = 1$).

breakthrough of the tracer relative to an ideal NRT arrival wave (simulated herein for comparison). Specifically, that simulated breakthrough curve illustrates transport behavior under "idealized" conditions such that the impact of physical heterogeneity in the system on overall transport behavior is negligible. Modeling of measured NRT transport results indicates the degree of non-ideality measured is small, such that the fraction of flow in the mobile domain (83%) dominates transport through this porous media (i.e. $\beta = 0.83$). The nonideality observed in these tracer studies is a direct result of physical heterogeneities present in the system and is likely due to some preferential flow pathways, velocity variability, and solution movement between the mobile and immobile domain of the porous media. A non-uniform flow front in the influent end of the apparatus employed in these experiments may have resulted in the measured non-ideal transport behavior. While these results show a relatively small degree of nonideality (with 83% of the flow occurring in the mobile domain), a comparison of transport behavior under the various experimental conditions show reproducibility. These results suggest the impacts of *physical heterogeneity* on solute transport behavior are independent of pH, pore water velocity, and the electrolytes employed in these transport experiments.

Physical and Chemical Heterogeneity

A comparison of Al₂O₃ nanoparticle transport curves to those measured for the non-reactive tracer is shown in Figure 21. These results indicate both physical and

chemical heterogeneity is contributing to the overall transport behavior of Al_2O_3 nanoparticles through this porous media. One additional physical transport phenomena Al_2O_3 may experience (not evidenced by PFBA as a NRT) is associated

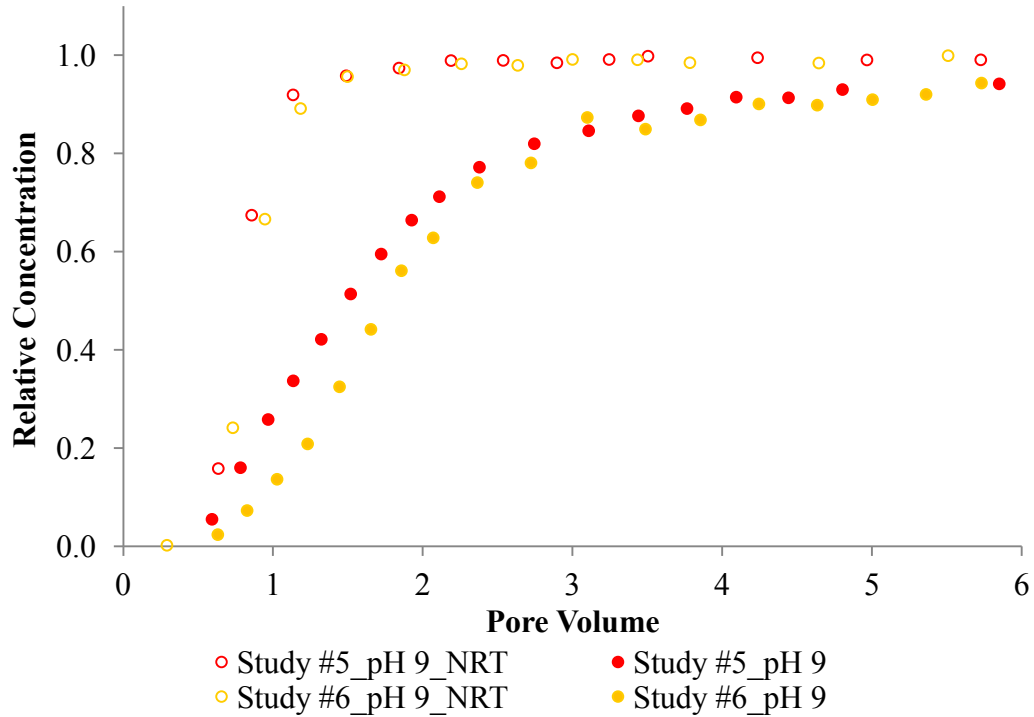


Figure 21: Al_2O_3 Arrival Waves Illustrating Physical and Chemical Heterogeneity Relative to NRT Physical Heterogeneity

Representative non-reactive tracer arrival waves compared to representative Al_2O_3 arrival waves illustrating the impact of physical and chemical heterogeneity on overall transport behavior.

physical straining. While straining has been shown to occur when $d_p/d_{50} > 0.0017$, it is not expected to occur in these systems as the $d_p/d_{50} < 0.0004$, an order of magnitude smaller than what has been observed in the literature (51). The impact of physical heterogeneities (illustrated by the NRT) is likely to be similar across both pH 6 and pH 9

experiments such that the observed nanoparticle transport behavior is likely due to the presence of on-going chemical phenomena (e.g., attachment, blocking).

Favorable and Unfavorable Attachment Conditions (pH 6 and pH 9)

A comparison of aluminum oxide (γ - Al_2O_3) nanoparticle transport measured at pH 6 and pH 9 shows markedly different colloid transport behavior in porous media under favorable versus unfavorable attachment conditions as illustrated in Figure 22. As with other metal oxides, γ - Al_2O_3 exhibits amphoteric behavior with a zero point of charge occurring at pH 8 such that at pH 9 conditions are unfavorable for nanoparticle attachment to the porous media as the nanoparticles and porous media carry an overall negative surface charge. Miscible displacement experiments performed at pH 9 (unfavorable attachment) showed a gently sloping, nearly linear, pseudo-steady state ($C/C_0 = 0.95 - 0.98$) occurring within approximately 5 pore volumes of injection.

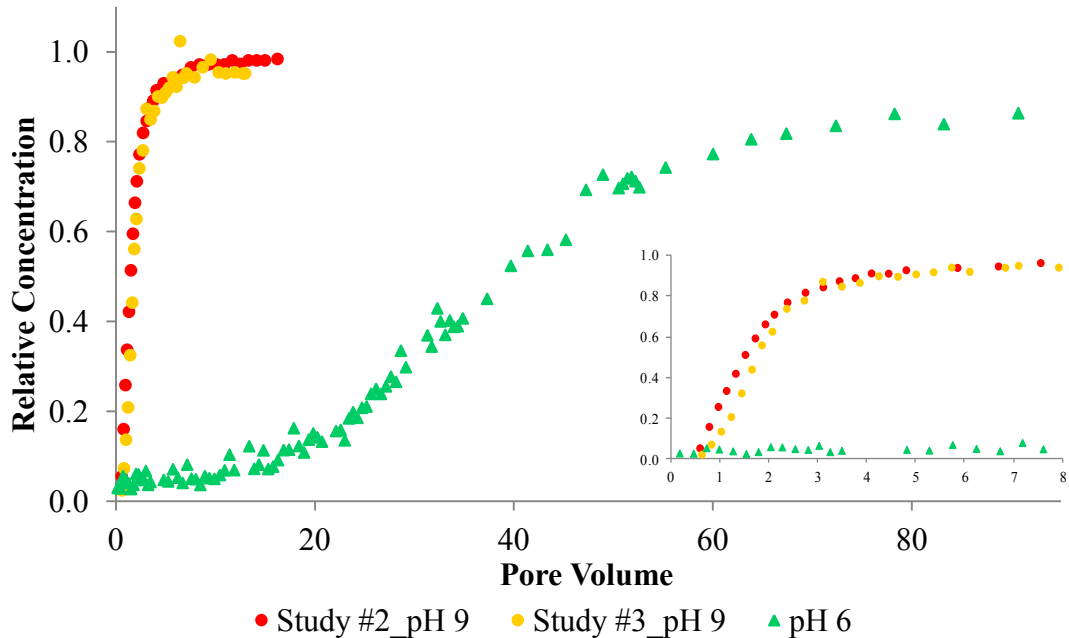


Figure 22: Al₂O₃ Arrival Waves- Favorable (pH 6) and Unfavorable Attachment (pH 9)
 Aluminum oxide solutions at pH 9 were 100 mg/L in a K₂HPO₄/K₃PO₄ (IS= 0.015 M) solution. The pH 6 experiment, conducted previously in our research group, used a 125 mg/L aluminum oxide solution in CaCl₂ (IS = 0.015 M). Experimental flow rate was 0.5 mL/min (pH 9 $v \approx 17.5$ cm/h; pH 6 $v = 18.4$ cm/h) for all three experiments.

In contrast, column experiments previously performed by researchers in our group under favorable attachment conditions (pH 6), where γ - Al₂O₃ is positively charged and the porous media is negatively charged, showed that a significantly larger injection pulse (greater than 70 pore volumes) was required to reach a gently sloping approach towards complete breakthrough.

Moment analysis performed on the arrival wave, under unfavorable attachment (pH 9), shows that 10% of Al₂O₃ nanoparticles are retained in the system. In contrast, 52% of the nanoparticle mass injected is held up in the system under favorable attachment conditions (pH 6). Retardation is significantly less under unfavorable

attachment conditions and likely due to the electrostatic repulsion between Al_2O_3 nanoparticles and the porous media. Those particles retained under unfavorable conditions are likely the result of multiple retention mechanisms including porous media geophysical heterogeneities and nanoparticle attachment in the secondary energy minimum. Surface charge heterogeneity is believed to play a part in attachment observed under unfavorable conditions wherein areas of positive surface charge, or favorable attachment sites located on the overall negatively-charged surface of the collector, may result in a larger retention of particles than predicted (i.e. negatively charged Al_2O_3 nanoparticles may attach) (41, 52, 59). Additionally, when surface charge heterogeneity is masked, deposition still occurs and is believed the result of deposition in the secondary energy well (50, 52).

Many researchers have focused on the initial stage of deposition under “clean bed” conditions, when processes contributing to colloid deposition are “simplest”, using short input pulses and high approach velocities not typically observed in groundwater flow. In contrast, the large injection volumes or input pulses employed in these nanoparticle transport experiments aimed to fully characterize long-term transport behavior at approach velocities typical of groundwater flow.

As described above, breakthrough curves of Al_2O_3 under unfavorable attachment conditions (pH 9) show a nearly linear approach to a pseudo-steady state relative concentration of ~ 0.95 within ~ 5 pore volumes of injection. These results are congruent to those presented in nanocolloid transport research conducted at similar darcy velocities,

employing nanocolloids of like size and shape, and electrolyte ionic strength (25, 49, 52, 78, 79, 93). For example, breakthrough curves (previously shown in Figure 18) of negatively charged 100 nm Fe_2O_3 (IS = 0.03 M) demonstrated a gently sloping, nearly linear approach to complete breakthrough within approximately 3 pore volumes of injection.

The nanoparticle transport curves under favorable attachment conditions (pH 6) as presented herein are markedly different from those typically reported in the literature. Specifically, our breakthrough curves show an early, low-concentration steady-state plateau followed by a gently-sloping rising limb with greater than 70 pore volumes required to reach complete breakthrough. In contrast, for example, breakthrough curves of positively-charged colloids, such as those of model latex colloids shown previously in Figure 9, exhibit a very sharp rising limb in the arrival wave with a fast approach to a steady-state relative concentration. Additionally, breakthrough curves from nanoparticle transport experiments (Figure 19) using positively-charged 123-nm Al_2O_3 displayed complete breakthrough ($C/C_0 = 1$) but not the early low-concentration steady-state behavior as observed in our Al_2O_3 transport experiments (see Figure 22). The approach velocities employed in these transport studies are ~80-fold higher ($U = 8.2$ cm/min and 6.0 cm/min, respectively) than in our transport studies ($U = 0.10$ cm/min) and employ markedly smaller input pulses such that they may not be able to fully characterize transport behavior associated with long-term transport at natural groundwater velocities. Interestingly, transport studies conducted previously in our research group using 100

mg/L Al_2O_3 in nanopure water at pH 6 showed that as pore-water velocity increased from 18 to 217 cm/h the resulting breakthrough curves become increasingly similar to that found in the literature (Figure 23). Finally, transport experiments using large injection pulses, while still employing large approach velocities, have the ability to characterize long-term transport behavior, but at approach velocities typical of engineered systems, not natural groundwater systems.

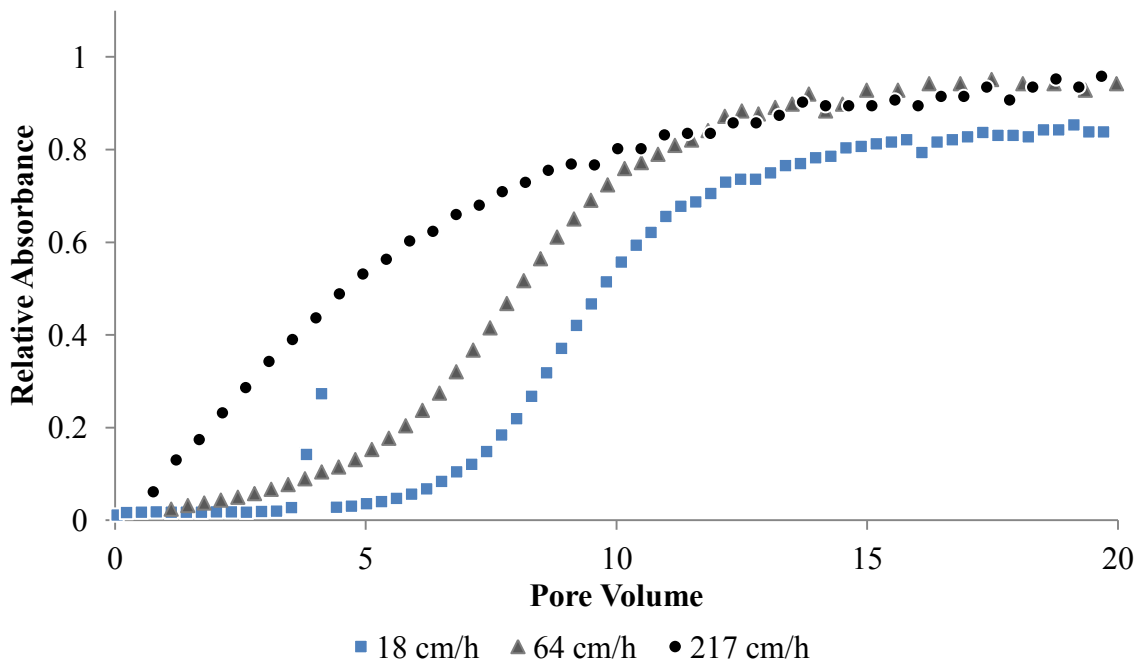


Figure 23: High velocity Al_2O_3 Nanoparticle Breakthrough Curve ($v = 217$ cm/h) – Favorable Attachment

Experiments conducted using 100 mg/L Al_2O_3 in pH 6 nanopure water at three different pore water velocities: 18, 64, and 217 cm/h.

A 2003 aquifer tank experiment using 150-nm silica-coated zirconia, employing large injection pulses and approach velocities similar to this current research, is, at the

time of this thesis, the only nanoparticle transport study to present breakthrough curves similar to this current research (41). The silica-coated zirconia breakthrough curves (Figure 4) demonstrate the same low-concentration steady-state transport behavior and gently sloping approach to complete breakthrough as observed in the pH 6 Al_2O_3 breakthrough curve shown in Figure 22.

Linear Pore Water Velocity

Transport experiments conducted under unfavorable attachment conditions (pH 9) at three average linear pore water velocities (4.5, 17.5, and 338 cm/h) show initial breakthrough within one pore volume and an approach to complete breakthrough within 5 pore volumes of injection (Figure 24). The mass retained within each system is small

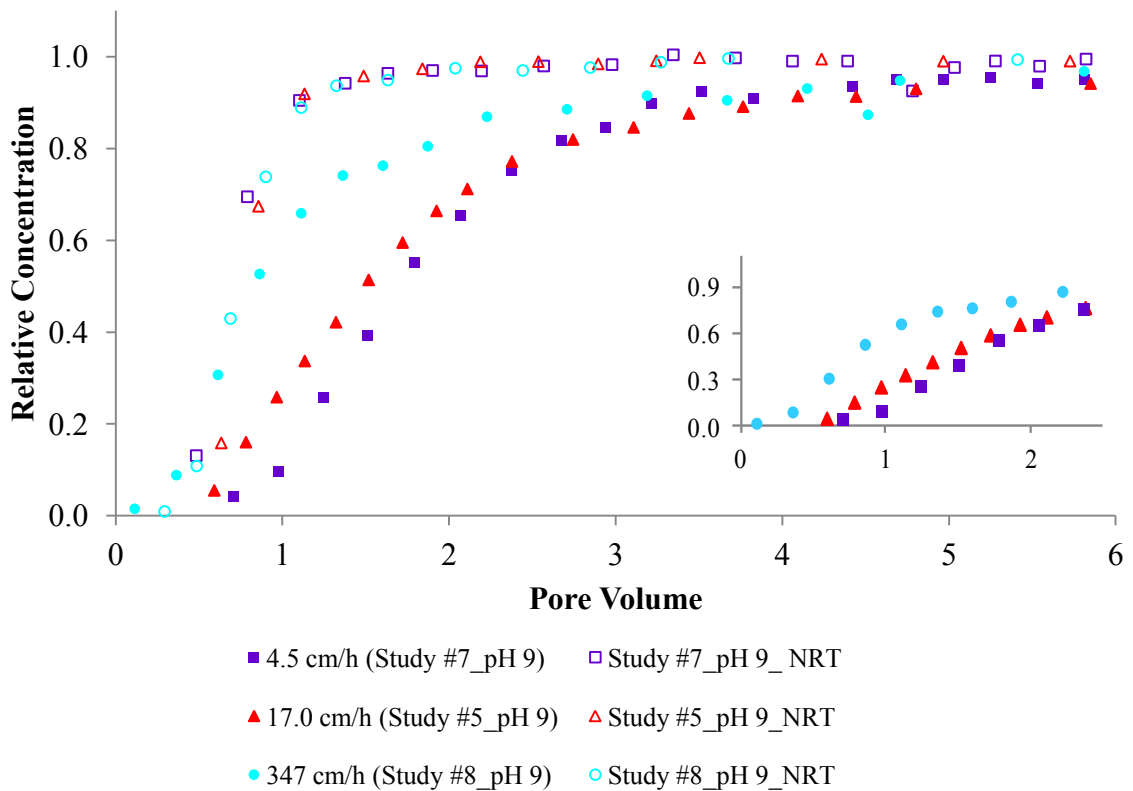


Figure 24: Characterization of Velocity Effects on Transport Behavior of Al_2O_3 – Unfavorable Conditions (pH 9)

These unfavorable attachment transport experiments were performed using 100 mg/L Al_2O_3 in $\text{K}_2\text{HPO}_4/\text{K}_3\text{PO}_4$ (IS = 0.015 M) buffer solution at a darcy velocity of approximately 0.03, 0.10, and 1.8 cm/min ($v = 4.5, 17.5, 338$ cm/h).

(5-13%) under these unfavorable attachment conditions and is likely associated with deposition in the shallow secondary energy minimum and/or surface charge heterogeneity on the sand grain surfaces. All variable flow experiments exhibit some degree of tailing on the nanoparticle transport arrival wave as evidenced on comparing that transport arrival wave to that observed for the non-reactive tracer. The higher flow (338 cm/h) breakthrough curve showed slightly earlier breakthrough than the lower flow (4.5, 17.5

cm/h) breakthrough curves, suggesting deposition is kinetically controlled (see inset Figure 24). This proposed kinetically-controlled deposition behavior is supported by concentration effects observed on the arrival wave following minor stop flow (5 – 10 minute) experiments during the high flow (329 cm/h) transport study (Figure 25a). Furthermore, a six-day stop flow experiment conducted during the low flow (4.5 cm/h) transport study exhibits a significant effect on measured column effluent concentrations (Figure 25b). Variable flow experiments (discussed previously) conducted within our research group under favorable attachment conditions (pH 6) also exhibit slightly earlier breakthrough at higher flow (see Figure 23) and concentration effects during stop flows (Figure 26). These results indicate Al_2O_3 nanoparticle deposition may be kinetically controlled irrespective of pH.

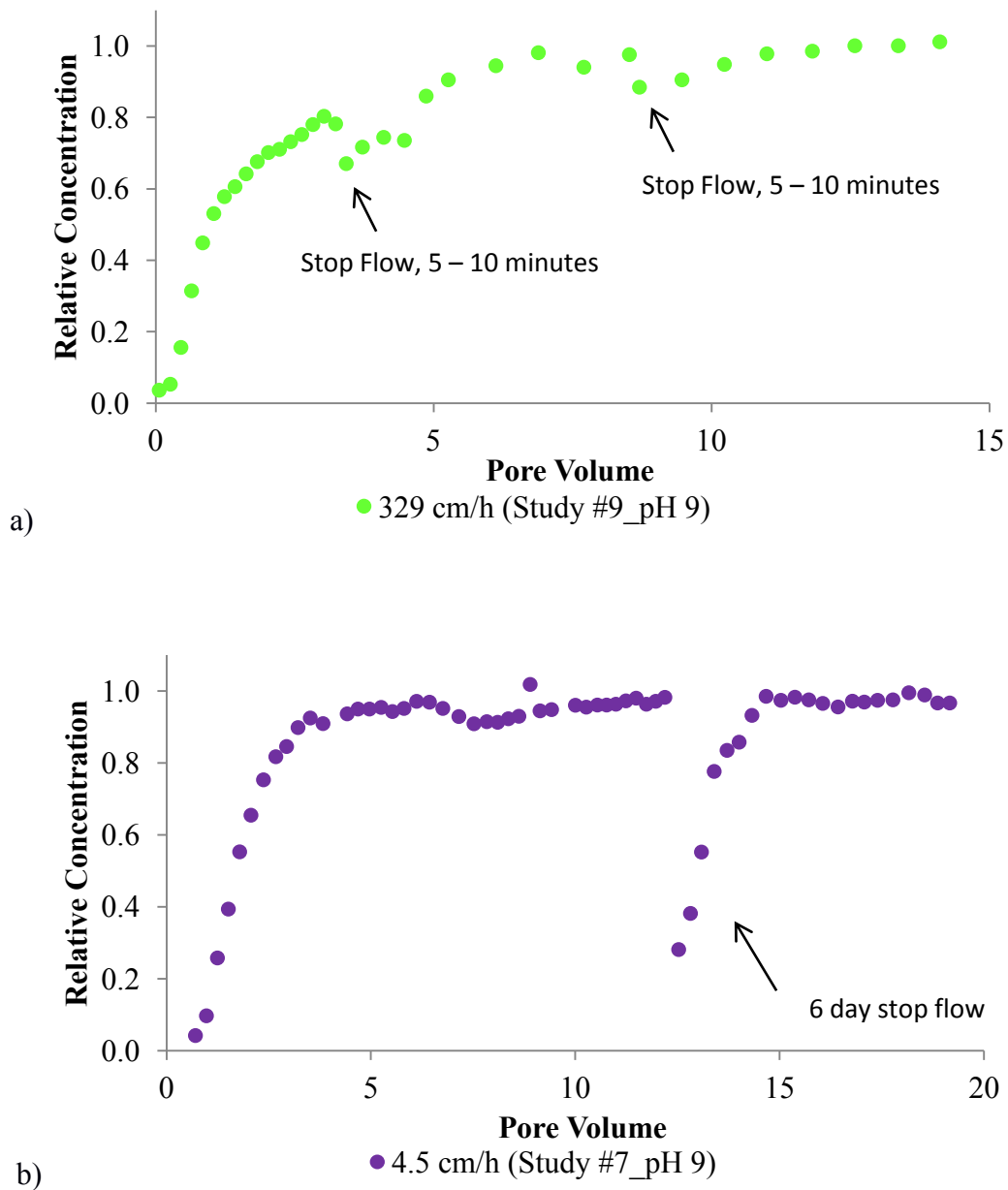


Figure 25: Concentration effects upon stop flow events – Unfavorable Attachment
 Stop flow events ranged from 5 – 10 minutes to approximately 1 week using 100 mg/L Al_2O_3 in $\text{K}_2\text{HPO}_4/\text{K}_3\text{PO}_4$ (IS = 0.015M) buffer solution. (a) Two small stop flows conducted during a high velocity ($v = 329$ cm/h) transport experiment (pH 9.4). (b) Six day stop flow conducted during a low velocity ($v = 4.5$ cm/h) transport experiment (pH 9.1).

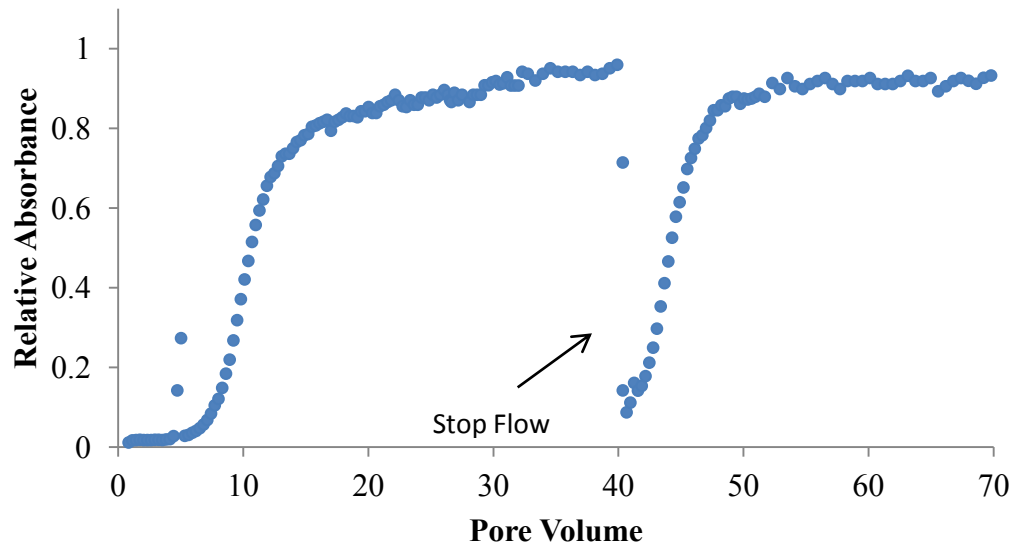


Figure 26: Stop Flow, Favorable Attachment Conditions (pH 6)

Stop flow experiment conducted at pH 6 illustrating rate-limited Al_2O_3 nanoparticle deposition. Experiment conducted using 100 mg/L Al_2O_3 in deionized water and a linear pore-water velocity of 18 cm/h.

Aqueous-Phase Concentration

The results of nanoparticle transport experiments under favorable attachment conditions (pH 6) and three different aqueous-phase concentrations are shown in Figure 27. As Al_2O_3 aqueous concentration decreased breakthrough times increased, with the low concentration experiment (25 mg/L) requiring greater than 500 pore volumes to reach a gently sloping approach to complete breakthrough at pH 6. Higher aqueous concentration resulted in a faster approach to dynamic deposition conditions with a gently sloping approach to complete breakthrough occurring within approximately 40 pore volumes (see inset in Figure 27).

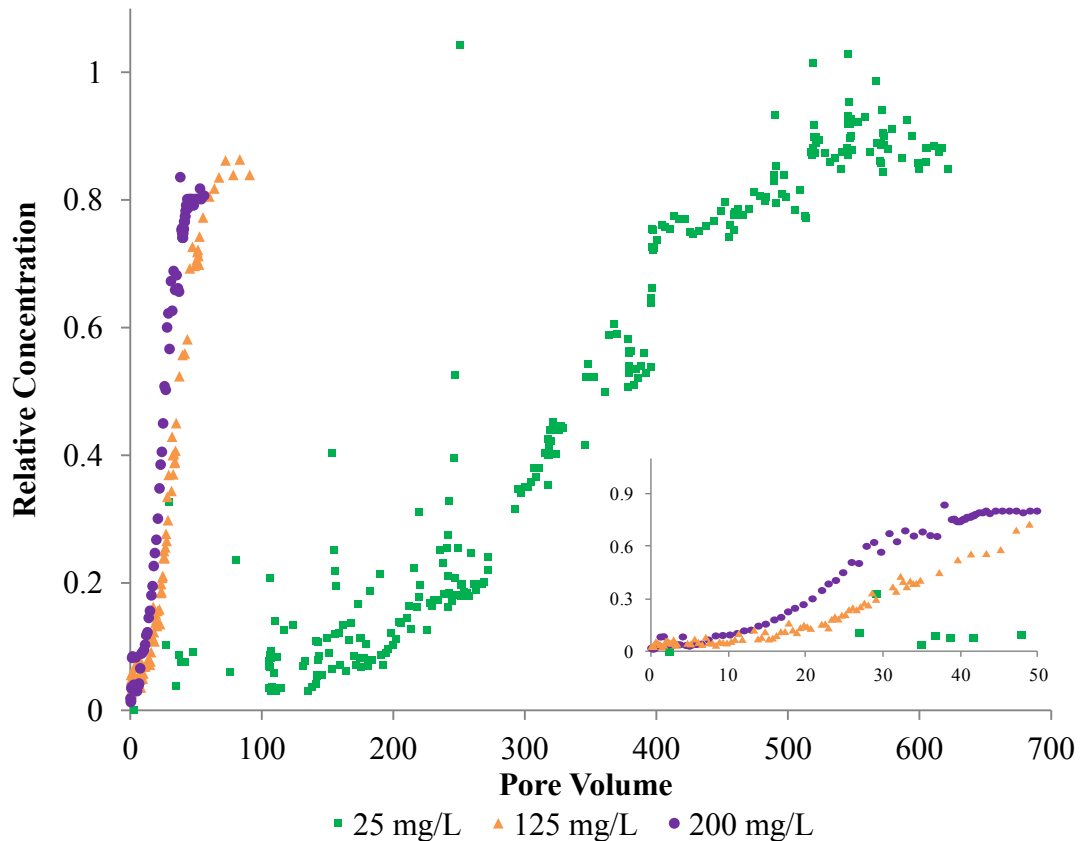


Figure 27: Al₂O₃ aqueous-phase concentration transport studies

Transport studies conducted at pH 6 using 25 mg/L Al₂O₃ (Study #2_ pH 6), 125 mg/L Al₂O₃ (conducted previously in our research group), and 200 mg/L Al₂O₃ (Study #1_ pH 6) in a CaCl₂ electrolyte (IS = 0.015 M); darcy velocity approximately 0.1 cm/min ($v = 18.4 - 19.8$ cm/h).

The onset of blocking wherein the transport of nanoparticles transitions from an early, low-concentration, steady-state plateau to “dynamic” transport conditions occurs within 10 pore volumes of injection in the 125 and 200 mg/L Al₂O₃ experiment, while the 25 mg/L experiment requires ~100 pore volumes of injection. Similar to our Al₂O₃ transport curves, Liu et al. (1995) found the approach to a long-term, high relative concentration of 0.48- μ m latex particles occurred faster as colloid concentration

increased (42) as shown previously (Figure 5). This behavior was attributed to the limited availability of attachment sites on the collectors such that the onset of blocking, where deposited particles impact attachment of subsequent particles (40), occurs more quickly as concentration increases. Our Al₂O₃ results are likely due to the limited availability of attachment sites on the porous media such that increasing the nanoparticle concentration results in filling those attachment sites over a smaller input pulse.

Colloid filtration theory assumes that the rate of particle attachment to the collector surface is independent of particle concentration. That theory is supported by results herein. Specifically, while the time to achieve the long-term, steady state high concentration increases with decreasing aqueous-phase concentration, the total mass retained in the system is independent of concentration as shown in Figure 28. The fraction of mass retained shows a similar linear relationship to the mass injected across all three aqueous-phase concentrations and is followed by decreasing retention (gently sloping curve) as the system approaches complete breakthrough. While the input pulse increases with decreasing nanoparticle concentration the total mass retained in the system upon reaching complete breakthrough is similar.

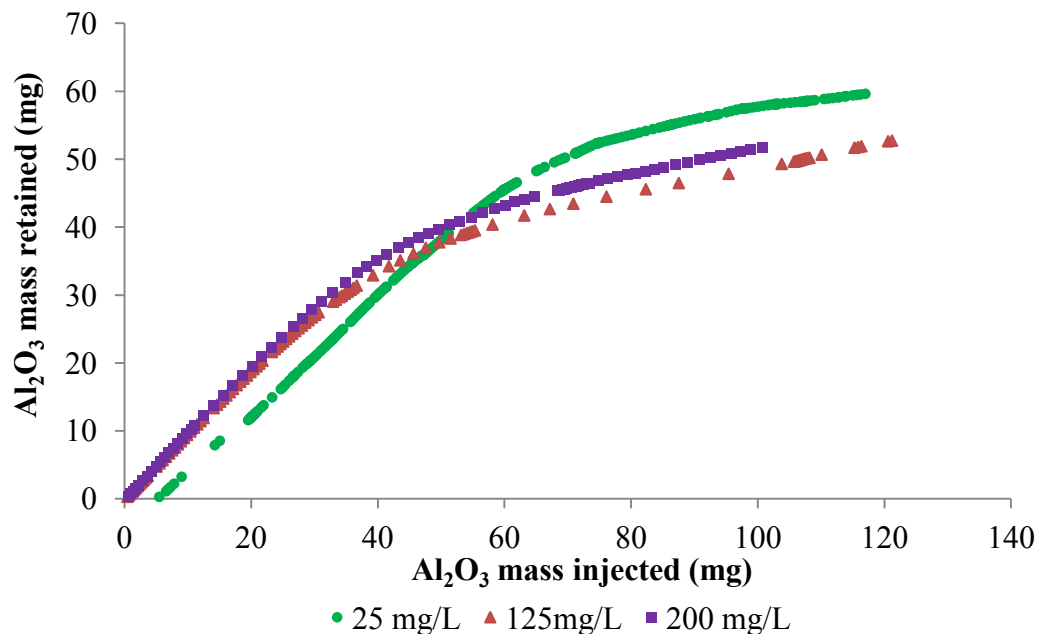


Figure 28: Total mass Al₂O₃ nanoparticles retained relative to the total mass injected at three different aqueous phase concentrations

Electrolyte – Monovalent Versus Divalent Cation

A 100 mg/L Al₂O₃ nanoparticle transport study at pH 6 in a 0.015 M electrolyte solution of KCl was conducted and compared to that measured under similar experimental conditions using a 0.015 M electrolyte solution of CaCl₂. Initial breakthrough of nanoparticles using the monovalent electrolyte (KCl) occurred within one pore volume of injection similar to that initial breakthrough observed using the divalent electrolyte (CaCl₂). With the onset of the dynamic transport phase (i.e., the onset of blocking), the Al₂O₃ transport measured using the KCl electrolyte solution diverged from that measured for using CaCl₂. Specifically, the transition from the low-

concentration, steady-state behavior to dynamic transport conditions in the KCl experiment is not as sharp/steep as that observed for the CaCl₂ experiment (Figure 29).

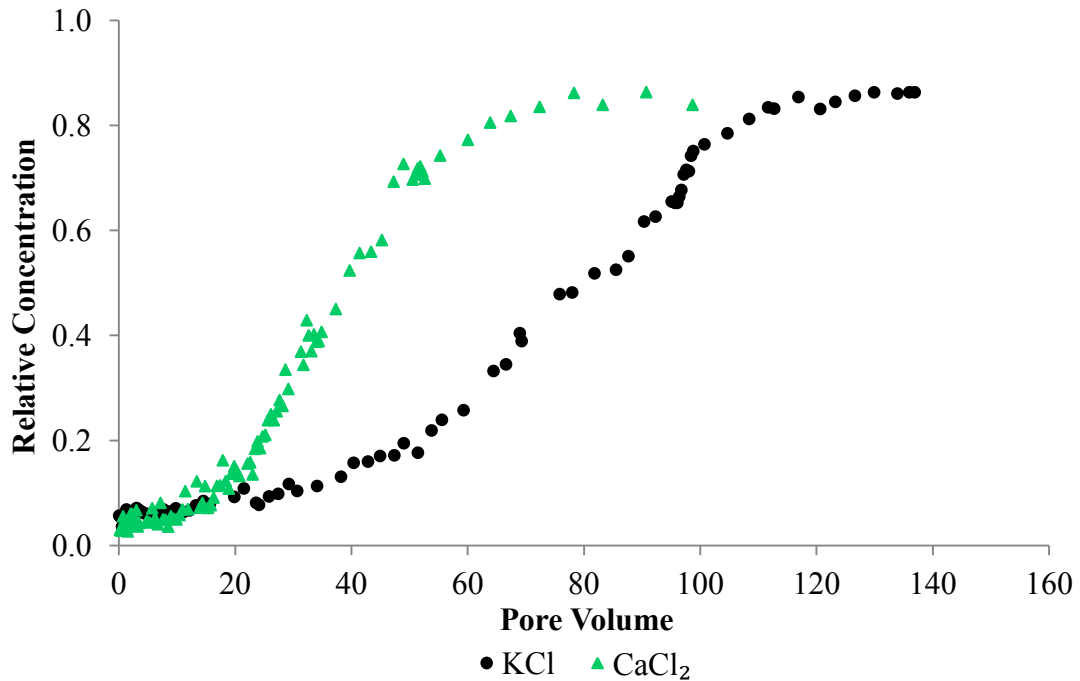


Figure 29: Comparison of Al₂O₃ transport using a monovalent (KCl) and divalent (CaCl₂) electrolyte solution

Both transport studies conducted at pH 6 using 100 mg/L Al₂O₃ in either KCl or CaCl₂ electrolyte solutions (IS = 0.015 M) and at an average linear pore water velocity of 19 cm/h. The KCl transport study corresponds to Study #3_ pH 6 in this thesis while CaCl₂ transport study was conducted previously within our research group.

A sharp transition occurs within approximately 20 pore volumes in the CaCl₂ study with a steep slope and approach to a long-term, steady-state plateau approaching complete breakthrough. Conversely, the observed transition in the KCl study is less sharp requiring nearly twice the number of injection-solution pore volumes to begin a high-concentration plateau condition. The two studies reach a similar long-term high concentration state at $C/C_0 = 0.83 - 0.86$ but the KCl study required approximately 150 pore volumes of

solution injection whereas the CaCl_2 study required only 80 pore volumes to reach the same relative concentration.

Experimental conditions were similar for these two transport studies (e.g., ionic strength, flow velocity, aqueous-phase concentration) apart from the presence of mono- versus divalent cations in solution and the differences in ion species concentrations. Although ionic strength was the same, the K^+ molar concentration (0.015 M) was three times higher than the Ca^{2+} molar concentration (0.005 M) while the anion concentrations were similar ($\text{Cl}^-_{\text{CaCl}_2} = 0.01\text{M}$ and $\text{Cl}^-_{\text{KCl}} = 0.015\text{M}$). A comparison of transport behavior for these two cations in solution at more similar concentrations is shown in Figure 30. The KCl transport study demonstrates similar behavior to a higher ionic strength (IS = 0.030 M) CaCl_2 transport study conducted within our research group. Again, the Cl^- concentrations are similar in these two studies ($\text{Cl}^-_{\text{KCl}} = 0.015\text{ M}$ and $\text{Cl}^-_{\text{CaCl}_2} = 0.02\text{ M}$) and are not believed to be impacting transport behavior. Overall these results suggest it is the cation (irrespective of valence) dominantly affecting/contributing to nanoparticle deposition to this porous media. As that cation concentration increases, from 0.005 M to 0.015 M, deposition of Al_2O_3 nanoparticles increases, resulting in greater retardation on transport through the porous media.

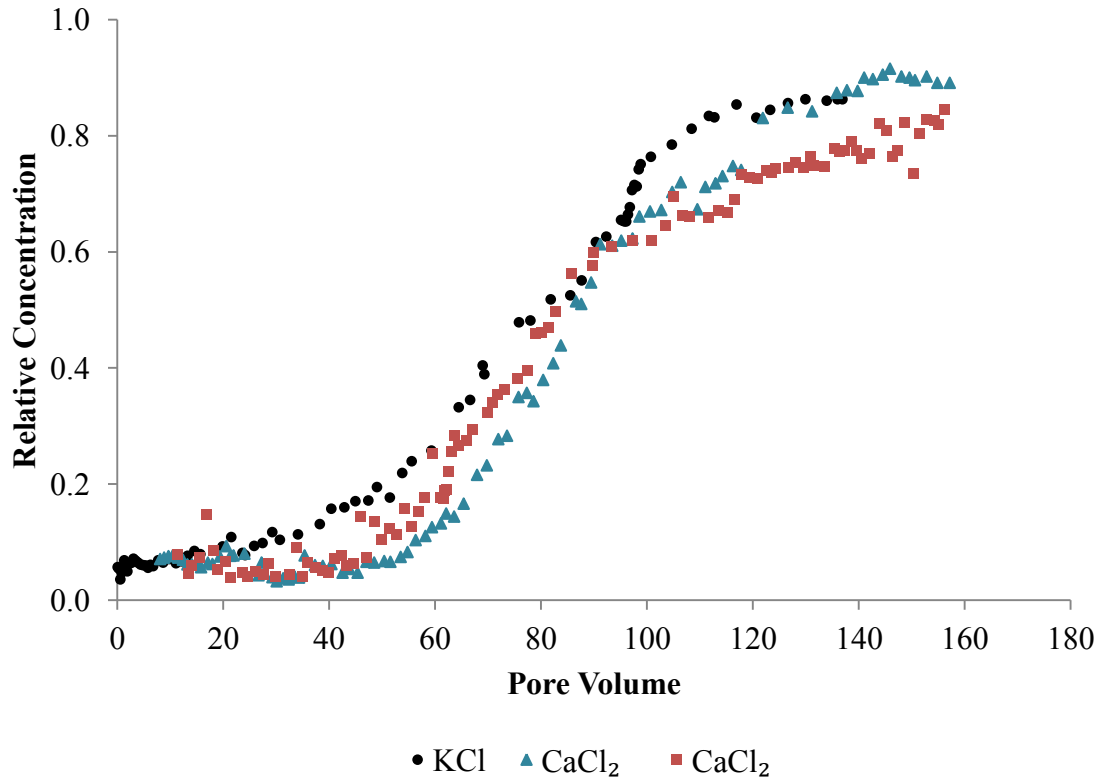


Figure 30: Comparison of Al_2O_3 Transport Study in KCl to a Higher Ionic Strength Study using CaCl_2

All three transport studies conducted at pH 6 using 100 mg/L Al_2O_3 in either KCl (IS = 0.015 M) or CaCl_2 (IS = 0.030 M) electrolyte solutions and at an average linear pore water velocity of 19 cm/h. The KCl transport study corresponds to Study #3_ pH 6 in this thesis while the CaCl_2 transport studies were conducted previously within our research group.

Collector Efficiency/First-order Reaction Rate Coefficient

Classic colloid filtration theory speaks to the early deposition behavior at the initial stages of deposition with the assumption that the deposition rate coefficient (k_d) is constant. This assumption points to a period, at this initial stage of deposition, where the relative effluent concentration is constant, occurring before the onset of blocking and the

transition to “dynamic” transport conditions. The early low-concentration, steady-state transport behavior observed in the pH 6 Al_2O_3 nanoparticle breakthrough curves, as highlighted in Figure 31, are in accordance with conditions under which deposition is deemed constant. Theoretical collector efficiencies predicted using various colloid

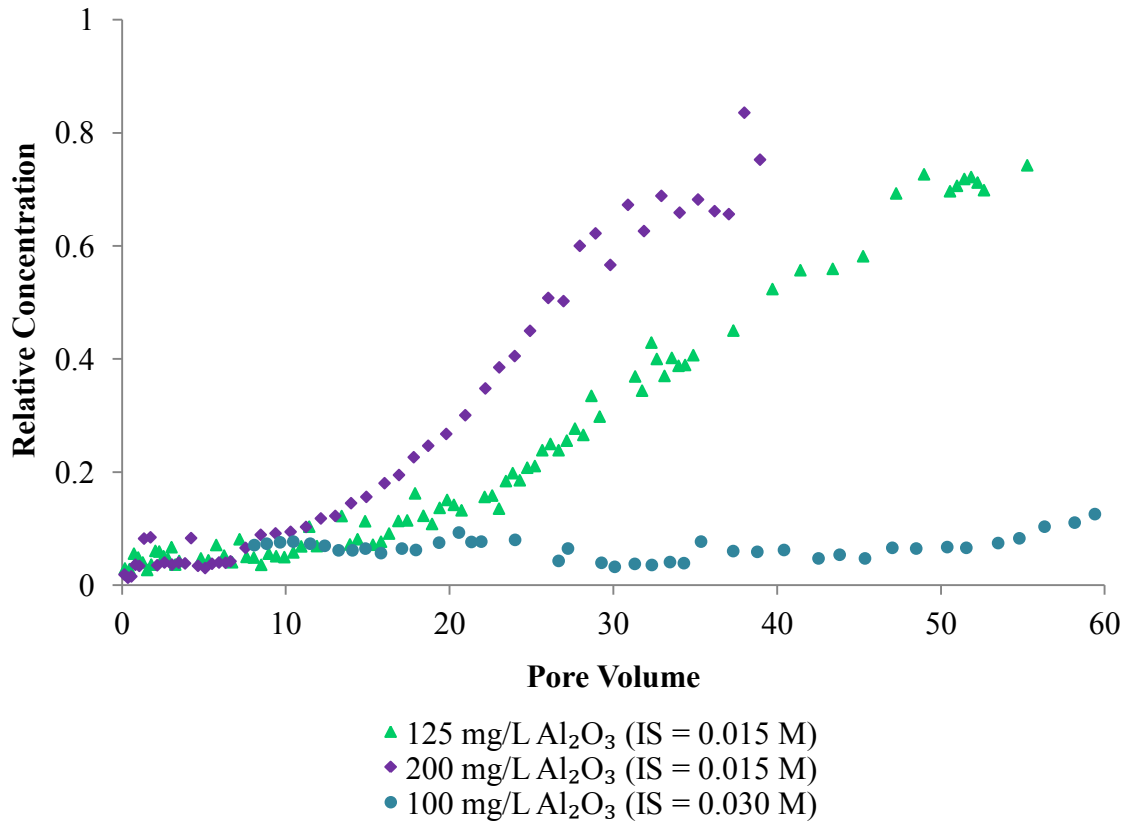


Figure 31: Al_2O_3 Early Transport Behavior – Favorable Attachment Conditions

The 200 mg/L Al_2O_3 transport experiment is Study pH 6_1 with the remaining experiments previously conducted within our research group. All experiments conducted at pH 6 and a darcy velocity of 0.10 cm/min ($v = 18.4 - 20.2$ cm/h).

deposition models and compared to those determined experimentally are shown in Table 4 and Table 5. The Yao model (30) consistently under-predicted our experimental results while the Tufenkji and Elimelech model (32) over-predicted Al_2O_3 deposition relative to our experimentally determined single-collector efficiencies across all aqueous-phase concentrations (25 – 200 mg/L) and ionic strength (0.015 – 0.030 M) conditions (Table 4).

Table 4: Theoretical single-collector efficiencies (η) compared to experimental single-collector efficiencies (η_{exp}) from Al_2O_3 pH 6 nanoparticle transport experiments

Al_2O_3 Concentration (mg/L)	Ionic Strength (M)	Yao et al. (30) η	Tufenkji and Elimelech (32) η	η_{exp}
25	0.015	0.017	0.050	0.044
125	0.015	0.017	0.050	0.048
125	0.015	0.017	0.051	0.042
200	0.015	0.017	0.052	0.044
100	0.030	0.018	0.037	0.031
100	0.030	0.019	0.038	0.033

Conversely, the Nelson and Ginn model (43) consistently under-predicted collector efficiencies relative to those experimentally-determined values across the same experimental conditions (Table 5). The discrepancy between these models as a predicting tool for deposition under clean bed conditions as compared to experimentally-determined deposition results are similar to those previously reported.

Table 5: Theoretical collector efficiencies (η) compared to experimental collector efficiencies (η_{exp}) from Al₂O₃ pH 6 nanoparticle transport experiments

Concentration (mg/L)	Ionic Strength (M)	Nelson and Ginn (43) η	η_{exp}
25	0.015	0.025	0.034
125	0.015	0.026	0.038
125	0.015	0.025	0.033
200	0.015	0.027	0.035
100	0.030	0.019	0.024
100	0.030	0.020	0.026

Across all pH6 Al₂O₃ nanoparticle transport experiments conducted within our research group, the Yao model under-predicts the reaction rate coefficient by 69 – 189 %, the Tufenkji and Elimelech model over-predicts by 4 – 17 %, and the Nelson and Ginn model under-predicts by 26 – 49 % (Table 6). These results are in relative agreement to what Nelson and Ginn (2011) found when comparing the Tufenkji and Elimelech (2004) model and their own model with experimental data wherein the TE model over-predicted reaction rate coefficients, particularly for nanoscale particles, while the NG model was found to under-predict primarily in the sub-micron size region.

Table 6: Experimental and Theoretical Reaction Rate Coefficients– Favorable Attachment Condition Experiments (pH 6)

Al ₂ O ₃ Concentration (mg/L)	Ionic Strength (M)	<i>k_d</i> experimental (s ⁻¹)	Yao et al. (30)		Tufenkji & Elimelech (32)		Nelson & Ginn (43)	
			<i>k_d</i> predicted (s ⁻¹)	% Difference	<i>k_d</i> predicted (s ⁻¹)	% Difference	<i>k_d</i> predicted (s ⁻¹)	% Difference
25	0.015	0.0033	0.0013	-155	0.0038	12	0.0025	-36
125	0.015	0.0040	0.0014	-189	0.0041	4	0.0027	-49
125	0.015	0.0031	0.0013	-142	0.0037	17	0.0024	-28
200	0.015	0.0036	0.0014	-158	0.0043	15	0.0028	-31
100	0.03	0.0025	0.0015	-69	0.0030	17	0.0020	-26
100	0.03	0.0027	0.0015	-77	0.0031	14	0.0020	-31

CONCLUDING REMARKS

Colloid filtration theory (typically) describes the initial stages of deposition under “clean bed” conditions while assuming a monodisperse colloid in a monovalent electrolyte solution. Additionally, the theory assumes spherical colloids and collectors of uniform surface charge. In contrast, the Al_2O_3 in this research is a polydisperse nanocolloid. Furthermore, the porous media employed here is a natural porous media, and while a fairly uniform quartz sand, does contain a small amount of metal oxide impurities within the crystalline structure and likely does not have a uniform surface charge. For example, scanning electron microscopy (SEM) analysis of the Accusand employed in these transport experiments showed quartz sand grains with rough heterogeneous surfaces and metal impurities (e.g., iron and aluminum oxide). While our experimental conditions are not ideal with regard to what is typically assumed under colloid filtration theory, the transport behavior observed, for the most part, supports colloid filtration theory. More importantly, the large input pulses and smaller approach velocities employed in our transport studies serve to illustrate that Al_2O_3 nanoparticles are mobile across the range of chemical conditions employed in these experiments. Future research will further examine the impact of counterion valence on transport of positively charged Al_2O_3 nanoparticles using a CaSO_4 electrolyte solution under the same experimental conditions as our pH 6 experiments using CaCl_2 . Additionally, transport experiments will be performed using, again under favorable attachment conditions, to ascertain what impact, if any, a multi-valent counter anion has on Al_2O_3 nanoparticle

transport. Measurement of the impact of natural organic matter, in the form of humic acid, and the subsequent effect on the overall transport behavior of these Al_2O_3 nanoparticles will also be assessed.

This current research has shown that, under environmentally relevant groundwater conditions, nanocolloids associated with biosolids, specifically Al_2O_3 , are mobile through saturated porous media. Mobility increased under conditions in which the nanoparticles and porous media were of like charge; observed under high pH conditions such as those occurring with the land-application of lime-stabilized biosolids. The use of calcium chloride electrolyte solution in transport studies resulted in enhanced mobility relative to potassium chloride suggesting that changes in groundwater solution chemistry could impact mobility of contaminants associated with biosolids. Given the ubiquity of nano-scale materials, in particular nano-particles, in the environment coupled with the expected increases in biosolid generation and land-application, a clear understanding of their transport and fate is necessary to assess the potential for contaminant transport and the facilitated transport of toxins through the subsurface and into our surface and groundwater bodies.

REFERENCES

1. Daughton, C. G.; Ternes, T. A. Pharmaceuticals and Personal Care Products in the Environment: Agents of Subtle Change? *Environmental Health Perspectives* 1999, *107*, 907-938.
2. Kolpin, D. W.; Furlong, E. T.; Meyer, M. T.; Thurman, E. M.; Zaugg, S. D.; Barber, L. B.; Buxton, H. T. Pharmaceuticals, Hormones, and Other Organic Wastewater Contaminants in U.S. Streams, 1999-2000: A National Reconnaissance. *Environmental Science and Technology* 2002, *36*, 1202-1211.
3. Ellis, J. B. Pharmaceutical and personal care products (PPCPs) in urban receiving waters. *Environmental Pollution* 2006, *144*, 184-189.
4. Yu, C.-P.; Chu, K.-H. Occurrence of pharmaceuticals and personal care products along the West Prong Little Pigeon River in east Tennessee, USA. *Chemosphere* 2009, *75*, 1281-1286.
5. Dougherty, J. A.; Swarzenski, P. W.; Dinicola, R. S.; Reinhard, M. Occurrence of Herbicides and Pharmaceutical and Personal Care Products in Surface Water and Groundwater around Liberty Bay, Puget Sound, Washington. *Journal of Environmental Quality* 2010, *39* (4), 1173-1180.
6. Schultz, M. M.; Furlong, E. T.; Kolpin, D. W.; Werner, S. L.; Schoenfuss, H. L.; Barber, L. B.; Blazer, V. S.; Norris, D. O.; Vaida, A. M. Antidepressant pharmaceuticals in two U.S. effluent-impacted streams: occurrence and fate in water and sediment, and selective uptake in fish neural tissue. *Environmental Science and Technology* 2010, *44* (6), 1918-1925.
7. Morace, J. L. *Reconnaissance of Contaminants in Selected Wastewater-Treatment-Plant Effluent and Stormwater Runoff Entering the Columbia River, Columbia River Basin, Washington and Oregon, 2008-10*; U.S. Geological Survey Scientific Investigations Report 2012-5068, 2012.
8. Cientifica Ltd. *Half Way to the Trillion Dollar Market? A Critical Review of the Diffusion of Nanotechnologies*; London, 2007.
9. Zhang, T. C.; Surampalli, R. Y.; Lai, K. C. K.; Hu, Z.; Tyagi, R. D.; Lo, I. M. C. *Nanotechnologies for Water Environment Applications*; American Society of Civil Engineers: Reston, 2009.

10. U.S. Environmental Protection Agency. *Biosolids Generation, Use, and Disposal in The United States*; U.S. EPA Municipal and Industrial Solid Waste Division: EPA 530-R-99-009, 1999.
11. North East Biosolids and Residuals Association (NEBRA). *A National Biosolids Regulation, Quality, End Use & Disposal Survey Final Report*; 2007.
12. Xia, K.; Bhandari, A.; Das, K.; Pillar, G. Occurrence and Fate of Pharmaceuticals and Personal Care Products (PPCPs) in Biosolids. *Journal of Environmental Quality* 2005, 34, 91-104.
13. Kinney, C. A.; Furlong, E. T.; Burkhardt, M. R.; Werner, S. L.; Cahill, J. D.; Jorgensen, G. R. Survey of Organic Wastewater Contaminants in Biosolids Destined for Land Application. *Environmental Science and Technology* 2006, 40, 7207-7215.
14. U.S. Environmental Protection Agency. *Targeted National Sewage Sludge Survey: Sampling and Analysis Technical Report*; U.S. Environmental Protection Agency Office of Water: EPA 822-R-08-016, 2009.
15. Chari, B. P.; Halden, R. U. Validation of mega composite sampling and nationwide mass inventories for 26 previously unmonitored contaminants in archived biosolids from the U.S. National Biosolids Repository. *Water Research* 2012, 46, 4814-4824.
16. Jaynes, W. F.; Zartman, R. E. Origin of Talc, Iron Phosphates, and Other Minerals in Biosolids. *Soil Science Society of America Journal* 2005, 69, 1047-1056.
17. Karathanasis, A. D.; Johnson, D. M. C.; Matocha, C. J. Biosolid Colloid-Mediated Transport of Copper, Zinc, and Lead in Waste-Amended Soils. *Journal of Environmental Quality* 2005, 34, 1153-1164.
18. Lapen, D. R.; Topp, E.; Metcalfe, C. D.; Li, H.; Edwards, M.; Gottschall, N.; Bolton, P.; Curnoe, W.; Payne, M.; Beck, A. Pharmaceutical and personal care products in tile drainage following land application of municipal biosolids. *Science of the Total Environment* 2008, 399, 50-65.
19. Edwards, M.; Topp, E.; Metcalfe, C. D.; Li, H.; Gottschall, N.; Bolton, P.; Curnoe, W.; Payne, M.; Beck, A.; Kleywegt, S.; Lapen, D. R. Pharmaceutical and personal care products in tile drainage following surface spreading and injection of dewatered municipal biosolids to an agricultural field. *Science of the Total Environment* 2009, 407, 4220-4230.

20. Gottschall, N.; Topp, E.; Metcalfe, C.; Edwards, M.; Payne, M.; Kleywegt, S.; Russell, P.; Lapen, D. R. Pharmaceutical and personal care products in groundwater, subsurface drainage, soil, and wheat grain, following a high single application of municipal biosolids to a field. *Chemosphere* 2012, 87, 194-203.
21. Grolimund, D.; Borkovec, M.; Barmettler, K.; Sticher, H. Colloid -Facilitated Transport of Strongly Sorbing Contaminants in Natural Porous Media: A Laboratory Column Study. *Environmental Science and Technology* 1996, 30, 3118-3123.
22. Roy, S. B.; Dzombak, D. A. Chemical Factors Influencing Colloid-Facilitated Transport of Contaminants in Porous Media. *Environmental Science and Technology* 1997, 31, 656-664.
23. Karathanasis, A. D.; Ming, D. W. Colloid-Mediated Transport of Metals Associated with Lime-Stabilized Biosolids. *Developments in Soil Science* 2002, 28A, 49-62.
24. de Jong, L. W.; Kjaergaard, C.; Moldrup, P. Colloids and Colloid-Facilitated Transport of Contaminants in Soils: An Introduction. *Vadose Zone Journal* 2004, 3, 321-325.
25. Lecoanet, H. F.; Bottero, J. Y.; Wiesner, M. R. Laboratory Assessment of the Mobility of Nanomaterials in Porous Media. *Environmental Science and Technology* 2004, 38 (19), 5164-5169.
26. Doshi, R.; Braida, W.; Christodoulatos, C.; Wazne, M.; O'Conner, G. Nano-Aluminum: Transport Through Sand Columns and Environmental Effects on Plants and Soil Communities. *Environmental Research* 2008, 106, 296-303.
27. Wang, H.; Wick, R. L.; Xing, B. Toxicity of Nanoparticle and Bulk ZnO, Al₂O₃ and TiO₂ to the Nematode *Caenorhabditis elegans*. *Environmental Pollution* 2009, 157, 1171-1177.
28. Hiemenz, P. C. *Principles of Colloid and Surface Chemistry*, 2nd ed.; Marcel Dekker: New York, 1986.
29. Elimelech, M.; Gregory, J.; Jia, X.; Williams, R. A. *Particle Aggregation and Deposition: Measurement, Modeling, and Simulation*, 1st ed.; Butterworth-Heinemann: Oxford, 1995.
30. Yao, K.; Habibian, M. T.; O'Melia, C. R. Water and Waste Water Filtration: Concepts and Applications. *Environmental Science and Technology* 1971, 5 (11), 1105-1112.

31. O'Melia, C. R. Aquasols: The Behavior of Small Particles in Aquatic Systems. *Environmental Science and Technology* 1980, 14 (9), 1052-1060.
32. Tufenkji, N.; Elimelech, M. Correlation Equation for Predicting Single-Collector Efficiency in Physicochemical Filtration in Saturated Porous Media. *Environmental Science and Technology* 2004, 38 (2), 529-536.
33. Petosa, A.; Jaisi, D. P.; Quevedo, I. R.; Elimelech, M.; Tufenkji, N. Aggregation and Deposition of Engineered Nanoparticles in Aquatic Environments: Role of Physicochemical Filtration. *Environmental Science and Technology* 2010, 44, 6532-6549.
34. Verway, E. J. W.; Overbeek, J. T. G. *Theory of the Stability of Lyophobic Colloids*; Elsevier Publishing: New York, 1948.
35. McCarthy, J. F.; Zachara, J. M. Subsurface Transport of Contaminants. *Environmental Science and Technology* 1989, 23 (5), 496-502.
36. McCarthy, J. F.; McKay, L. D. Colloid Transport in the Subsurface: Past, Present, and Future Challenges. *Vadose Zone Journal* 2004, 3, 326-337.
37. Ryan, J. N.; Elimelech, M. Review: Colloid Mobilization and Transport in Groundwater. *Colloids and Surfaces A: Physicochemical and Engineering Aspects* 1996, 107, 1-56.
38. Hahn, M. W. Aquasols: On the Role of Secondary Minima. *Environmental Science and Technology* 2004, 38 (22), 5915-5924.
39. N, T.; Redman, J. A.; Elimelech, M. Interpreting Deposition Patterns of Microbial Particles in Laboratory-Scale Column Experiments. *Environmental Science and Technology* 2003, 37 (3), 616-623.
40. Ko, C.; Elimelech, M. The "Shadow Effect" in Colloid Transport and Deposition Dynamics in Granular Porous Media: Measurements and Mechanisms. *Environmental Science and Technology* 2000, 34 (17), 3681-3689.
41. Loveland, J. P.; Bhattacharjee, S.; Ryan, J. N.; Elimelech, M. Colloid Transport in Geochemically Heterogeneous Porous Media: Aquifer Tank Experiment and Modeling. *Journal of Contaminant Hydrology* 2003, 65, 161-182.
42. Liu, D.; Johnson, P. R.; Elimelech, M. Colloid Deposition in Flow Through Porous Media: Role of Electrolyte Concentration. *Environmental Science and Technology* 1995, 29 (12), 2963-2973.

43. Nelson, K. E.; Ginn, T. R. New Collector Efficiency Equation for Colloid Filtration in Both Natural and Engineered Flow Conditions. *Water Resources Research* 2011, *47*, 1-17.
44. Elimelech, M. Effect of Particle Size on the Kinetics of Particle Deposition Under Attractive Double Layer Interactions. *Journal of Colloid and Interface Science* 1994, *164*, 190-199.
45. Elimelech, M. Kinetics of Capture of Colloidal Particles in Packed Beds Under Attractive Double Layer Interactions. *Journal of Colloid and Interface Science* 1991, *146* (2), 337-351.
46. Reerink, H.; Overbeek, J. T. G. The Rate of Coagulation as a Measure of the Stability of Silver Iodide Sols. *Discussions of the Faraday Society* 1954, *18*, 74-84.
47. Tufenkji, N.; Elimelech, M. Deviation from the Classical Colloid Filtration Theory in the Presence of Repulsive DLVO Interactions. *Langmuir* 2004, *20*, 10818-10828.
48. Pelley, A. J.; Tufenkji, N. Effect of Particle Size and Natural Organic Matter on the Migration of Nano- and Microscale Latex Particles in Saturated Porous Media. *Journal of Colloid and Interface Science* 2008, *321*, 74-83.
49. Elimelech, M.; O'Melia, C. R. Effect of Particle Size on Collision Efficiency in the Deposition of Brownian Particles with Electrostatic Energy Barriers. *Langmuir* 1990, *6*, 1153-1163.
50. Litton, G. M.; Olson, T. M. Particle Size Effects on Colloid Deposition Kinetics: Evidence of Secondary Minimum Deposition. *Colloids and Surfaces A: Physicochemical and Engineering Aspects* 1996, *107*, 273-283.
51. Bradford, S. A.; Yates, S. R.; Bettahar, M.; Simunek, J. Physical Factors Affecting the Transport and Fate of Colloids in Saturated Porous Media. *Water Resources Research* 2002, *38* (12), 63-1 - 63-12.
52. Tufenkji, N.; Elimelech, M. Breakdown of Colloid Filtration Theory: Role of the Secondary Minimum and Surface Charge Heterogeneity. *Langmuir* 2005, *21*, 841-852.
53. Hahn, M. W.; O'Melia, C. R. Deposition and Reentrainment of Brownian Particles in Porous Media under Unfavorable Chemical Conditions: Some Concepts and Applications. *Environmental Science and Technology* 2004, *38* (1), 210-220.

54. Elimelech, M.; O'Melia, C. R. Kinetics of Deposition of Colloidal Particles in Porous Media. *Environmental Science and Technology* 1990, 24, 1528-1536.
55. Tufenkji, N.; Miller, G. F.; Ryan, J. N.; Harvey, R. W.; Elimelech, M. Transport of Cryptosporidium Oocysts in Porous Media: Role of Straining and Physicochemical Filtration. *Environmental Science and Technology* 2004, 38, 5932-5938.
56. Song, L.; Johnson, P. R.; Elimelech, M. Kinetics of Colloid Deposition onto Heterogeneously Charged Surfaces in Porous Media. *Environmental Science and Technology* 1994, 28, 1164-1171.
57. Ryan, J. N.; Gschwend, P. M. Effects of Ionic Strength and Flow Rate on Colloid Release: Relating Kinetics to Intersurface Potential Energy. *Journal of Colloid and Interface Science* 1994, 164, 21-34.
58. Schroth, M. H.; Ahearn, S. J.; Selker, J. S.; Istok, J. D. Characterization of Miller-Similar Silica Sands for Laboratory Hydrologic Studies. *Soil Science Society of America Journal* 1996, 60, 1331-1339.
59. Johnson, P. R.; Sun, N.; Elimelech, M. Colloid Transport in Geochemically Heterogeneous Porous Media: Modeling and Measurements. *Environmental Science and Technology* 1996, 30, 3284-3293.
60. U.S. Environmental Protection Agency. *Nanotechnology White Paper*; Office of the Science Advisor, 2007.
61. Nowack, B.; Bucheli, T. D. Occurrence, Behavior, and Effects of Nanoparticles in the Environment. *Environmental Pollution* 2007, 150, 5-22.
62. Christian, P.; Von der Kammer, F.; Baalousha, M.; Hofmann, T. Nanoparticles: Structure, Properties, Preparation, and Behaviour in Environmental Media. *Ecotoxicology* 2008, 17, 326-343.
63. Hotze, E. M.; Phenrat, T.; Lowry, G. V. Nanoparticle Aggregation: Challenges to Understanding Transport and Reactivity in the Environment. *Journal of Environmental Quality* 2010, 39, 1909-1924.
64. Chen, K. L.; Elimelech, M. Aggregation and Deposition Kinetics of Fullerene (C60) Nanoparticles. *Langmuir* 2006, 22, 10994-11001.
65. Chowdury, I.; Hong, Y.; Walker, S. L. Container to Characterization: Impacts of Metal Oxide Handling, Preparation, and Solution Chemistry on Particle Stability. *Colloids and Surfaces A: Physicochemical and Engineering Aspects* 2010, 368, 91-95.

66. Keller, A. A.; Wang, H.; Zhou, D.; Lenihan, H. S.; Cherr, G.; Cardinale, B. J.; Miller, R.; Ji, Z. Stability and Aggregation of Metal Oxide Nanoparticles in Natural Aqueous Matrices. *Environmental Science and Technology* 2010, 44 (6), 1962-1967.
67. Shen, C.; Huang, Y.; Li, B.; Jin, Y. Predicting Attachment Efficiency of Colloid Deposition Under Unfavorable Attachment Conditions. *Water Resources Research* 2010, 46, 1-12.
68. Franchi, A.; O'Melia, C. R. Effects of Natural Organic Matter and Solution Chemistry on the Deposition and Reentrainment of Colloids in Porous Media. *Environmental Science and Technology* 2003, 37 (6), 1122-1129.
69. Baalousha, M. Aggregation and Disaggregation of Iron Oxide Nanoparticles: Influence of Particle Concentration, pH, and Natural Organic Matter. *Science of the Total Environment* 2009, 407, 2093-2101.
70. Domingos, R. F.; Tufenkji, N.; Wilkinson, K. J. Aggregation of Titanium Dioxide Nanoparticles Role of Fulvic Acid. *Environmental Science and Technology* 2009, 43 (5), 1282-1286.
71. Wiesner, M. R.; Lowry, G. V.; Alvarez, P.; Dionysiou, D.; Biswas, P. Assessing the Risks of Manufactured Nanomaterials. *Environmental Science and Technology* 2006, 40, 4336-4345.
72. Strigul, N.; Vaccari, L.; Galdun, C.; Wazne, M.; Liu, X.; Christodoulatos, C.; Jasinkiewicz, K. Acute Toxicity of Boron, Titanium Dioxide, and Aluminum Nanoparticles to *Daphnia magna* and *Vibrio fischeri*. *Desalination* 2009, 248, 771-782.
73. Chen, J.; Liu, M.; Zhang, J.; Ying, X.; Jin, L. Photocatalytic Degradation of Organic Wastes by Electrochemically Assisted TiO₂ Photocatalytic System. *Journal of Environmental Management* 2004, 70, 43-47.
74. Aitken, R. J.; Chaudhry, M. Q.; Boxall, A. B. A.; Hull, M. Manufacture and Use of Nanomaterials" Current Status in the UK and Global Trends. *Occupational Medicine* 2006, 56, 300-306.
75. Kansal, S. K.; Singh, M.; Sud, D. Effluent Quality at Kraft/Soda Agro-based Paper Mills and its Treatment Using a Heterogeneous Photocatalytic System. *Desalination* 2008, 228, 183-190.

76. Xiong, D.; Fang, T.; Yu, L.; Sima, X.; Zhu, W. Effects of Nano-Scale TiO₂, ZnO and Their Bulk Counterparts on Zebrafish: Acute Toxicity, Oxidative Stress and Oxidative Damage. *Science of the Total Environment* 2011, 409, 1444-1452.
77. Stumm, W.; Sigg, L.; Sulzberger, B. *Chemistry of the Solid-Water Interface: Processes at the Mineral-Water and Particle-Water Interface in Natural Systems*; Wiley: New York, 1992.
78. Puls, R. W.; Powell, R. M. Transport of Inorganic Colloids Through natural Aquifer Material Implications for Contaminant Transport. *Environmental Science and Technology* 1992, 26, 614-621.
79. Lecoanet, H. F.; Wiesner, M. R. Velocity Effects on Fullerene and Oxide Nanoparticle Deposition in Porous Media. *Environmental Science and Technology* 2004, 38, 4377-4382.
80. Guzman, K. A. D.; Finnegan, M. P.; Banfield, J. F. Influence of Surface Potential on Aggregation and Transport of Titania Nanoparticles. *Environmental Science and Technology* 2006, 40, 7688-7693.
81. Ben-Moshe, T.; Dror, I.; Berkowitz, B. Transport of Metal Oxide Nanoparticles in Saturated Porous Media. *Chemosphere* 2010, 81, 387-393.
82. Chowdhury, I.; Hong, Y.; Honda, R. J.; Walker, S. L. Mechanisms of TiO₂ nanoparticle Transport in Porous Media: Role of Solution Chemistry, nanoparticle Concentration, and Flowrate. *Journal of Colloid and Interface Science* 2011, 360, 548-555.
83. He, Y. T.; Wan, J. W.; Tokunaga, T. Kinetic stability of hematite nanoparticles: the effect of particle sizes. *Journal of Nanoparticle Research* 2008, 10 (2), 321-332.
84. Sposito, G. *The Surface Chemistry of Soils*; Oxford University Press: New York, 1984.
85. Sposito, G. *The Environmental Chemistry of Aluminum*, 2nd ed.; CRC Press: Berkeley, 1995.
86. Ghosh, S.; Mashayekhi, H.; Pan, B.; Bowmilk, P.; Xing, B. Colloidal Behavior of Aluminum Oxide Nanoparticles as Affected by pH and natural Organic matter. *Langmuir* 2008, 24, 12385-12391.

87. Tombacz, E.; Dobos, A.; Szekeres, M.; Narres, H. D.; Klumpp, E.; Dekany, I. Effect of pH and Ionic Strength on the Interaction of Humic Acid with Aluminum Oxide. *Colloid Polymer Science* 2000, 278, 337-345.
88. Ghosh, S.; Mashayekhi, H.; Bhowmik, P.; Xing, B. Colloidal Stability of Al₂O₃ Nanoparticles as Affected by Coating of Structurally Different Humic Acids. *Langmuir* 2009, 26 (2), 873-879.
89. Sprycha, R. Electrical Double Layer at Alumina/Electrolyte Interface 1. Surface Charge and Zeta Potential. *Journal of Colloid and Interface Science* 1989, 127 (1), 1-11.
90. Liu, D. *Chemical Aspects in the Dynamics of Particle Deposition in Porous Media*; PhD Dissertation; University of California, Los Angeles, 1994.
91. van Genuchten. *Non-equilibrium transport parameters from miscible displacement experiments*; M.Th.; USDA Salinity Laboratory: Riverside, 1971.
92. Bergstrom, L. Hamaker constants of inorganic materials. *Advances in Colloid and Interface Science* 1997, 70, 125-169.
93. Tian, Y.; Gao, B.; Silvera-Batista, C.; Ziegler, K. J. Transport of Engineered Nanoparticles in Saturated Porous Media. *Journal of Nanoparticle Research* 2010, 12, 2371-2380.

APPENDIX – EXPERIMENTAL DATA

Table 7: Non-Reactive Tracer Study Data – Study #1_pH 6_NRT

Performed for Al₂O₃ Study #1_pH 6

Column: C

Darcy Velocity: 0.098/min

Electrolyte: CaCl₂

Ionic Strength: 0.015 M

Data results for pentafluorobenzoic acid transport Study #1_pH 6_NRT; Samples 1 - 27.

Sample	Pore Volume (mL)	UV-Vis Abs	Dilution	C/C ₀	
1	-0.507	0.003	1	-0.004	LDL
2	-0.299	0.000	1	-0.005	LDL
3	-0.093	-0.002	1	-0.006	LDL
4	0.122	0.004	1	-0.004	LDL
5	0.334	0.256	1	0.032	
6	0.553	2.057	1	0.265	
7	0.772	1.571	3.0	0.612	
8	0.979	2.063	3.0	0.805	
9	1.222	2.273	3.0	0.886	
10	1.467	2.374	3.0	0.926	
11	1.695	2.395	3.0	0.935	
12	1.941	2.441	3.0	0.952	
13	2.191	2.453	3.0	0.957	
14	2.413	2.465	3.0	0.961	
15	2.708	2.506	3.0	0.978	
16	3.101	2.506	3.0	0.976	
17	3.537	2.520	3.0	0.981	
18	3.946	2.534	3.0	0.987	
19	5.356	2.550	3.0	0.994	
20	6.232	2.534	3.0	0.993	
21	7.122	2.565	3.0	1.003	
22	8.077	2.565	3.0	1.000	
23	9.006	2.565	3.0	1.000	
24	9.901	2.550	3.0	0.995	
25	10.796	2.550	3.0	0.997	
26	11.789	2.550	3.0	0.994	
27	12.761	2.550	3.0	0.997	

Table 7 (Continued): Non-Reactive Tracer Study Data – Study #1_pH 6_NRT

Data results for pentafluorobenzoic acid transport Study #1_pH 6_NRT; Samples 28 - 53.

Sample	Pore Volume (mL)	UV-Vis Abs	Dilution	C/C ₀	Elution	
28	13.099	2.550	3.0	0.993	Elution	
29	13.399	2.550	3.0	0.992		
30	13.632	2.534	3.0	0.989		
31	13.854	2.479	3.0	0.966		
32	14.102	1.845	3.0	0.718		
33	14.355	2.675	1	0.346		
34	14.606	1.217	1	0.155		
35	14.842	0.712	1	0.091		
36	15.085	0.506	1	0.064		
37	15.408	0.373	1	0.046		
38	15.811	0.271	1	0.033		
39	16.215	0.198	1	0.024		
40	16.599	0.152	1	0.018		
41	17.017	0.118	1	0.032		
42	17.483	0.097	1	0.026		
43	18.586	0.053	1	0.012		
44	19.553	0.045	1	0.009		
45	20.485	0.045	1	0.009		
46	21.356	0.032	1	0.005		
47	22.304	0.030	1	0.004		
48	23.226	0.027	1	0.003		
49	24.141	0.029	1	0.004		
50	24.988	0.025	1	0.003		
51	25.885	0.023	1	0.002		
52	26.783	0.024	1	0.002		
53	27.664	0.018	1	0.000		LDL

Table 8: Aluminum Oxide Transport Data – Study #1_pH 6

Concentration: 200 mg/L
Column: C
Darcy Velocity: 0.098 cm/min
Electrolyte: CaCl₂
Ionic Strength: 0.15 M

Data results for aluminum oxide nanoparticle transport Study #1_pH 6; samples 1 - 27.

Sample	Pore Volume (mL)	Influent pH	Effluent pH	UV-Vis	
				Abs	C/C ₀
1	-0.510			0.301	0.064
2	-0.303			0.199	0.029
3	-0.077			0.145	0.020
4	0.150			0.138	0.019
5	0.359			0.103	0.013
6	0.569			0.117	0.016
7	0.816			0.247	0.036
8	1.054			0.234	0.034
9	1.345			0.366	0.082
10	1.741			0.374	0.085
11	2.152			0.241	0.035
12	2.592			0.272	0.040
13	3.049			0.248	0.036
14	3.465			0.270	0.040
15	3.849			0.262	0.039
16	4.217			0.369	0.083
17	4.637			0.235	0.034
18	5.075			0.210	0.030
19	5.493			0.258	0.038
20	5.922			0.272	0.040
21	6.324			0.269	0.040
22	6.627			0.285	0.042
23	7.543			0.307	0.066
24	8.469			0.390	0.089
25	9.375			0.399	0.092
26	10.294			0.409	0.094
27	11.235			0.440	0.103

Table 8 (Continued): Aluminum Oxide Transport Data – Study #1_pH 6

Data results for aluminum oxide nanoparticle transport Study #1_pH 6; samples 28 - 61.

Sample	Pore Volume (mL)	Influent pH	Effluent pH	UV-Vis Abs	C/C ₀
28	12.141			0.494	0.118
29	13.023			0.510	0.122
30	13.986			0.591	0.145
31	14.918			0.631	0.156
32	15.473				
33	16.030	5.98		0.718	0.180
34	16.470	5.77	5.86		
35	16.911			0.770	0.195
36	17.365				
37	17.811			0.883	0.226
38	18.245		5.86		
39	18.695			0.956	0.247
40	19.223				
41	19.797			1.031	0.267
42	20.303		5.86		
43	20.959			1.150	0.301
44	21.676				
45	22.186			1.255	0.348
46	22.602	5.89	5.86		
47	23.033			1.382	0.385
48	23.503				
49	23.976			1.450	0.405
50	24.447		5.8		
51	24.915			1.602	0.450
52	25.475				
53	26.027			1.800	0.508
54	26.471		5.79		
55	26.958			1.781	0.502
56	27.473				
57	27.951			2.114	0.600
58	28.426		5.8		
59	28.913			2.189	0.622
60	29.371				
61	29.815			1.999	0.566

Table 8 (Continued): Aluminum Oxide Transport Data – Study #1_pH 6

Data results for aluminum oxide nanoparticle transport Study #1_pH 6; samples 62 - 93.

Sample	Pore Volume (mL)	Influent pH	Effluent pH	UV-Vis Abs	C/C _o
62	30.338		5.76		
63	30.893			2.361	0.673
64	31.380				
65	31.871			2.203	0.626
66	32.416		5.83		
67	32.934			2.415	0.688
68	33.458				
69	34.047			2.314	0.659
70	34.612		5.96		
71	35.173			2.393	0.682
72	35.723				
73	36.183			2.323	0.661
74	36.636		5.82		
75	37.051			2.305	0.656
76	37.537				
77	37.999			2.916	0.836
78	38.472				
79	38.957	5.93		2.633	0.752
80	39.244			0.173	0.046
81	39.450			0.133	0.034
82	39.647			0.122	0.031
83	39.834			0.141	0.036
84	40.029			0.337	0.097
85	40.239			1.023	0.315
86	40.456			1.759	0.548
87	40.679			2.141	0.669
88	40.913		6.23	2.293	0.717
89	41.128			2.415	0.755
90	41.356			2.390	0.748
91	41.586			2.369	0.741
92	41.806			2.369	0.741
93	42.019			2.369	0.741

7 day Stop Flow

Table 8 (Continued): Aluminum Oxide Transport Data – Study #1_pH 6

Data results for aluminum oxide nanoparticle transport Study #1_pH 6; samples 94 - 127.

Sample	Pore Volume (mL)	Influent pH	Effluent pH	UV-Vis Abs	C/C ₀
94	42.240			2.390	0.747
95	42.488			2.412	0.754
96	42.730			2.412	0.754
97	42.940		6.02	2.448	0.766
98	43.142			2.448	0.766
99	43.379			2.448	0.766
100	43.612	5.95		2.474	0.774
101	43.855			2.474	0.774
102	44.138		5.91	2.501	0.783
103	44.617		6.76		
104	45.039			2.529	0.791
105	45.477		6.04		
106	45.929			2.529	0.791
107	46.387		5.95		
108	46.832	6.12		2.560	0.801
109	47.289		5.96		
110	47.750			2.515	0.787
111	48.155		5.84		
112	48.597			2.560	0.801
113	49.059		5.88		
114	49.504			2.560	0.801
115	49.947		5.84		
116	50.390			2.560	0.801
117	50.813	5.86	5.84		
118	51.241			2.560	0.801
119	51.734		5.81		
120	52.358			2.529	0.791
121	52.983	5.91	5.84		
122	53.489			2.560	0.801
123	53.973		5.86		
124	54.620			2.560	0.801
125	55.221		5.87		
126	55.642			2.560	0.801
127	56.102		5.87		

Table 8 (Continued): Aluminum Oxide Transport Data – Study #1_pH 6

Data results for aluminum oxide nanoparticle transport Study #1_pH 6; samples 128-161.

Sample	Pore Volume (mL)	Influent pH	Effluent pH	UV-Vis Abs	C/C _o	
128	56.608			2.560	0.801	
129	57.153	5.85	5.84			
130	57.630			2.612	0.818	
131	58.063		5.82			
132	58.518			2.560	0.801	
133	58.992		5.86			
134	59.480			2.577	0.807	
135	60.081		5.88			
136	60.656	5.84		2.577	0.807	
137	60.935			2.401	0.751	Elution
138	61.154			2.460	0.770	
139	61.355			2.501	0.783	
140	61.570			2.501	0.783	
141	61.839			2.179	0.681	
142	62.078		5.95	1.336	0.414	
143	62.269			0.687	0.208	
144	62.489			0.298	0.085	
145	62.721		5.9	0.131	0.034	
146	63.101			0.072	0.017	
147	63.475	6.09		0.035	0.006	
148	63.773			0.017	0.001	
149	64.127			0.011	-0.001	LDL
150	64.496		5.91	0.010	-0.001	LDL
151	64.894			0.017	0.001	
152	65.224			0.013	0.000	LDL
153	65.663		5.88			
154	66.090			0.004	-0.003	LDL
155	66.560	6.08	5.83			
156	67.248		5.86	0.008	-0.002	LDL
157	67.869		5.84			
158	68.262			-0.005	-0.006	LDL
159	68.365		5.84			
160	68.715			-0.002	-0.005	LDL
161	68.883	6.07		-0.001	-0.004	LDL

Table 9: Non-Reactive Tracer Study Data – Study #2_pH 6_NRT

Performed for Al₂O₃ Study #2_pH 6

Column: C

Darcy Velocity: 0.092 cm/min

Electrolyte: CaCl₂

Ionic Strength: 0.015 M

Data results for pentafluorobenzoic acid transport Study #2_pH 6_NRT; Samples 1 - 28.

Sample	Pore Volume (mL)	UV-Vis Abs	Dilution	C/C ₀	
1	-0.795	0.030	1	0.002	
2	-0.607	0.013	1	-0.001	LDL
3	-0.438	0.011	1	-0.001	LDL
4	-0.270	0.011	1	-0.001	LDL
5	-0.063	0.010	1	-0.001	LDL
6	0.183	0.114	1	0.013	
7	0.429	1.496	1	0.199	
8	0.644	1.563	2.9	0.598	
9	0.927	2.115	3.1	0.870	
10	1.299	2.202	3.2	0.930	
11	1.616	2.510	2.9	0.964	
12	1.928	2.311	3.1	0.967	
13	2.281	2.421	3.0	0.960	
14	2.651	2.269	3.2	0.975	
15	3.057	2.057	3.6	0.981	
16	3.366	2.082	3.5	0.975	
17	4.535	2.510	2.9	0.985	
18	5.507	2.175	3.4	0.980	
19	6.323	2.586	2.9	0.987	
20	7.120	2.294	3.2	0.981	
21	8.053	2.277	3.2	0.980	
22	8.673	2.554	2.8	0.957	
23	8.894	2.445	3.0	0.982	
24	9.118	2.399	3.1	0.982	
25	9.360	2.679	2.7	0.978	
26	9.596	2.445	3.0	0.989	
27	9.833	2.510	2.9	0.984	
28	10.087	2.679	2.7	0.972	

Table 9 (Continued): Non-Reactive Tracer Study Data – Study #2_pH 6_NRT

Data results for pentafluorobenzoic acid transport Study #2_pH 6_NRT; Samples 29 - 57.

Sample	Pore Volume (mL)	UV-Vis Abs	Dilution	C/C _o	
29	10.428	2.722	2.7	0.984	
30	10.879	2.399	2.8	0.910	
31	11.843	2.410	3.1	0.990	
32	12.197	2.509	2.9	0.986	Elution
33	12.402	2.509	3.0	0.997	
34	12.666	2.585	2.9	0.990	
35	12.923	2.252	3.3	1.001	
36	13.127	2.585	2.8	0.984	
37	13.351	2.482	2.6	0.869	
38	13.598	1.120	2.9	0.441	
39	13.806	0.414	3.0	0.164	
40	14.123	0.537	1	0.071	
41	14.545	0.325	1	0.043	
42	15.026	0.257	1	0.033	
43	15.529	0.220	1	0.028	
44	15.965	0.203	1	0.025	
45	16.404	0.192	1	0.024	
46	16.743	0.178	1	0.022	
47	17.624	0.147	1	0.018	
48	18.575	0.121	1	0.014	
49	19.465	0.096	1	0.011	
50	20.446	0.080	1	0.009	
51	21.404	0.068	1	0.007	
52	22.336	0.072	1	0.008	
53	23.318	0.053	1	0.005	
54	24.235	0.049	1	0.004	
55	25.151	0.051	1	0.005	
56	26.020	0.047	1	0.004	
57	27.114	0.032	1	0.002	

Table 10: Aluminum Oxide Transport Data – Study #2_pH 6

Concentration: 25 mg/L

Column: C

Darcy Velocity: 0.096 cm/min

Electrolyte: CaCl₂

Ionic Strength: 0.015 M

Data results for aluminum oxide nanoparticle transport Study #2_pH 6; samples 1 - 27.

Sample	Pore Volume (mL)	Influent pH	Effluent pH	UV-Vis Abs	C/C _o	
1	-0.818			0.001		LDL
2	-0.563			0.001		LDL
3	-0.284			0.018		LDL
4	-0.036			0.001		LDL
5	0.235			0.001		LDL
6	0.542		5.95	0.004		LDL
7	0.882	6.07		0.006		LDL
8	1.185			0.011		LDL
9	1.420			0.001		LDL
10	1.688			0.004		LDL
11	2.008		5.75	0.000		LDL
12	2.424			0.001		LDL
13	2.959			0.011		LDL
14	3.415		5.82	-0.002		LDL
15	3.741			0.018		LDL
16	4.231		5.84			
17	4.663			0.014		LDL
18	5.091	5.98	5.89			
19	5.524			0.015		LDL
20	5.960		5.88			
21	6.386			0.020		LDL
22	6.827		5.88			
23	7.276			0.016		LDL
24	7.688		5.85			
25	8.101			0.015		LDL
26	8.861		5.94			
27	9.663			0.014		LDL

Table 10 (Continued): Aluminum Oxide Transport Data – Study #2_pH 6

Data results for aluminum oxide nanoparticle transport Study #2_pH 6; samples 28 - 60.

Sample	Pore Volume (mL)	Influent pH	Effluent pH	UV-Vis Abs	C/C _o	
28	10.420	5.96	5.92			
29	11.187			0.015		LDL
30	12.017		5.98			
31	12.825			0.019		LDL
32	13.585		5.95			
33	14.344			0.022		LDL
34	15.177	5.95	5.99			
35	15.988			0.022		LDL
36	16.753		5.98			
37	17.533			0.013		LDL
38	18.333		5.96			
39	19.146			0.023		LDL
40	19.910	5.94	5.96			
41	20.653			0.013		LDL
42	21.406		5.98			
43	22.201			0.013		LDL
44	23.010		5.98			
45	23.797			0.021		LDL
46	24.649		5.95			
47	25.489			0.013		LDL
48	26.270		5.98			
49	27.058			0.082	0.103	
50	27.245					
51	27.416			0.027		LDL
52	27.618			0.020		LDL
53	27.826			0.019		LDL
54	28.069			0.046	0.066	Stop Flow
55	28.268			0.019		LDL
56	28.468			0.009		LDL
57	28.697			0.008		LDL
58	28.966			0.017		LDL
59	29.202			0.146	0.327	
60	29.417			0.027		LDL

Table 10 (Continued): Aluminum Oxide Transport Data – Study #2_pH 6

Data results for aluminum oxide nanoparticle transport Study #2_pH 6; samples 61 - 93.

Sample	Pore Volume (mL)	Influent pH	Effluent pH	UV-Vis Abs	C/C _o	
61	29.673		5.91	0.031		LDL
62	30.015			0.019		LDL
63	30.460			0.018		LDL
64	30.930		5.84	0.025		LDL
65	31.275			0.020		LDL
66	31.700	5.91	5.72			
67	32.105			0.013		LDL
68	32.561		5.73			
69	33.090			0.016		LDL
70	33.586		5.76			
71	34.009			0.009		LDL
72	34.484		5.75			
73	34.985			0.032	0.038	
74	35.469		5.76			
75	35.924			0.026		LDL
76	36.341		5.77			
77	36.776			0.057	0.087	
78	37.224		5.73			
79	37.673			0.016		LDL
80	38.192	5.86	5.75			
81	38.716	5.95		0.051	0.075	
82	39.489		5.83			
83	40.234			0.023		LDL
84	40.958		5.85			
85	41.692			0.051	0.075	
86	42.454		5.86			
87	43.214			0.007		LDL
88	44.111		5.88			
89	44.995			0.014		LDL
90	45.741		5.93			
91	46.496			0.014		LDL
92	47.239	5.95	5.95			
93	48.003			0.091	0.092	

Table 10 (Continued): Aluminum Oxide Transport Data – Study #2_pH 6

Data results for aluminum oxide nanoparticle transport Study #2_pH 6; samples 94 - 126.

Sample	Pore Volume (mL)	Influent pH	Effluent pH	UV-Vis Abs	C/C _o	
94	48.393			0.012		LDL
95	49.139		5.96			
96	49.886			0.014		LDL
97	50.638		5.94			
98	51.382			0.011		LDL
99	52.108	5.89	5.89			
100	52.866			0.014		LDL
101	53.620		5.93			
102	54.340			0.011		LDL
103	55.166		5.95			
104	56.002	5.88		0.026		LDL
105	57.054	6.10	5.98			
106	58.130			0.015		LDL
107	59.084		5.98			
108	60.044			0.013		LDL
109	60.907	6.07	5.97			
110	61.743			0.015		LDL
111	62.510		6.03			
112	63.287			0.014		LDL
113	64.056		6.06			
114	64.835			0.018		LDL
115	65.635	5.98	6.01			
116	66.432			0.016		LDL
117	66.704			0.028		Stop Flow,LDL
118	66.907			0.013		LDL
119	67.135			0.008		LDL
120	67.384			0.004		LDL
121	67.624			0.007		LDL
122	67.851			0.013		LDL
123	68.162		6.08	0.015		LDL
124	68.553			0.009		LDL
125	68.926			0.012		LDL
126	69.341		5.89	0.010		LDL

Table 10 (Continued): Aluminum Oxide Transport Data – Study #2_pH 6

Data results for aluminum oxide nanoparticle transport Study #2_pH 6; samples 127-159.

Sample	Pore Volume (mL)	Influent pH	Effluent pH	UV-Vis Abs	C/C _o	
127	69.774			0.009		LDL
128	70.195		5.80	0.012		LDL
129	71.178	6.09	5.94			
130	72.096			0.014		LDL
131	73.037		6.02			
132	73.941			0.013		LDL
133	74.867	6.08	5.99			
134	75.849			0.060	0.061	
135	76.083					
136	76.258			0.014		LDL
137	77.173		6.08			
138	78.127			0.015		LDL
139	79.109		5.92			
140	80.032			0.118	0.236	
141	80.166					
142	80.299			0.022		LDL
143	81.182	6.08	6.04			
144	82.074			0.023		LDL
145	82.998		6.05			
146	83.921			0.012		LDL
147	84.863		6.02			
148	85.871			0.018		LDL
149	86.798	6.04	6.02			
150	89.552			0.018		LDL
151	88.557		6.04			
152	89.387			0.011		LDL
153	90.290		6.00			
154	91.181			0.018		LDL
155	92.080		5.99			
156	92.985			0.020		LDL
157	93.899		6.09			
158	94.818			0.023		LDL
159	95.756		6.00			

Table 10 (Continued): Aluminum Oxide Transport Data – Study #2_pH 6

Data results for aluminum oxide nanoparticle transport Study #2_pH 6; samples 160-192.

Sample	Pore Volume (mL)	Influent pH	Effluent pH	UV-Vis Abs	C/C _o	
160	96.730			0.021		LDL
161	97.730		6.05			
162	98.701			0.021		LDL
163	99.607		6.08			
164	100.515			0.025		LDL
165	101.424		6.09			
166	102.336			0.028		LDL
167	103.083		6.13			
168	103.808			0.174	0.371	
169	104.073			0.068	0.070	Stop Flow
170	104.279			0.052	0.033	
171	104.477			0.044	0.014	
172	104.674			0.533	1.348	
173	104.882			0.028		LDL
174	105.083		6.14	0.045		LDL
175	105.277			0.053	0.035	
176	105.478			0.071	0.077	
177	105.682			0.068	0.070	
178	105.896			0.118	0.208	
179	106.162			0.075	0.086	
180	106.415			0.067	0.068	
181	106.616		5.84	0.051	0.030	
182	106.823			0.073	0.082	
183	107.125			0.078	0.093	
184	107.570			0.049		LDL
185	108.050	5.88		0.054	0.037	
186	108.472	6.03	5.72	0.053	0.035	
187	108.894			0.046		LDL
188	109.311			0.063	0.058	
189	109.694		5.66	0.094	0.140	
190	110.248		5.87			
191	110.730			0.051	0.030	
192	111.176		5.84			

Table 10 (Continued): Aluminum Oxide Transport Data – Study #2_pH 6

Data results for aluminum oxide nanoparticle transport Study #2_pH 6; samples 193-225.

Sample	Pore Volume (mL)	Influent pH	Effluent pH	UV-Vis Abs	C/C ₀	
193	111.595			0.074	0.084	
194	112.008	6.02	5.83			
195	112.416			0.046		LDL
196	112.830		5.83			
197	113.250			0.045		LDL
198	113.988		5.87			
199	114.729			0.053	0.035	
200	115.706		5.90			
201	116.711			0.089	0.126	
202	117.065		5.95			
203	118.653			0.030		LDL
204	121.294		6.00			
205	123.922			0.092	0.134	
206	126.636		5.95			
207	129.379			0.044		LDL
208	130.313	5.95	5.91			
209	131.272			0.068	0.070	
210	132.160		5.91			
211	133.052			0.071	0.077	
212	134.307		5.90			
213	134.918			0.051	0.030	
214	135.801		5.86			
215	136.646	5.96		0.039		LDL
216	137.459		5.87			
217	138.307			0.054	0.037	
218	139.143		5.89			
219	139.956			0.043		LDL
220	140.403	5.93	5.80			
221	140.841			0.049		LDL
222	141.101			0.062	0.109	
223	141.313			0.035	0.042	Stop Flow
224	141.571			0.039	0.053	
225	141.888			0.040	0.056	

Table 10 (Continued): Aluminum Oxide Transport Data – Study #2_pH 6

Data results for aluminum oxide nanoparticle transport Study #2_pH 6; samples 226-258.

Sample	Pore Volume (mL)	Influent pH	Effluent pH	UV-Vis Abs	C/C _o	LDL
226	142.225			0.030		LDL
227	142.544		5.98	0.058	0.108	
228	142.872			0.048	0.079	
229	143.192			0.050	0.085	
230	144.467		5.84			
231	145.719			0.040	0.056	
232	146.616	5.88	5.80			
233	147.503	6.11		0.031		LDL
234	148.453		5.82			
235	149.452			0.060	0.113	
236	150.416		5.78			
237	151.370			0.052	0.090	
238	152.267		5.83			
239	153.111	6.09		0.177	0.403	
240	153.240					
241	153.390			0.043	0.065	
242	154.297		5.91			
243	155.225			0.118	0.251	
244	155.402					
245	155.539			0.105	0.218	
246	155.677					
247	155.860			0.066	0.119	
248	156.312		5.86			
249	156.730			0.096	0.195	
250	157.137	6.07	5.93			
251	157.538					
252	157.972		5.90			
253	158.412			0.067	0.122	
254	158.981		5.90			
255	159.548			0.045	0.070	
256	160.454		5.88			
257	161.352			0.072	0.134	
258	162.709	6.04	5.98			

Table 10 (Continued): Aluminum Oxide Transport Data – Study #2_pH 6

Data results for aluminum oxide nanoparticle transport Study #2_pH 6; samples 259-291.

Sample	Pore Volume (mL)	Influent pH	Effluent pH	UV-Vis Abs	C/C _o	
259	164.056			0.042	0.062	
260	165.021		5.93			
261	166.029			0.059	0.110	
262	167.071	6.01	5.95			
263	168.098			0.073	0.137	
264	168.930		5.94			
265	169.741			0.050	0.085	
266	170.807		5.98			
267	171.927			0.045	0.070	
268	172.637		5.93			
269	173.292	5.97		0.085	0.167	
270	173.590			0.033	0.048	Stop Flow
271	173.848			0.068	0.114	
272	174.095			0.024	0.033	
273	174.354			0.027	0.038	
274	174.641			0.052	0.083	
275	174.896			0.068	0.114	
276	175.150		5.94	0.044	0.067	
277	176.065		5.94			
278	176.953			0.052	0.083	
279	177.921		5.89			
280	178.898			0.063	0.104	
281	179.794	5.95	5.89			
282	180.688			0.045	0.069	
283	181.644		5.88			
284	182.562			0.106	0.187	
285	182.979		5.81			
286	183.401			0.050	0.079	
287	186.453		5.96			
288	189.504			0.120	0.214	
289	189.928		5.86			
290	190.348	5.93		0.054	0.086	
291	191.279		5.85			

Table 10 (Continued): Aluminum Oxide Transport Data – Study #2_pH 6

Data results for aluminum oxide nanoparticle transport Study #2_pH 6; samples 292-324.

Sample	Pore Volume (mL)	Influent pH	Effluent pH	UV-Vis Abs	C/C _o
292	192.270			0.046	0.071
293	193.261		5.81		
294	194.208			0.056	0.090
295	195.183	5.93	5.86		
296	196.215			0.059	0.096
297	197.113		5.81		
298	198.005			0.072	0.121
299	199.012		5.89		
300	199.978			0.062	0.102
301	201.060	5.88	5.84		
302	202.132			0.067	0.112
303	203.112	5.94	5.84		
304	204.116			0.081	0.139
305	205.004		5.88		
306	205.921			0.080	0.137
307	206.284			0.045	0.085
308	206.499			0.039	0.071
309	206.764			0.085	0.180
310	207.074			0.020	0.023
311	207.328		5.88	0.043	0.081
312	207.550			0.049	0.095
313	207.759			0.075	0.157
314	207.969			0.090	0.192
315	208.253		6.07	0.056	0.112
316	209.178		5.92		
317	210.034			0.070	0.145
318	210.936	5.98	5.87		
319	211.859			0.078	0.164
320	212.797		5.86		
321	213.707			0.063	0.128
322	214.547	5.95	5.86		
323	215.418			0.103	0.223
324	216.555		5.86		

Stop Flow

Table 10 (Continued): Aluminum Oxide Transport Data – Study #2_pH 6

Data results for aluminum oxide nanoparticle transport Study #2_pH 6; samples 325-357.

Sample	Pore Volume (mL)	Influent pH	Effluent pH	UV-Vis Abs	C/C ₀	
325	217.714			0.077	0.161	
326	218.568	5.95	5.89			
327	219.368			0.140	0.311	
328	219.514					
329	219.656			0.084	0.178	
330	219.788					
331	219.926			0.092	0.197	
332	222.734		5.92			
333	225.599			0.062	0.126	
334	226.639		5.93			
335	227.635			0.080	0.169	
336	228.550		5.89			
337	229.456			0.078	0.164	
338	230.313		5.88			
339	231.178			0.082	0.173	
340	232.326	5.87	5.90			
341	233.564	5.92		0.082	0.173	
342	232.671		5.90			
343	235.447			0.116	0.251	
344	236.442		5.96			
345	237.508			0.106	0.230	
346	238.071		5.93			
347	238.587			0.086	0.183	
348	238.961			0.041		LDL, Stop Flow
349	239.277			0.041		LDL
350	239.529			0.023		LDL
351	239.818			0.053	0.091	
352	240.079			0.068	0.127	
353	240.266			0.138	0.305	
354	240.488		6.05	0.083	0.164	
355	240.714			0.068	0.127	
356	240.907			0.118	0.254	
357	241.160			0.126	0.274	

Table 10 (Continued): Aluminum Oxide Transport Data – Study #2_pH 6

Data results for aluminum oxide nanoparticle transport Study #2_pH 6; samples 358-390.

Sample	Pore Volume (mL)	Influent pH	Effluent pH	UV-Vis Abs	C/C ₀
358	241.409			0.082	0.162
359	241.745			0.102	0.211
360	242.093			0.091	0.184
361	242.427		5.85	0.147	0.327
362	243.313		5.95		
363	244.195	5.95		0.086	0.171
364	245.016		5.93		
365	245.803			0.174	0.396
366	246.328		5.89		
367	246.816			0.225	0.525
368	246.948				
369	247.090			0.101	0.208
370	247.908			0.090	0.181
371	248.637		5.93		
372	249.431			0.118	0.254
373	250.148	5.92	5.93		
374	250.867	5.94		0.429	1.043
375	250.974				
376	251.143			0.455	1.109
377	251.271				
378	251.409			0.096	0.196
379	251.693			0.089	0.179
380	251.987			0.097	0.198
381	252.968		5.95		
382	253.988			0.092	0.186
383	254.784		5.98		
384	255.631	5.93		0.091	0.184
385	256.523		5.90		
386	257.375			0.089	0.179
387	258.309		5.84		
388	259.251			0.115	0.246
389	260.164		5.92		
390	261.053	5.89		0.097	0.198

Table 10 (Continued): Aluminum Oxide Transport Data – Study #2_pH 6

Data results for aluminum oxide nanoparticle transport Study #2_pH 6; samples 391-423.

Sample	Pore Volume (mL)	Influent pH	Effluent pH	UV-Vis Abs	C/C _o	
391	261.941	5.99	5.88			
392	262.820			0.093	0.189	
393	263.895		5.90			
394	265.104			0.097	0.198	
395	266.106		5.92			
396	267.044			0.097	0.198	
397	268.109	5.96	5.99			
398	269.162			0.098	0.201	
399	270.529		6.01			
400	271.808			0.113	0.241	
401	271.982					
402	272.148			0.106	0.220	
403	272.395			0.107		LDL, Stop Flow
404	272.606			0.086		LDL
405	272.811			0.057		LDL
406	273.019			0.047		LDL
407	273.255			0.037		LDL
408	273.503		6.15	0.092		LDL
409	273.742			0.126	0.092	
410	273.996			0.127	0.096	
411	274.267	5.98		0.127	0.096	
412	274.516			0.122		LDL
413	274.826		6.14	0.137	0.134	
414	275.226			0.126	0.092	
415	275.606			0.134	0.122	
416	276.429		5.41			
417	277.207			0.137	0.134	
418	278.213	5.98	5.71			
419	279.223			0.135	0.126	
420	281.619		5.88			
421	284.013			0.143	0.156	
422	286.481		5.91			
423	288.975			0.150	0.183	

Table 10 (Continued): Aluminum Oxide Transport Data – Study #2_pH 6

Data results for aluminum oxide nanoparticle transport Study #2_pH 6; samples 424-456.

Sample	Pore Volume (mL)	Influent pH	Effluent pH	UV-Vis Abs	C/C _o	
424	290.864		5.95			
425	292.745			0.192	0.315	
426	293.772	5.96	5.93			
427	294.801			0.205	0.348	
428	295.801					
429	296.841			0.202	0.340	
430	298.449		5.96			
431	300.025			0.206	0.350	
432	300.962		5.96			
433	302.015	5.95		0.206	0.350	
434	303.306		5.96			
435	304.488			0.209	0.358	
436	305.581		5.96			
437	306.734			0.218	0.380	
438	307.786		5.95			
439	308.778			0.212	0.365	
440	309.892		5.64			
441	311.007			0.218	0.380	
442	313.175					
443	315.389			0.227	0.403	
444	317.231	6.01		0.207	0.353	Stop Flow
445	317.579			0.236	0.425	
446	317.925			0.226	0.400	
447	318.279			0.231	0.413	
448	318.661			0.226	0.400	
449	318.990			0.216	0.440	
450	319.487			0.210	0.423	
451	319.924			0.216	0.440	
452	320.744		4.79			
453	321.507			0.220	0.452	
454	322.516	6.00	5.99			
455	323.285			0.203	0.402	
456	324.448		5.60			

Table 10 (Continued): Aluminum Oxide Transport Data – Study #2_pH 6

Data results for aluminum oxide nanoparticle transport Study #2_pH 6; samples 457-488.

Sample	Pore Volume (mL)	Influent pH	Effluent pH	UV-Vis Abs	C/C ₀	
457	325.590			0.216	0.440	
458	326.677		5.77			
459	327.788			0.218	0.446	
460	328.464		5.95			
461	329.181			0.217	0.443	
462	344.543		5.07			
462	345.613			0.208	0.417	
463	346.691			0.244	0.523	
464	347.485	5.98	4.95			
465	348.194			0.251	0.543	
466	350.382		5.27			
467	352.642			0.244	0.523	
468	356.654		5.84			
469	360.638			0.236	0.499	
470	362.467		5.77			
471	364.266	5.98		0.266	0.588	
472	365.829		5.91			
473	367.391			0.272	0.605	
474	368.555		5.66			
475	369.706			0.267	0.590	
476	369.956			0.079		LDL, Stop Flow
477	370.161			0.066		LDL
478	370.358			0.030		LDL
479	370.560			0.038		LDL
480	370.765			0.044		LDL
481	370.968			0.065		LDL
482	371.205		5.96	0.138	0.213	
483	371.449			0.218	0.276	
484	371.674			0.262	0.432	
485	371.906			0.256	0.411	
486	372.132			0.262	0.432	
487	372.354			0.253	0.400	
488	372.572			0.264	0.440	

Table 10 (Continued): Aluminum Oxide Transport Data – Study #2_pH 6

Data results for aluminum oxide nanoparticle transport Study #2_pH 6; samples 489-521.

Sample	Pore Volume (mL)	Influent pH	Effluent pH	UV-Vis Abs	C/C ₀
489	372.793			0.256	0.411
490	373.123		5.39	0.265	0.443
491	375.635		5.85		
492	378.041			0.304	0.582
493	378.678			0.283	0.507
494	378.870			0.292	0.539
495	379.068			0.298	0.560
496	379.274			0.289	0.528
497	379.490		6.03	0.299	0.564
498	379.905	6.04	6.02		
499	380.320			0.299	0.564
500	380.743		5.98		
501	381.169			0.291	0.536
502	382.018		5.91		
503	382.910			0.284	0.511
504	383.737		5.98		
505	384.530			0.291	0.536
506	385.285		6.04		
507	386.103			0.287	0.521
508	387.205		6.04		
509	388.287			0.292	0.539
510	389.283	6.03	5.94		
511	390.247			0.298	0.560
512	391.276		6.02		
513	392.341			0.289	0.528
514	393.075		6.02		
515	394.054			0.056	0.084
516	394.259			0.059	0.091
517	394.462			0.076	0.134
518	394.670			0.163	0.355
519	394.873			0.101	0.197
520	395.071			0.121	0.248
521	395.278			0.152	0.327

Stop Flow

Table 10 (Continued): Aluminum Oxide Transport Data – Study #2_pH 6

Data results for aluminum oxide nanoparticle transport Study #2_pH 6; samples 522-554.

Sample	Pore Volume (mL)	Influent pH	Effluent pH	UV-Vis	
				Abs	C/C ₀
522	395.517			0.232	0.539
523	395.781		6.10	0.271	0.639
524	396.030			0.274	0.647
525	396.256			0.280	0.662
526	396.540			0.305	0.727
527	396.913			0.316	0.755
528	397.277	5.98	5.96	0.303	0.721
529	397.642	5.98	5.91	0.315	0.752
530	398.028			0.305	0.727
531	398.480			0.304	0.724
532	400.101			0.309	0.737
533	403.938			0.318	0.760
534	405.358		5.81		
535	406.745			0.317	0.757
536	408.501		5.95		
537	410.252			0.316	0.755
538	411.796		5.95		
539	413.347			0.324	0.775
540	415.315		5.95		
541	417.322			0.322	0.770
542	419.382		5.96		
543	421.389			0.322	0.770
544	423.428	5.96	5.96		
545	425.478			0.314	0.750
546	427.562			0.313	0.747
547	427.819			0.064	0.086
548	428.098			0.108	0.188
549	428.392			0.137	0.255
550	428.596			0.123	0.223
551	428.809			0.147	0.290
552	429.019			0.182	0.384
553	429.258		6.03	0.241	0.543
554	429.532			0.282	0.654

Stop Flow

Table 10 (Continued): Aluminum Oxide Transport Data – Study #2_pH 6

Data results for aluminum oxide nanoparticle transport Study #2_pH 6; samples 555-587.

Sample	Pore Volume (mL)	Influent pH	Effluent pH	UV-Vis Abs	C/C ₀
555	429.770			0.296	0.691
556	430.026			0.303	0.710
557	430.324			0.305	0.716
558	430.587			0.308	0.724
559	430.834		5.96	0.315	0.742
560	431.185			0.311	0.732
561	431.669			0.310	0.729
562	432.163			0.318	0.751
563	437.452			0.321	0.759
564	440.436	6.02	5.98		
565	443.455			0.324	0.767
566	446.132		5.89		
567	448.773			0.330	0.783
568	450.645		5.93		
569	452.501			0.335	0.796
570	453.887	5.98	5.90		
571	455.340			0.315	0.742
572	456.042			0.322	0.761
573	456.400			0.085	0.164
574	456.645			0.076	0.142
575	456.908			0.061	0.105
576	457.177			0.077	0.145
577	457.440			0.129	0.259
578	457.720			0.212	0.470
579	458.053		6.01	0.293	0.677
580	458.377			0.313	0.728
581	458.657			0.323	0.753
582	458.922			0.333	0.778
583	459.199			0.332	0.776
584	459.541			0.334	0.781
585	459.949			0.332	0.776
586	461.129		5.92		
587	462.217			0.336	0.786

Stop Flow

Table 10 (Continued): Aluminum Oxide Transport Data – Study #2_pH 6

Data results for aluminum oxide nanoparticle transport Study #2_pH 6; samples 588-620.

Sample	Pore Volume (mL)	Influent pH	Effluent pH	UV-Vis Abs	C/C ₀	
588	463.926		5.90			
589	466.013			0.332	0.776	
590	468.034		5.99			
591	470.082	6.00		0.336	0.786	
592	472.114		5.97			
593	474.104			0.346	0.812	
594	476.253		5.89			
595	478.407			0.344	0.807	
596	480.409	6.00	6.02			
597	482.401			0.341	0.799	
598	483.029		6.01			
599	483.653			0.343	0.804	
600	483.901			0.115	0.109	Stop Flow
601	484.110			0.135	0.138	
602	484.328			0.096	0.081	
603	484.539			0.102	0.090	
604	484.736			0.114	0.107	
605	484.941			0.143	0.149	
606	485.202			0.248	0.458	
607	485.486		6.05	0.323	0.678	
608	485.714			0.365	0.801	
609	485.909			0.347	0.748	
610	486.116			0.366	0.804	
611	486.336			0.341	0.731	
612	486.557			0.343	0.737	
613	486.761		5.86	0.456	1.067	
614	487.033			0.385	0.859	
615	487.357			0.380	0.845	
616	487.570			0.347	0.748	
617	487.811			0.364	0.798	
618	488.053			0.370	0.816	
619	488.339		5.85	0.395	0.889	
620	488.646			0.359	0.783	

Table 10 (Continued): Aluminum Oxide Transport Data – Study #2_pH 6

Data results for aluminum oxide nanoparticle transport Study #2_pH 6; samples 621-653.

Sample	Pore Volume (mL)	Influent pH	Effluent pH	UV-Vis Abs	C/C _o	
621	488.903			0.392	0.880	
622	489.221			0.378	0.839	
623	489.622		5.85	0.375	0.830	
624	490.049			0.410	0.933	
625	490.624			0.383	0.854	
626	491.087		4.91	0.363	0.795	
627	493.361		5.89			
628	495.644			0.368	0.810	
629	497.172		6.01	0.378	0.839	
630	498.741			0.366	0.804	
631	501.964		5.98			
632	505.175			0.359	0.783	
633	507.119		6.00			
634	509.061	5.95	5.95	0.370	0.816	
635	513.286			0.356	0.775	
636	513.505			0.355	0.772	
637	513.815			0.135	0.232	Stop Flow
638	514.071			0.248	0.544	
639	514.304			0.197	0.410	
640	514.525			0.225	0.484	
641	514.737			0.240	0.523	
642	514.946			0.306	0.697	
643	515.150		5.99	0.301	0.684	
644	515.418			0.491	1.183	
645	515.709			0.390	0.917	
646	515.929			0.388	0.912	
647	516.133			0.384	0.902	
648	516.394			0.413	0.978	
649	516.736			0.407	0.962	
650	517.097		5.96	0.390	0.917	
651	517.469			0.413	0.978	
652	517.846			0.374	0.875	
653	518.247			0.372	0.870	

Table 10 (Continued): Aluminum Oxide Transport Data – Study #2_pH 6

Data results for aluminum oxide nanoparticle transport Study #2_pH 6; samples 654-686.

Sample	Pore Volume (mL)	Influent pH	Effluent pH	UV-Vis Abs	C/C ₀
654	518.760		5.83	0.427	1.015
655	519.234			0.376	0.881
656	519.623			0.390	0.917
657	520.084		5.83	0.383	0.899
658	520.638			0.373	0.873
659	521.125			0.383	0.899
660	521.515		5.79	0.379	0.889
661	522.651		5.79		
662	523.698			0.381	0.894
663	525.764		5.92		
664	527.830			0.373	0.873
665	529.814	5.97	5.91		
666	531.848			0.368	0.860
667	533.886		5.89		
668	535.893			0.370	0.865
669	537.962	5.96	5.91		
670	540.012			0.364	0.849
671	540.585		5.93		
672	541.159			0.374	0.875
673	541.414			0.118	0.192
674	541.607			0.233	0.516
675	541.820			0.216	0.471
676	542.045			0.221	0.484
677	542.258			0.227	0.500
678	542.454			0.256	0.578
679	542.651			0.272	0.621
680	542.853		5.91	0.304	0.707
681	543.054			0.378	0.905
682	543.258			0.341	0.806
683	543.551			0.358	0.852
684	543.926			0.379	0.908
685	544.294			0.405	0.978
686	544.604		5.95	0.424	1.029

Stop Flow

Table 10 (Continued): Aluminum Oxide Transport Data – Study #2_pH 6

Data results for aluminum oxide nanoparticle transport Study #2_pH 6; samples 687-719.

Sample	Pore Volume (mL)	Influent pH	Effluent pH	UV-Vis Abs	C/C _o
687	544.826			0.367	0.876
688	545.048			0.369	0.881
689	545.285			0.365	0.870
690	545.483			0.424	1.029
691	545.745			0.388	0.932
692	545.981			0.383	0.919
693	546.225			0.383	0.919
694	546.550		5.84	0.396	0.954
695	546.933			0.375	0.897
696	547.348			0.383	0.919
697	547.775			0.376	0.900
698	548.255			0.386	0.927
699	548.828		5.83	0.368	0.878
700	551.231		5.93		
701	553.468			0.384	0.921
702	556.047		5.88		
703	558.646			0.387	0.929
704	560.714		5.93		
705	562.766			0.367	0.876
706	564.899	5.97			
707	566.993			0.408	0.986
708	567.237				
709	567.470			0.372	0.889
710	567.811	5.96	5.95		
711	568.212			0.111	0.189
712	568.422			0.238	0.529
713	568.629			0.233	0.515
714	568.834			0.218	0.473
715	569.034			0.250	0.563
716	569.237			0.260	0.591
717	569.460			0.301	0.706
718	569.678			0.314	0.742
719	569.885		5.93	0.352	0.849

Stop Flow

Table 10 (Continued): Aluminum Oxide Transport Data – Study #2_pH 6

Data results for aluminum oxide nanoparticle transport Study #2_pH 6; samples 720-752.

Sample	Pore Volume (mL)	Influent pH	Effluent pH	UV-Vis Abs	C/C ₀
720	570.086			0.349	0.841
721	570.308			0.356	0.860
722	570.522			0.366	0.888
723	570.733			0.355	0.857
724	570.943			0.365	0.885
725	571.318		5.94		
726	571.730			0.385	0.942
727	572.119			0.350	0.843
728	572.639			0.372	0.905
729	572.994			0.365	0.885
730	573.288		5.93	0.370	0.899
731	574.642		5.91		
732	575.902			0.363	0.880
733	575.652		5.91		
734	579.188			0.374	0.911
735	585.007		5.95		
736	587.081	5.96		0.358	0.866
737	588.836		6.02		
738	590.655			0.379	0.925
739	592.560		5.96		
740	594.360			0.370	0.899
741	596.523		5.96		
742	598.691			0.355	0.857
743	599.245	5.95	6.03		
744	599.805			0.352	0.849
745	600.091			0.104	0.187
746	600.339			0.124	0.240
747	600.690			0.120	0.229
748	601.121			0.167	0.353
749	601.555			0.285	0.717
750	601.892			0.316	0.811
751	602.204		6.03	0.306	0.781
752	602.562			0.332	0.860

Stop Flow

Table 10 (Continued): Aluminum Oxide Transport Data – Study #2_pH 6

Data results for aluminum oxide nanoparticle transport Study #2_pH 6; samples 753-768.

Sample	Pore Volume (mL)	Influent pH	Effluent pH	UV-Vis Abs	C/C _o
753	602.857			0.326	0.842
754	603.154		5.91	0.325	0.839
755	603.451			0.320	0.824
756	603.773			0.319	0.821
757	604.181			0.325	0.839
758	604.581			0.332	0.860
759	604.906			0.339	0.881
760	605.554		5.92	0.339	0.881
761	608.579		5.90		
762	611.208			0.340	0.884
763	612.881		5.93		
764	614.577	5.98		0.337	0.875
765	615.981		5.90		
766	617.461			0.339	0.881
767	619.605		5.93		
768	621.732			0.328	0.848

Table 11: Non-Reactive Tracer Study Data – Study #3_pH 6_NRT

Performed for Al₂O₃ Study #3_pH 6

Column: D

Darcy Velocity: 0.010 cm/min

Electrolyte: KCl

Ionic Strength: 0.015 M

Data results for pentafluorobenzoic acid transport Study #3_pH 6_NRT; Samples 1 - 27.

Sample	Pore Volume (mL)	UV-Vis Abs	Dilution	C/C _o	
1	-0.514	0.014	1	0.000	LDL
2	-0.378	0.006	1	-0.002	LDL
3	-0.219	0.003	1	-0.002	LDL
4	-0.026	0.003	1	-0.002	LDL
5	0.189	0.011	1	-0.001	LDL
6	0.403	0.240	1	0.031	
7	0.635	2.568	1	0.344	
8	0.863	1.822	2.9	0.721	
9	1.075	2.381	2.6	0.838	
10	1.293	2.381	2.8	0.896	
11	1.499	2.725	2.4	0.901	
12	1.696	2.370	2.9	0.940	
13	1.910	2.541	2.7	0.942	
14	2.192	2.725	2.6	0.950	
15	2.550	2.499	2.8	0.965	
16	2.913	2.460	2.9	0.973	
17	3.248	2.460	2.9	0.976	
18	3.644	2.828	2.5	0.964	
19	4.117	2.642	2.7	0.980	
20	4.576	2.323	3.2	0.993	
21	5.017	2.323	3.2	0.999	
22	5.946	2.332	3.1	0.977	
23	6.765	2.332	3.2	0.999	
24	7.746	2.541	2.9	0.987	
25	8.560	2.191	3.4	1.003	
26	9.370	2.725	2.7	0.981	
27	10.195	2.332	3.2	1.001	

Table 11 (Continued): Non-Reactive Tracer Study Data – Study #3_pH 6_NRT

Data results for pentafluorobenzoic acid transport Study #3_pH 6_NRT; Samples 28 - 53.

Sample	Pore Volume (mL)	UV-Vis Abs	Dilution	C/C _o	
28	10.443	2.527	2.9	0.995	Elution
29	10.668	2.436	3.0	0.997	
30	10.874	2.381	3.1	1.001	
31	11.088	2.662	2.7	0.979	
32	11.322	2.589	2.8	0.976	
33	11.546	1.752	2.9	0.696	
34	11.765	0.791	3.0	0.315	
35	11.951	1.285	1	0.169	
36	12.141	0.868	1	0.112	
37	12.359	0.623	1	0.082	
38	12.581	0.476	1	0.062	
39	12.799	0.391	1	0.051	
40	13.099	0.314	1	0.041	
41	13.477	0.251	1	0.032	
42	13.866	0.214	1	0.027	
43	14.332	0.178	1	0.022	
44	14.816	0.154	1	0.019	
45	15.875	0.119	1	0.014	
46	16.825	0.100	1	0.012	
47	17.809	0.080	1	0.009	
48	18.849	0.062	1	0.006	
49	20.071	0.048	1	0.004	
50	20.961	0.042	1	0.004	
51	21.985	0.034	1	0.002	
52	22.922	0.027	1	0.001	
53	23.787	0.018	1	0.000	LDL

Table 12: Aluminum Oxide Transport Data – Study #3_pH 6

Concentration: 100 mg/L
 Column: D
 Darcy Velocity: 0.096 cm/min
 Electrolyte: KCl
 Ionic Strength: 0.015 M

Data results for aluminum oxide nanoparticle transport Study #3_pH 6; samples 1-27.

Sample	Pore Volume (mL)	Influent pH	Effluent pH	UV-Vis Abs	C/C _o
1	-0.505			0.078	0.057
2	-0.308		6.06	0.046	0.039
3	-0.125			0.035	0.033
4	0.062		6.24	0.078	0.057
5	0.305			0.073	0.054
6	0.557		6.22	0.040	0.036
7	0.825			0.061	0.047
8	1.074		6.27	0.081	0.059
9	1.305			0.099	0.069
10	1.573		6.15	0.070	0.052
11	1.887			0.065	0.050
12	2.226		6.20	0.090	0.064
13	2.616			0.091	0.064
14	3.040		6.13	0.104	0.071
15	3.433			0.098	0.068
16	3.887		5.95	0.092	0.065
17	4.376			0.086	0.061
18	4.846	6.07	6.08	0.084	0.060
19	5.324			0.083	0.060
20	5.786		6.12	0.076	0.056
21	6.241			0.085	0.061
22	6.753		6.02	0.081	0.059
23	7.708			0.099	0.069
24	8.638		6.04	0.092	0.065
25	9.799	6.10		0.103	0.071
26	11.065		6.05	0.090	0.064
27	12.156			0.096	0.067

Table 12 (Continued): Aluminum Oxide Transport Data – Study #3_pH 6

Data results for aluminum oxide nanoparticle transport Study #3_pH 6; samples 28 - 60.

Sample	Pore Volume (mL)	Influent pH	Effluent pH	UV-Vis Abs	C/C ₀
28	13.260	6.13	6.09	0.113	0.076
29	14.543			0.128	0.085
30	15.671		6.01	0.118	0.079
31	19.871			0.142	0.093
32	21.506	6.10	5.99	0.171	0.109
33	23.614			0.122	0.081
34	24.119			0.115	0.077
35	25.832			0.145	0.093
36	27.415		6.03	0.154	0.098
37	29.247	6.13		0.188	0.117
38	30.682		5.86	0.164	0.104
39	34.102			0.181	0.113
40	38.220	6.13	6.10	0.213	0.131
41	40.396			0.261	0.158
42	42.859		5.89	0.294	0.160
43	44.943			0.311	0.170
44	47.388		6.07	0.313	0.172
45	49.016	6.02		0.350	0.195
46	51.446		6.09	0.321	0.177
47	53.790			0.384	0.219
48	55.574	6.01	5.83	0.416	0.239
49	59.305			0.445	0.258
50	64.454	5.98	5.97	0.563	0.332
51	66.605			0.583	0.345
52	68.980	6.07		0.677	0.404
53	69.294			0.653	0.389
54	75.835			0.800	0.479
55	77.986			0.805	0.482
56	81.824	5.99	5.88	0.863	0.518
57	85.527			0.874	0.525
58	87.662	5.98		0.915	0.551
59	90.354			1.027	0.617
60	92.319		5.93	1.042	0.626

Table 12 (Continued): Aluminum Oxide Transport Data – Study #3_pH 6

Data results for aluminum oxide nanoparticle transport Study #3_pH 6; samples 61 - 93.

Sample	Pore Volume (mL)	Influent pH	Effluent pH	UV-Vis Abs	C/C _o	
61	95.105			1.081	0.655	
62	95.470	5.95		0.259	0.139	Stop Flow
63	95.749		5.92	0.393	0.223	
64	96.073			0.543	0.317	
65	96.406		5.91	0.768	0.459	
66	96.761			0.994	0.600	
67	97.171		5.95	1.058	0.641	
68	97.626			1.079	0.654	
69	98.064		5.90	1.077	0.653	
70	98.439			1.077	0.653	
71	98.810		5.90	1.096	0.664	
72	100.736			1.116	0.677	
73	104.697		5.95	1.163	0.707	
74	108.430			1.177	0.715	
75	111.688	5.95		1.173	0.713	
76	112.729		6.15	1.203	0.742	
77	116.907			1.217	0.751	
78	120.650		6.07	1.237	0.764	
79	123.260	5.95		1.270	0.785	
80	126.623			1.361	0.812	
81	129.917			1.397	0.834	
82	133.933			1.393	0.832	
83	135.981		5.99	1.429	0.854	
84	136.906	5.96		1.392	0.831	
85	139.547			1.414	0.845	
86	142.123	6.05		1.433	0.856	
87	147.471			1.450	0.863	
88	151.863			1.446	0.861	
89	156.125			1.450	0.863	
90	160.049			1.450	0.863	
91	160.383	5.98		1.404	0.835	Elution
92	160.641		6.07	1.381	0.821	
93	160.897			1.415	0.842	

Table 12 (Continued): Aluminum Oxide Transport Data – Study #3_pH 6

Data results for aluminum oxide nanoparticle transport Study #3_pH 6; samples 94 - 106.

Sample	Pore Volume (mL)	Influent pH	Effluent pH	UV-Vis Abs	C/C _o
94	161.144		6.12	1.388	0.825
95	161.536			0.486	0.274
96	161.977		6.05	0.177	0.109
97	162.384			0.062	0.047
98	162.777		6.01	0.044	0.037
99	163.155			0.044	0.037
100	163.449		5.95	0.064	0.048
101	164.494			0.060	0.046
102	165.415		5.88	0.034	0.032
103	166.408			0.034	0.032
104	167.804		5.92	0.024	0.026
105	169.249			0.013	0.020
106	170.497			0.010	0.019

Table 13: Non-Reactive Tracer Study Data – Study #4_pH 9_NRT

Performed for Al₂O₃ Study #4_pH 9

Column: A

Darcy Velocity: 0.097 cm/min

Electrolyte: K₂HPO₄/K₃HPO₄

Ionic Strength: 0.015 M

Data results for pentafluorobenzoic acid transport Study #4_pH 9_NRT; Samples 1 - 26.

Sample	Pore Volume (mL)	UV-Vis Abs	Dilution	C/C ₀	
1	-0.315	0.023	1	0.001	LDL
2	0.014	0.020	1	0.001	LDL
3	0.335	0.226	1	0.027	
4	0.681	2.199	1	0.284	
5	1.020	1.968	3	0.786	
6	1.353	2.392	3	0.958	
7	1.688	2.500	3	1.002	
8	2.032	2.500	3	1.002	
9	2.393	2.487	3	0.996	
10	2.737	2.487	3	0.996	
11	3.074	2.528	3	1.013	
12	3.539	2.542	3	1.019	
13	4.146	2.528	3	1.013	
14	4.730	2.487	3	0.996	
15	5.451	2.487	3	0.996	
16	6.356	2.514	3	1.007	
17	7.291	2.514	3	1.007	
18	8.214	2.487	3	0.996	
19	9.132	2.487	3	0.996	
20	10.076	2.324	3	0.930	
21	11.217	2.487	3	0.996	
22	12.382	2.542	3	1.019	
23	13.087	2.500	3	1.002	Elution
24	13.443	2.487	3	0.996	
25	13.781	2.414	3	0.967	
26	14.084	1.823	3	0.727	

Table 13 (Continued): Non-Reactive Tracer Study Data – Study #4_pH 9_NRT

Data results for pentafluorobenzoic acid transport Study #4_pH 9_NRT; Samples 27 - 44.

Sample	Pore Volume (mL)	UV-Vis Abs	Dilution	C/C ₀	
27	14.422	2.114	1	0.273	
28	14.793	0.544	1	0.060	
29	15.154	0.251	1	0.031	
30	15.489	0.170	1	0.020	
31	15.835	0.131	1	0.015	
32	16.257	0.103	1	0.012	
33	16.723	0.081	1	0.009	
34	17.117	0.071	1	0.008	
35	17.822	0.055	1	0.006	
36	18.881	0.046	1	0.005	
37	19.910	0.036	1	0.003	
38	20.886	0.036	1	0.003	
39	21.807	0.036	1	0.003	
40	22.797	0.030	1	0.003	
41	23.874	0.025	1	0.002	
42	24.964	0.029	1	0.002	
43	26.030	0.023	1	0.002	LDL
44	27.009	0.025	1	0.002	LDL

Table 14: Aluminum Oxide Transport Data – Study #4_pH 9

Concentration: 100 mg/L
Column: A
Darcy Velocity: 0.098 cm/min
Electrolyte: K₂HPO₄/K₃HPO₄
Ionic Strength: 0.015 M

Data results for aluminum oxide nanoparticle transport Study #4_pH 9; samples 1 - 27.

Sample	Pore Volume (mL)	Influent pH	Effluent pH	UV-Vis Abs	C/C ₀
1	-0.443			0.053	0.025
2	-0.246			0.063	0.031
3	-0.054			0.058	0.028
4	0.151			0.070	0.035
5	0.358			0.097	0.052
6	0.581	9.44		0.232	0.119
7	0.806		8.86	0.608	0.347
8	1.089			0.826	0.479
9	1.476		9.09	1.178	0.693
10	1.856			1.363	0.805
11	2.224		9.20	1.418	0.838
12	2.588			1.508	0.893
13	2.997	9.48	9.17	1.547	0.916
14	3.449			1.567	0.928
15	3.881		9.19	1.634	0.969
16	4.286			1.688	1.002
17	4.666			1.677	0.995
18	4.952			1.749	1.039
19	5.362		9.11		
20	5.771	9.42		1.705	1.012
21	6.168		9.23		
22	6.583			1.716	1.019
23	7.006		9.25		
24	7.416			1.739	1.033
25	7.834	9.34	9.23		
26	8.198			1.766	1.049
27	8.630		9.20		

Table 14 (Continued): Aluminum Oxide Transport Data – Study #4_pH 9

Data results for aluminum oxide nanoparticle transport Study #4_pH 9; samples 28 - 61.

Sample	Pore Volume (mL)	Influent pH	Effluent pH	UV-Vis Abs	C/C ₀	
28	9.057			1.661	0.985	
29	9.493		9.17			
30	9.921			1.661	0.985	
31	10.404		9.19			
32	10.898	9.30		1.782	1.059	
33	11.362		9.17			
34	11.882			1.673	0.993	
35	12.139			1.806	1.073	
36	12.353			1.927	1.147	
37	12.540			1.909	1.136	
38	12.819			1.322	0.780	
39	13.159		8.95	0.690	0.397	
40	13.504			0.202	0.101	
41	13.893			0.128	0.071	
42	14.278		9.01	0.091	0.048	
43	14.739	9.25		0.084	0.044	
44	15.239			0.138	0.077	Elution
45	15.664		8.93	0.196	0.113	
46	16.038			0.080	0.042	
47	16.410			0.091	0.048	
48	16.724		8.90	0.139	0.078	
49	17.148		9.14			
50	17.562			0.067	0.034	
51	17.962		9.04			
52	18.351			0.156	0.088	
53	18.732	9.20	9.06			
54	19.126			0.051	0.024	
55	19.531		9.05			
56	19.923			0.287	0.169	
57	20.317		9.04			
58	20.709			0.163	0.093	
59	21.183		9.04			
60	21.666			0.234	0.120	
61	22.065		9.02			

Table 14 (Continued): Aluminum Oxide Transport Data – Study #4_pH 9

Data results for aluminum oxide nanoparticle transport Study #4 pH 9; samples 62 - 74.

Sample	Pore Volume (mL)	Influent pH	Effluent pH	UV-Vis Abs	C/C ₀
62	22.458			0.191	0.094
63	22.912		9.04		
64	23.364			0.131	0.073
65	23.759		9.03		
66	24.163	9.14		0.142	0.080
67	24.549		8.86		
68	24.931			0.114	0.063
69	25.341	9.10	8.98		
70	25.747			0.128	0.071
71	26.150		9.01		
72	26.559			0.037	0.015
73	26.952		8.98		
74	27.352			0.827	0.502

Table 15: Non-Reactive Tracer Study Data – Study #5_pH 9_NRTPerformed for Al₂O₃ Study #5_pH 9

Column: A

Darcy Velocity: 0.098 cm/min

Electrolyte: K₂HPO₄/K₃HPO₄

Ionic Strength: 0.015 M

Data results for pentafluorobenzoic acid transport Study #5_pH 9_NRT; Samples 1 - 29.

Sample	Pore Volume (mL)	UV-Vis Abs	Dilution	C/C ₀	
1	-0.315	0.011	1	-0.006	LDL
2	-0.134	0.005	1	-0.007	LDL
3	0.042	0.002	1	-0.001	LDL
4	0.225	0.002	1	-0.004	LDL
5	0.420	0.028	1	-0.001	LDL
6	0.634	1.189	1	0.158	
7	0.857	1.682	2.9	0.674	
8	1.133	2.328	2.9	0.919	
9	1.488	2.699	2.6	0.958	
10	1.841	2.745	2.6	0.974	
11	2.188	2.568	2.8	0.989	
12	2.536	2.553	2.8	0.989	
13	2.895	2.602	2.8	0.984	
14	3.244	2.328	3.1	0.991	
15	3.504	2.432	3.0	0.998	
16	4.236	2.745	2.7	0.995	
17	4.966	2.620	2.8	0.990	
18	5.726	2.602	2.8	0.990	
19	6.515	2.168	3.4	1.011	
20	7.341	2.319	3.2	1.007	
21	8.114	2.420	3.0	1.006	
22	8.864	2.482	3.0	1.006	
24	10.307	2.301	3.2	1.010	
25	10.533	2.523	2.9	0.997	Elution
26	10.713	2.377	3.1	1.004	
27	10.896	2.456	3.0	1.000	
28	11.077	2.444	3.0	0.999	
29	11.267	2.282	3.0	1.002	

Table 15 (Continued): Non-Reactive Tracer Study Data – Study #5_pH 9_NRT

Data results for pentafluorobenzoic acid transport Study #5_pH 9_NRT; Samples 30 - 48.

Sample	Pore Volume (mL)	UV-Vis Abs	Dilution	C/C _o	
30	11.457	2.071	3.2	0.914	
31	11.641	1.169	3.0	0.480	
32	11.816	0.396	3.2	0.167	
33	12.075	0.436	1	0.057	
34	12.424	0.197	1	0.025	
35	12.776	0.117	1	0.014	
36	13.127	0.082	1	0.010	
37	13.470	0.065	1	0.008	
38	13.794	0.056	1	0.005	
39	14.040	0.053	1	0.005	
40	14.790	0.043	1	0.002	
41	15.546	0.032	1	-0.001	LDL
42	16.405	0.027	1	-0.002	LDL
43	17.164	0.025	1	-0.002	LDL
44	17.920	0.021	1	-0.003	LDL
45	18.679	0.021	1	-0.003	LDL
46	19.443	0.023	1	-0.003	LDL
47	20.191	0.021	1	-0.003	LDL
48	20.902	0.012	1	-0.006	LDL

Table 16: Aluminum Oxide Transport Data – Study #5_pH 9

Concentration: 100 mg/L
 Column: A
 Darcy Velocity: 0.098 cm/min
 Electrolyte: K₂HPO₄/K₃HPO₄
 Ionic Strength: 0.015 M

Data results for aluminum oxide nanoparticle transport Study #5_pH 9; samples 1 - 27.

Sample	Pore Volume (mL)	Influent pH	Effluent pH	UV-Vis Abs	C/C ₀	
1	-0.312			0.024	-0.001	LDL
2	-0.126			0.005	-0.012	LDL
3	0.063			0.007	-0.011	LDL
4	0.243			0.002	-0.013	LDL
5	0.415			0.019	-0.004	LDL
6	0.592			0.124	0.055	
7	0.782			0.319	0.160	
8	0.967		8.55	0.489	0.258	
9	1.134			0.611	0.337	
10	1.322			0.742	0.422	
11	1.518			0.885	0.514	
12	1.722			1.011	0.595	
13	1.925			1.118	0.664	
14	2.110			1.192	0.712	
15	2.378		8.84	1.285	0.772	
16	2.744	9.34		1.359	0.820	
17	3.108			1.400	0.846	
18	3.440		8.87	1.447	0.876	
19	3.764			1.470	0.891	
20	4.093			1.506	0.914	
21	4.442		8.88	1.504	0.913	
22	4.803			1.530	0.930	
24	5.461		8.93			
25	5.850			1.548	0.942	
26	6.262		8.9			
27	6.687			1.559	0.949	

Table 16 (Continued): Aluminum Oxide Transport Data – Study #5_pH 9

Data results for aluminum oxide nanoparticle transport Study #5_pH 9; samples 28 - 60.

Sample	Pore Volume (mL)	Influent pH	Effluent pH	UV-Vis Abs	C/C _o
28	7.125	9.29	8.85		
29	7.548			1.585	0.965
30	7.998		8.84		
31	8.404			1.595	0.972
32	8.843	9.25			
33	9.272			1.595	0.972
34	9.668		8.8		
35	10.096			1.595	0.972
36	10.507		8.84		
37	10.903			1.595	0.972
38	11.303		8.86		
39	11.703			1.609	0.981
40	12.106		8.84		
41	12.506			1.597	0.973
42	12.903		8.84		
43	13.333	9.2		1.609	0.981
44	13.758		8.76		
45	14.174			1.609	0.981
46	14.592		8.8		
47	14.995			1.609	0.981
48	15.629		8.8		
49	16.253			1.614	0.984
50	16.504			1.595	0.972
51	16.684			1.600	0.975
52	16.860			1.607	0.980
53	17.056			1.590	0.969
54	17.264			1.540	0.936
55	17.452			1.186	0.708
56	17.623			0.670	0.375
57	17.799	9.3		0.327	0.154
58	17.983		8.74	0.168	0.079
59	18.159			0.110	0.048
60	18.330			0.077	0.028

Elution

Table 16 (Continued): Aluminum Oxide Transport Data – Study #5_pH 9

Data results for aluminum oxide nanoparticle transport Study #5_pH 9; samples 61 - 96.

Sample	Pore Volume (mL)	Influent pH	Effluent pH	UV-Vis Abs	C/C ₀
61	18.495			0.062	0.020
62	18.663			0.054	0.015
63	18.919			0.044	0.010
64	19.266		8.85	0.034	0.004
65	19.603			0.088	0.034
66	19.909			0.122	0.054
67	20.181			0.546	0.295
68	20.365		8.8	0.353	0.171
69	20.553			0.129	0.058
70	20.730			0.245	0.120
71	20.908			0.095	0.038
72	21.098			0.061	0.019
73	21.401			0.187	0.089
74	21.689			0.106	0.045
75	22.115	9.27	8.84		
76	22.556			0.166	0.078
77	22.956		8.82		
78	23.343			0.050	0.013
79	23.755		8.82		
80	24.178			0.065	0.021
81	24.594		8.86		
82	24.990	9.2		0.040	0.007
83	25.388		8.8		
84	25.805			0.140	0.064
85	26.234		8.79		
86	26.680			0.049	0.012
87	27.148		8.81		
88	27.619			0.086	0.033
89	28.039		8.77		
90	28.411			0.162	0.076
91	28.790		8.77		
92	29.222			0.284	0.141
93	29.662		8.77		
94	30.064			0.196	0.094
95	30.473		8.81		
96	30.880	9.2		0.099	0.042

Table 17: Non-Reactive Tracer Study Data – Study #6_pH 9_NRTPerformed for Al₂O₃ Study #6_pH 9

Column: A

Darcy Velocity: 0.098 cm/min

Electrolyte: K₂HPO₄/K₃HPO₄

Ionic Strength: 0.015 M

Data results for pentafluorobenzoic acid transport Study #6_pH 9_NRT; Samples 1 - 28.

Sample	Pore Volume (mL)	UV-Vis Abs	Dilution	C/C ₀	
1	-0.359	0.019	1	0.001	LDL
2	-0.146	0.010	1	0.000	LDL
3	0.058	0.007	1	-0.001	LDL
4	0.291	0.033	1	0.002	
5	0.528	0.190	1	0.020	
6	0.731	1.807	1	0.241	
7	0.945	1.625	3.0	0.666	
8	1.183	2.194	3.0	0.891	
9	1.497	2.347	3.0	0.956	
10	1.877	2.387	3.0	0.970	
11	2.258	2.409	3.0	0.982	
12	2.634	2.409	3.0	0.979	
13	3.000	2.444	3.0	0.991	
14	3.434	2.444	3.0	0.991	
15	3.784	2.420	3.0	0.985	
16	4.645	2.420	3.0	0.984	
17	5.508	2.468	3.0	0.999	
18	6.371	2.468	3.0	1.000	
19	7.168	2.495	3.0	1.007	
20	7.980	2.468	3.0	0.999	
21	8.830	2.468	3.0	0.996	
22	9.708	2.301	3.2	1.007	
24	10.827	2.769	2.6	0.990	Elution
25	11.040	2.824	2.7	0.979	
26	11.264	2.495	2.7	1.001	
27	11.481	2.409	2.7	1.013	
28	11.678	2.131	2.7	0.989	

Table 17 (Continued): Non-Reactive Tracer Study Data – Study #6_pH 9_NRT

Data results for pentafluorobenzoic acid transport Study #6_pH 9_NRT; Samples 29 - 48.

Sample	Pore Volume (mL)	UV-Vis Abs	Dilution	C/C _o	
29	11.905	2.046	2.7	0.797	
30	12.222	0.943	2.6	0.298	
31	12.597	0.279	2.5	0.069	
32	12.962	0.282	1	0.036	
33	13.330	0.202	1	0.025	
34	13.705	0.161	1	0.019	
35	14.091	0.131	1	0.015	
36	14.378	0.119	1	0.014	
37	15.187	0.102	1	0.011	
38	16.003	0.065	1	0.006	
39	16.862	0.067	1	0.006	
40	17.753	0.045	1	0.004	
41	18.637	0.034	1	0.002	
42	19.528	0.039	1	0.003	
43	20.469	0.125	1	0.015	
44	20.891	0.024	1	0.001	LDL
45	21.795	0.018	1	0.001	LDL
46	22.637	0.029	1	0.002	
47	23.565	0.017	1	0.000	LDL
48	24.408	0.011	1	0.000	LDL

Table 18: Aluminum Oxide Transport Data – Study #6_pH 9

Concentration: 100 mg/L
 Column: A
 Darcy Velocity: 0.098 cm/min
 Electrolyte: K₂HPO₄/K₃HPO₄
 Ionic Strength: 0.015 M

Data results for aluminum oxide nanoparticle transport Study #6_pH 9; samples 1 - 27.

Sample	Pore Volume (mL)	Influent pH	Effluent pH	UV-Vis Abs	C/C ₀	
1	-0.380			0.008	-0.010	LDL
2	-0.165			-0.008	-0.018	LDL
3	0.027			-0.008	-0.018	LDL
4	0.231			-0.003	-0.015	LDL
5	0.430			0.007	-0.010	LDL
6	0.631			0.071	0.024	
7	0.826			0.161	0.073	
8	1.026			0.283	0.137	
9	1.230			0.422	0.209	
10	1.443			0.608	0.325	
11	1.653			0.795	0.442	
12	1.857		8.70	0.986	0.561	
13	2.069			1.093	0.628	
14	2.364	9.15		1.273	0.741	
15	2.722			1.337	0.781	
16	3.098			1.485	0.873	
17	3.487			1.447	0.849	
18	3.854		8.80	1.477	0.868	
19	4.244			1.529	0.901	
20	4.634			1.525	0.898	
21	5.003			1.543	0.909	
22	5.361	9.13	8.89	1.560	0.920	
23	5.731			1.597	0.943	
24	6.098			1.564	0.922	
25	6.464			1.726	1.024	
26	6.825		8.89	1.596	0.942	
27	7.098			1.611	0.952	

Table 18 (Continued): Aluminum Oxide Transport Data – Study #6_pH 9

Data results for aluminum oxide nanoparticle transport Study #6_pH 9; samples 28 - 60.

Sample	Pore Volume (mL)	Influent pH	Effluent pH	UV-Vis Abs	C/C _o	
28	7.495		8.89			
29	7.915			1.597	0.943	
30	8.338		8.86			
31	8.737			1.633	0.966	
32	9.138	9.09	8.84			
33	9.539			1.660	0.982	
34	9.938		8.88			
35	10.335			1.615	0.954	
36	10.732		8.84			
37	11.063			1.611	0.952	
38	11.582		8.89			
39	11.981			1.615	0.954	
40	12.379		8.89			
41	12.780			1.611	0.952	
42	12.985	9.06		1.611	0.952	
43	13.226	9.14		1.564	0.922	Elution
44	13.450			1.576	0.930	
45	13.701			1.589	0.938	
46	13.936			1.584	0.935	
47	14.175			1.394	0.816	
48	14.395			0.912	0.515	
49	14.591		8.78	0.481	0.245	
50	14.783			0.247	0.118	
51	14.988			0.138	0.061	
52	15.190			0.093	0.036	
53	15.388			0.079	0.028	
54	15.685			0.064	0.020	
55	16.055			0.055	0.015	LDL
56	16.445		8.83	0.072	0.024	
57	16.843	9.13		0.042	0.008	LDL
58	17.218			0.036	0.005	LDL
59	17.636			0.042	0.008	LDL
60	17.959			0.024	-0.001	LDL

Table 18 (Continued): Aluminum Oxide Transport Data – Study #6_pH 9

Data results for aluminum oxide nanoparticle transport Study #6_pH 9; samples 61 - 74.

Sample	Pore Volume (mL)	Influent pH	Effluent pH	UV-Vis Abs	C/C _o	
61	18.365		8.89			LDL
62	18.768			0.018	-0.004	LDL
63	19.182		8.83			LDL
64	19.607			0.012	-0.007	LDL
65	20.001		8.79			LDL
66	20.396			0.010	-0.009	LDL
67	20.790	9.10	8.81			LDL
68	21.175			0.007	-0.010	LDL
69	21.562		8.82			LDL
70	21.966			0.005	-0.011	LDL
71	22.405		8.84			LDL
72	22.868			0.003	-0.012	LDL
73	23.274		8.82			LDL
74	23.648			0.004	-0.012	LDL

Table 19: Non-Reactive Tracer Study Data – Study #7_pH 9_NRTPerformed for Al₂O₃ Study #7_pH 9

Column: A

Darcy Velocity: 0.025 cm/min

Electrolyte: K₂HPO₄/K₃HPO₄

Ionic Strength: 0.015 M

Data results for pentafluorobenzoic acid transport Study #7_pH 9_NRT; Samples 1 - 28.

Sample	Pore Volume (mL)	UV-Vis Abs	Dilution	C/C _o	
1	-0.447	0.012	1	0.000	LDL
2	-0.148	0.005	1	-0.001	LDL
3	0.179	0.006	1	0.000	LDL
4	0.483	0.965	1	0.131	
5	0.790	1.726	2.9	0.695	
6	1.102	2.377	2.8	0.905	
7	1.377	2.319	3.0	0.942	
8	1.633	2.310	3.0	0.964	
9	1.901	2.468	2.9	0.970	
10	2.195	2.468	2.9	0.969	
11	2.568	2.337	3.1	0.980	
12	2.978	2.268	3.2	0.983	
13	3.346	1.836	4.0	1.004	
14	3.719	2.319	3.1	0.997	
15	4.061	1.963	3.7	0.990	
16	4.392	2.620	2.8	0.990	
17	4.781	2.456	2.7	0.925	
18	5.033	2.174	3.2	0.977	
19	5.278	2.420	2.9	0.991	
20	5.544	2.310	3.0	0.979	
21	5.822	2.174	3.3	0.995	
22	6.111	2.260	3.2	1.031	
23	6.378	2.537	2.8	1.015	
24	6.705	2.620	2.7	1.013	
25	7.097	2.620	2.8	1.022	
26	7.506	2.387	3.0	1.024	
27	8.717	2.237	3.3	1.046	
28	9.874	2.456	3.0	1.024	

Table 19 (Continued): Non-Reactive Tracer Study Data – Study #7_pH 9_NRT

Data results for pentafluorobenzoic acid transport Study #7_pH 9_NRT; Samples 29 - 62.

Sample	Pore Volume (mL)	UV-Vis Abs	Dilution	C/C ₀	
29	11.137	2.854	2.4	0.975	
30	11.717	2.468	3.0	1.026	
31	12.050	2.537	2.9	1.040	Elution
32	12.332	2.432	3.0	1.025	
33	12.640	2.409	3.0	1.034	
34	12.945	2.194	2.9	0.898	
35	13.253	0.959	3.1	0.411	
36	13.549	0.349	2.8	0.132	
37	13.826	0.547	1	0.071	
38	14.117	0.388	1	0.052	
39	14.456	0.286	1	0.038	
40	14.799	0.215	1	0.028	
41	15.098	0.191	1	0.025	
42	15.409	0.158	1	0.020	
43	15.759	0.889	1	0.116	
44	16.028	0.454	1	0.060	
45	16.290	0.235	1	0.031	
46	16.521	0.374	1	0.049	
47	16.786	0.468	1	0.062	
48	17.120	0.179	1	0.023	
49	17.430	0.084	1	0.011	
50	17.727	0.058	1	0.007	
51	18.057	0.047	1	0.006	
52	18.374	0.048	1	0.006	
53	18.705	0.045	1	0.005	
54	19.026	0.043	1	0.005	
55	19.300	0.036	1	0.004	
56	19.574	0.037	1	0.004	
57	19.861	0.035	1	0.004	
58	20.208	0.029	1	0.003	
59	20.579	0.033	1	0.004	
60	20.916	0.034	1	0.004	
61	21.322	0.045	1	0.005	
62	21.707	0.032	1	0.004	

Table 19 (Continued): Non-Reactive Tracer Study Data – Study #7_pH 9_NRT

Data results for pentafluorobenzoic acid transport Study #7_pH 9_NRT; Samples 63 - 70.

Sample	Pore Volume (mL)	UV-Vis Abs	Dilution	C/C ₀	
63	22.013	0.041	1	0.005	
64	22.316	0.043	1	0.005	
65	22.620	0.041	1	0.005	
66	22.937	0.021	1	0.002	LDL
67	23.216	0.022	1	0.002	LDL
68	23.454	0.023	1	0.002	LDL
69	23.685	0.025	1	0.003	LDL
70	23.894	0.019	1	0.002	LDL

Table 20: Aluminum Oxide Transport Data – Study #7_pH 9

Concentration: 100 mg/L
 Column: A
 Darcy Velocity: 0.025 cm/min
 Electrolyte: K_2HPO_4/K_3HPO_4
 Ionic Strength: 0.015 M

Data results for aluminum oxide nanoparticle transport Study #7_pH 9; samples 1 - 28.

Sample	Pore Volume (mL)	Influent pH	Effluent pH	UV-Vis Abs	C/C _o	
1	-0.432			-0.032	-0.031	LDL
2	-0.133		8.61	0.015	-0.006	LDL
3	0.169			-0.004	-0.016	LDL
4	0.448			0.020	-0.003	LDL
5	0.708		8.68	0.107	0.042	
6	0.977	9.01		0.196	0.097	
7	1.246		8.77	0.447	0.258	
8	1.513			0.659	0.393	
9	1.790		8.63	0.902	0.553	
10	2.067			1.078	0.654	
11	2.372		8.85	1.248	0.753	
12	2.675			1.359	0.817	
13	2.938	9.04	8.84	1.408	0.845	
14	3.218			1.499	0.898	
15	3.517		8.77	1.545	0.925	
16	3.829			1.518	0.909	
18	4.421	8.99		1.565	0.936	
19	4.685		8.77	1.588	0.949	
20	4.965			1.588	0.949	
21	5.252		8.77	1.596	0.954	
22	5.528	9.37		1.576	0.942	
23	5.811		8.8	1.591	0.951	
24	6.119			1.625	0.971	
25	6.434		8.78	1.621	0.969	
26	6.760			1.591	0.951	
27	7.153		8.72	1.552	0.929	
28	7.522			1.518	0.909	

Table 20 (Continued): Aluminum Oxide Transport Data – Study #7_pH 9

Data results for aluminum oxide nanoparticle transport Study #7_pH 9; samples 29 - 61.

Sample	Pore Volume (mL)	Influent pH	Effluent pH	UV-Vis Abs	C/C _o
29	7.837			1.528	0.914
30	8.103		8.74	1.525	0.913
31	8.363			1.542	0.922
32	8.621		8.86	1.554	0.929
33	8.897			1.707	1.018
34	9.139		8.8	1.580	0.944
35	9.421	9.05		1.586	0.948
37	10.004	9.15		1.607	0.960
38	10.270		8.89	1.598	0.955
39	10.542			1.608	0.961
40	10.768		8.86	1.608	0.961
41	10.995			1.612	0.963
42	11.241		8.78	1.628	0.972
43	11.490			1.641	0.980
44	11.741		8.75	1.612	0.963
45	11.971			1.626	0.971
46	12.194	9.26	8.85	1.645	0.982
47	12.530	9.06		0.528	0.281
48	12.820		7.87	0.691	0.381
49	13.089			0.968	0.552
50	13.399		7.94	1.332	0.776
51	13.714			1.427	0.835
52	14.009		8.16	1.464	0.857
53	14.324			1.585	0.932
54	14.670	9.05	8.5	1.671	0.985
55	15.032			1.653	0.974
56	15.376		8.57	1.667	0.982
57	15.714			1.655	0.975
58	16.056		8.63	1.639	0.965
59	16.430			1.623	0.955
60	16.781		8.66	1.649	0.971
61	17.072			1.645	0.969

6 day stop flow

Table 20 (Continued): Aluminum Oxide Transport Data – Study #7_pH 9

Data results for aluminum oxide nanoparticle transport Study #7_pH 9; samples 62 - 94.

Sample	Pore Volume (mL)	Influent pH	Effluent pH	UV-Vis Abs	C/C _o	
62	17.397		8.63	1.653	0.974	
63	17.772			1.655	0.975	
64	18.162		8.63	1.687	0.995	
65	18.549			1.677	0.989	
66	18.866		8.64	1.641	0.966	
67	19.162			1.641	0.966	
68	19.516			1.667	0.982	Elution
69	19.795		8.59	1.667	0.982	
70	20.055			1.627	0.958	
71	20.318		8.62	1.632	0.961	
72	20.557			1.039	0.596	
73	20.832		8.6	0.522	0.277	
74	21.142			0.231	0.107	
75	21.441		8.66	0.150	0.065	
76	21.742			0.118	0.048	
77	22.029		8.7	0.097	0.037	
78	22.291			0.090	0.033	
79	22.552		8.7	0.096	0.036	
80	22.851			0.139	0.059	
81	23.169		8.71	0.077	0.026	
82	23.438			0.093	0.035	
83	23.697		8.68	0.091	0.034	
84	23.951			0.086	0.031	
85	24.179		8.72	0.085	0.031	
86	24.492			0.333	0.164	
87	24.764		7.94	0.210	0.088	
88	25.031			0.197	0.080	
89	25.293		7.98	0.221	0.095	
90	25.562			0.243	0.108	
91	25.854		8.05	0.171	0.068	
92	26.128			0.125	0.044	
93	26.457		8.41	0.107	0.034	
94	26.857			0.062	0.017	

Table 20 (Continued): Aluminum Oxide Transport Data – Study #7_pH 9

Data results for aluminum oxide nanoparticle transport Study #7_pH 9; samples 95 - 114.

Sample	Pore Volume (mL)	Influent pH	Effluent pH	UV-Vis Abs	C/C _o	
95	27.199		8.54	0.062	0.017	
96	27.479			0.105	0.033	
97	27.733		8.56	0.065	0.019	
98	27.989			0.074	0.023	
99	28.252		8.6	0.050	0.011	
100	28.516			0.075	0.023	
101	28.750		8.57	0.058	0.015	
102	29.003			0.041	0.007	
103	29.272		8.55	0.061	0.017	
104	29.538			0.054	0.013	
105	29.815		8.61	0.050	0.011	
106	30.163			0.047	0.010	
107	30.443		8.6	0.060	0.016	
108	30.725			0.133	0.048	
109	31.017		8.61	0.018	-0.014	LDL
110	31.269			0.071	0.021	LDL
111	31.520			0.046	0.009	LDL
112	31.848		8.66	0.049	0.011	LDL
113	32.205			0.048	0.010	LDL
114	32.490		8.61	0.063	0.018	LDL

Table 21: Non-Reactive Tracer Study Data – Study #8_pH 9_NRTPerformed for Al₂O₃ Study #8_pH 9

Column: A

Darcy Velocity: 1.9 cm/min

Electrolyte: K₂HPO₄/K₃HPO₄

Ionic Strength: 0.015 M

Data results for pentafluorobenzoic acid transport Study #8_pH 9_NRT; Samples 1 - 28.

Sample	Pore Volume (mL)	UV-Vis Abs	Dilution	C/C ₀	
1	-0.449	0.034	1	0.005	LDL
2	-0.285	0.020	1	0.004	LDL
3	-0.092	0.004	1	0.001	LDL
4	0.101	0.010	1	0.002	LDL
5	0.293	0.062	1	0.009	
6	0.486	0.789	1	0.108	
7	0.689	1.002	3.1	0.430	
8	0.901	1.883	2.8	0.738	
9	1.113	2.347	2.8	0.889	
10	1.325	2.432	2.8	0.937	
11	1.633	2.678	2.6	0.949	
12	2.038	2.398	3.0	0.975	
13	2.443	2.432	2.9	0.970	
14	2.848	2.456	2.9	0.976	
15	3.272	2.420	3.0	0.988	
16	3.677	2.310	3.1	0.996	
17	4.563	2.161	2.1	0.622	
18	5.411	2.284	3.2	0.994	
19	6.183	2.537	2.9	1.008	
20	6.983	2.260	3.3	1.011	
21	7.783	2.678	2.7	0.979	
22	8.554	2.678	2.7	0.992	
23	9.325	2.745	2.6	0.999	
24	10.105	2.620	2.8	0.996	
25	10.886	2.337	3.1	1.005	
26	11.638	2.293	3.2	1.011	Elution
27	11.850	2.509	2.9	1.010	
28	12.062	2.456	3.0	1.009	

Table 21 (Continued): Non-Reactive Tracer Study Data – Study #8_pH 9_NRT

Data results for pentafluorobenzoic acid transport Study #8_pH 9_NRT; Samples 29 - 52.

Sample	Pore Volume (mL)	UV-Vis Abs	Dilution	C/C ₀	
29	12.274	2.357	3.1	1.012	
30	12.486	2.092	3.3	0.936	
31	12.698	1.786	2.6	0.645	
32	12.910	0.884	2.7	0.327	
33	13.122	0.437	2.6	0.159	
34	13.334	0.600	1	0.082	
35	13.546	0.397	1	0.054	
36	13.855	0.284	1	0.039	
37	14.269	0.224	1	0.030	
38	14.684	0.191	1	0.026	
39	15.089	0.164	1	0.022	
40	15.493	0.143	1	0.019	
41	15.898	0.125	1	0.017	
42	16.785	0.093	1	0.012	
43	17.633	0.065	1	0.009	
44	18.424	0.053	1	0.007	LDL
45	19.339	0.037	1	0.005	LDL
46	20.236	0.034	1	0.004	LDL
47	21.045	0.031	1	0.004	LDL
48	21.855	0.027	1	0.003	LDL
49	22.665	0.025	1	0.003	LDL
50	23.416	0.021	1	0.003	LDL
51	24.226	0.021	1	0.003	LDL
52	25.093	0.020	1	0.002	LDL

Table 22: Aluminum Oxide Transport Data – Study #8_pH 9

Concentration: 100 mg/L
 Column: A
 Darcy Velocity: 1.9 cm/min
 Electrolyte: K₂HPO₄/K₃HPO₄
 Ionic Strength: 0.015 M

Data results for aluminum oxide nanoparticle transport Study #8_pH 9; samples 1 - 27.

Sample	Pore Volume (mL)	Influent pH	Effluent pH	UV-Vis Abs	C/C ₀
1	-0.385	9.19		0.113	0.071
2	-0.136			0.027	0.024
3	0.114		8.35	0.011	0.015
4	0.364			0.144	0.089
5	0.614			0.540	0.307
6	0.863		8.63	0.933	0.527
7	1.113			1.155	0.659
8	1.363			1.293	0.741
9	1.603		8.73	1.329	0.763
10	1.872			1.400	0.805
11	2.228			1.508	0.869
12	2.708		8.8	1.535	0.885
13	3.188			1.585	0.915
14	3.669			1.568	0.905
15	4.149			1.611	0.931
16	4.514		8.82	1.515	0.873
17	4.706		8.89		
18	5.811		8.95		
19	6.301			1.568	0.905
20	6.753		8.93		
21	7.204			1.640	0.948
22	7.646		8.93		
23	8.088			1.674	0.968
24	8.530		8.95		
25	8.972			1.682	0.973
26	9.414		8.95		
27	9.846			1.720	0.996

Table 22 (Continued): Aluminum Oxide Transport Data – Study #8_pH 9

Data results for aluminum oxide nanoparticle transport Study #8_pH 9; samples 28 - 46.

Sample	Pore Volume (mL)	Influent pH	Effluent pH	UV-Vis Abs	C/C _o
28	10.288		8.96		
29	10.720			1.739	1.007
30	11.210		8.91		
31	11.719			1.670	0.966
32	12.190		8.93		
33	12.680			1.691	0.978
34	13.276			1.581	0.913
35	13.718				
36	14.169			1.706	0.987
37	14.621		8.94		
38	15.101			1.753	1.015
39	15.581		8.93		
40	16.043			1.739	1.007
41	16.484		8.9		
42	16.907			1.729	1.001
43	17.190			1.729	1.001
44	17.706		8.91		
45	18.223			1.700	0.984
46	18.557		8.9		

Table 23: Non-Reactive Tracer Study Data – Study #9_pH 9_NRT

Performed for Al₂O₃ Study #9_pH 9

Column: A

Darcy Velocity: 1.8 cm/min

Electrolyte: K₂HPO₄/K₃HPO₄

Ionic Strength: 0.015 M

Data results for pentafluorobenzoic acid transport Study #9_pH 9_NRT; Samples 1 - 28.

Sample	Pore Volume (mL)	UV-Vis Abs	Dilution	C/C ₀	
1	-0.143	0.020	1	0.002	LDL
2	0.054	0.019	1	0.001	LDL
3	0.252	0.039	1	0.004	
4	0.449	0.738	1	0.099	
5	0.647	1.131	3.0	0.463	
6	0.844	1.940	3.0	0.797	
7	1.041	2.244	3.0	0.921	
8	1.239	2.310	3.0	0.953	
9	1.436	2.337	3.0	0.967	
10	1.634	2.366	3.0	0.976	
11	1.831	2.357	3.0	0.974	
12	2.029	2.357	3.0	0.976	
13	2.316	2.377	3.0	0.982	
14	2.693	2.377	3.0	0.979	
15	3.070	2.377	3.0	0.985	
16	3.447	2.409	3.0	0.990	
17	3.824	2.377	3.0	0.982	
18	4.560	2.377	3.0	0.963	
19	5.332	2.409	3.0	0.995	
20	6.086	2.420	3.0	1.000	
21	6.786	2.444	3.0	1.004	
22	7.558	2.409	3.0	1.003	
23	8.294	2.420	3.0	1.000	
24	9.048	2.745	2.6	0.994	
25	9.784	2.420	3.0	0.998	
26	10.537	2.658	2.8	1.008	
27	11.309	2.420	3.0	1.006	
28	11.902	2.444	3.0	1.007	

Table 23 (Continued): Non-Reactive Tracer Study Data – Study #9_pH 9_NRT

Data results for pentafluorobenzoic acid transport Study #9_pH 9_NRT; Samples 29 - 63.

Sample	Pore Volume (mL)	UV-Vis Abs	Dilution	C/C ₀	
29	12.665	2.444	3.0	1.003	
30	13.428	2.444	3.0	1.007	
31	13.616	2.444	3.0	1.016	Elution
32	13.805	2.444	3.0	1.007	
33	13.984	2.456	3.0	1.013	
34	14.181	2.456	3.0	1.012	
35	14.379	2.420	3.0	1.005	
36	14.576	2.229	3.0	0.927	
37	14.783	1.366	3.0	0.562	
38	14.989	0.545	3.0	0.222	
39	15.187	0.673	1	0.090	
40	15.384	0.398	1	0.052	
41	15.671	0.265	1	0.034	
42	16.048	0.198	1	0.025	
43	16.425	0.172	1	0.022	
44	16.802	0.157	1	0.020	
45	17.179	0.141	1	0.017	
46	17.556	0.129	1	0.016	
47	18.382	0.116	1	0.014	
48	19.154	0.103	1	0.012	
49	19.908	0.096	1	0.011	
50	20.662	0.089	1	0.010	
51	21.425	0.086	1	0.010	
52	22.188	0.065	1	0.007	
53	22.942	0.073	1	0.008	
54	23.704	0.060	1	0.007	
55	24.485	0.052	1	0.006	
56	25.239	0.044	1	0.005	
57	25.975	0.041	1	0.004	
58	26.729	0.044	1	0.005	
59	27.483	0.040	1	0.004	
60	28.237	0.044	1	0.005	
61	28.973	0.023	1	0.002	
62	29.727	0.033	1	0.003	
63	30.481	0.026	1	0.002	

Table 24: Aluminum Oxide Transport Data – Study #9_pH 9

Concentration: 100 mg/L
 Column: A
 Darcy Velocity: 1.9 cm/min
 Electrolyte: K₂HPO₄/K₃HPO₄
 Ionic Strength: 0.015 M

Data results for aluminum oxide nanoparticle transport Study #9_pH 9; samples 1 - 27.

Sample	Pore Volume (mL)	Influent pH	Effluent pH	UV-Vis Abs	C/C _o
1	-0.536	9.44		0.069	0.051
2	-0.336			0.034	0.031
3	-0.136		8.38	0.067	0.050
4	0.064			0.043	0.036
5	0.264			0.072	0.053
6	0.455		8.69	0.245	0.156
7	0.646			0.517	0.314
8	0.847			0.738	0.449
9	1.047		8.64	0.873	0.531
10	1.238			0.951	0.578
11	1.429			0.997	0.606
12	1.629		8.73	1.056	0.642
13	1.829			1.112	0.676
14	2.029			1.154	0.702
15	2.229		8.76	1.169	0.711
16	2.429			1.204	0.732
17	2.629			1.237	0.752
18	2.830		8.76	1.283	0.780
19	3.030			1.321	0.803
20	3.239			1.286	0.782
21	3.430			1.103	0.671
22	3.721		8.86	1.179	0.717
23	4.103			1.224	0.744
24	4.476		8.93	1.210	0.736
25	4.867			1.414	0.860
26	5.267		8.88	1.489	0.905
27	5.740		8.99		

5-10 min. stop flow

Table 24 (Continued): Aluminum Oxide Transport Data – Study #9_pH 9

Data results for aluminum oxide nanoparticle transport Study #9_pH 9; samples 28 - 59.

Sample	Pore Volume (mL)	Influent pH	Effluent pH	UV-Vis Abs	C/C _o	
28	6.122			1.554	0.945	
29	6.504		9.01			
30	6.886			1.614	0.981	
31	7.268		8.94			
32	7.705			1.547	0.940	
33	8.142		8.9			
34	8.524			1.605	0.976	
35	8.706			1.455	0.885	5-10 min. stop flow
36	9.088		8.94			
37	9.470			1.489	0.905	
38	9.852		8.93			
39	10.234			1.560	0.948	
40	10.616		8.92			
41	10.998			1.609	0.978	
42	11.407		8.95			
43	11.817			1.621	0.985	
44	12.199		8.9			
45	12.581			1.646	1.001	
46	12.972		8.91			
47	13.363			1.646	1.001	
48	13.736		8.88			
49	14.109			1.664	1.012	
50	14.345	9.14		1.540	0.936	Elution
51	14.545			1.593	0.968	
52	14.746			1.543	0.938	
53	14.946			1.571	0.955	
54	15.146		8.8	1.560	0.948	
55	15.346			1.282	0.779	
56	15.546			0.789	0.480	
57	15.737		8.77	0.442	0.269	
58	15.928			0.229	0.146	
59	16.128			0.134	0.090	

Table 24 (Continued): Aluminum Oxide Transport Data – Study #9_pH 9

Data results for aluminum oxide nanoparticle transport Study #9_pH 9; samples 60 - 93.

Sample	Pore Volume (mL)	Influent pH	Effluent pH	UV-Vis Abs	C/C _o
60	16.337		8.76	0.074	0.054
61	16.547			0.092	0.065
62	16.747			0.066	0.049
63	16.947		8.74	0.079	0.057
64	17.147			0.083	0.059
65	17.347			0.076	0.055
66	17.547		8.75	0.080	0.058
67	17.747			0.042	0.036
68	17.947			0.056	0.044
69	18.175		8.74	0.088	0.062
70	18.493			0.056	0.044
71	18.875		8.86	0.058	0.045
72	19.266			0.033	0.031
73	19.548		8.74	0.119	0.081
74	19.930		8.81		
75	20.312			0.052	0.041
76	20.667		8.81		
77	21.040			0.031	0.029
78	21.422		8.77		
79	21.804			0.050	0.040
80	22.186		8.79		
81	22.595			0.040	0.035
82	23.005		8.81		
83	23.387			0.031	0.029
84	23.769		8.81		
85	24.160			0.060	0.046
86	24.397			0.037	0.033
87	24.760		8.74		
88	25.079			0.067	0.050
89	25.461		8.81		
90	25.843			0.044	0.037
91	26.225		8.79		
92	26.607			0.046	0.038
93	26.989		8.8		

Table 24 (Continued): Aluminum Oxide Transport Data – Study #9_pH 9

Data results for aluminum oxide nanoparticle transport Study #9_pH 9; samples 94 - 115.

Sample	Pore Volume (mL)	Influent pH	Effluent pH	UV-Vis Abs	C/C _o	
94	27.398			0.042	0.036	
95	27.808		8.79			
96	28.208			0.056	0.044	
97	28.617		8.77			
98	29.008			0.106	0.073	
99	29.372		8.77			
100	29.736			0.036	0.032	
101	29.918			0.015	0.020	
102	30.300		8.81			
103	30.682			0.007	0.016	LDL
104	30.873			0.011	0.018	
105	31.100			0.097	0.068	
106	31.537		8.79			
107	31.983			0.089	0.063	
108	32.410		8.77			
109	32.792			-0.008	0.007	LDL
110	33.183		8.73			
111	33.575			-0.006	0.009	LDL
112	33.993		8.76			
113	34.430			-0.011	0.006	LDL
114	34.812		8.75			
115	35.203			-0.014	0.004	LDL